CALCULATION OF SCALAR OPTICAL DIFFRACTION FIELD FROM ITS DISTRIBUTED SAMPLES OVER THE SPACE

A DISSERTATION

SUBMITTED TO THE DEPARTMENT OF ELECTRICAL AND

ELECTRONICS ENGINEERING

AND THE INSTITUTE OF ENGINEERING AND SCIENCES

OF BILKENT UNIVERSITY

IN PARTIAL FULFILLMENT OF THE REQUIREMENTS

FOR THE DEGREE OF

DOCTOR OF PHILOSOPHY

By

Gökhan Bora Esmer

April 2010

I certify that I have read this thesis and that in my opinion it is fully adequate, in scope and in quality, as a thesis for the degree of Doctor of Philosophy.

Prof. Dr. Levent Onural(Supervisor)

I certify that I have read this thesis and that in my opinion it is fully adequate, in scope and in quality, as a thesis for the degree of Doctor of Philosophy.

Prof. Dr. Haldun M. Özaktaş

I certify that I have read this thesis and that in my opinion it is fully adequate, in scope and in quality, as a thesis for the degree of Doctor of Philosophy.

Prof. Dr. Orhan Arıkan

I certify that I have read this thesis and that in my opinion it is fully adequate, in scope and in quality, as a thesis for the degree of Doctor of Philosophy.

Assoc. Prof. Dr. Mehmet Tankut Özgen

I certify that I have read this thesis and that in my opinion it is fully adequate, in scope and in quality, as a thesis for the degree of Doctor of Philosophy.

Assist. Prof. Dr. İbrahim Körpeoğlu

Approved for the Institute of Engineering and Sciences:

Prof. Dr. Mehmet Baray
Director of Institute of Engineering and Sciences

ABSTRACT

CALCULATION OF SCALAR OPTICAL DIFFRACTION FIELD FROM ITS DISTRIBUTED SAMPLES OVER THE SPACE

Gökhan Bora Esmer
Ph.D. in Electrical and Electronics Engineering
Supervisor: Prof. Dr. Levent Onural
April 2010

As a three-dimensional viewing technique, holography provides successful three-dimensional perceptions. The technique is based on duplication of the information carrying optical waves which come from an object. Therefore, calculation of the diffraction field due to the object is an important process in digital holography. To have the exact reconstruction of the object, the exact diffraction field created by the object has to be calculated. In the literature, one of the commonly used approach in calculation of the diffraction field due to an object is to superpose the fields created by the elementary building blocks of the object; such procedures may be called as the "source model" approach and such a computed field can be different from the exact field over the entire space. In this work, we propose four algorithms to calculate the exact diffraction field due to an object. These proposed algorithms may be called as the "field model" approach. In the first algorithm, the diffraction field given over the manifold, which defines the surface of the object, is decomposed onto a function set derived from propagating plane waves. Second algorithm is based on pseudo inversion of the system

matrix which gives the relation between the given field samples and the field over a transversal plane. Third and fourth algorithms are iterative methods. In the third algorithm, diffraction field is calculated by a projection method onto convex sets. In the fourth algorithm, pseudo inversion of the system matrix is computed by conjugate gradient method. Depending on the number and the locations of the given samples, the proposed algorithms provide the exact field solution over the entire space. To compute the exact field, the number of given samples has to be larger than the number of plane waves that forms the diffraction field over the entire space. The solution is affected by the dependencies between the given samples. To decrease the dependencies between the given samples, the samples over the manifold may be taken randomly. Iterative algorithms outperforms the rest of them in terms of computational complexity when the number of given samples are larger than 1.4 times the number of plane waves forming the diffraction field over the entire space.

Keywords: Digital Holography, Scalar Optical Diffraction, Plane Wave Decomposition, Signal Decomposition, Projection Onto Convex Sets, Conjugate Gradient, Eigenvalue Distribution, Computer Generated Holography

ÖZET

UZAYDA DAĞILMIŞ ÖRNEKLERİNDEN SKALAR OPTİK KIRINIM ALANI HESAPLANMASI

Gökhan Bora Esmer
Elektrik ve Elektronik Mühendisliği Bölümü Doktora
Tez Yöneticisi: Prof. Dr. Levent Onural
Nisan 2010

Üç boyutlu görüntüleme tekniği olan holografi, üç boyut algısını başarıyla sağlar. Bu görüntüleme tekniği, nesneden gelen bilgi taşıyan optik dalgaların tıpkısının üretilmesine dayanır. Bu yüzden, sayısal holografide nesne kırınım deseninin hesaplanması önemlidir. Nesnenin optik yönden aynen geri çatılabilmesi için, nesne tarafından üretilen kırınım deseninin doğru olarak hesaplanması gerekmektedir. Litaretürde, nesneden yayılan kırınım deseninin hesaplanmasında nesneyi oluşturan temel parçalardan yayılan kırınım desenlerinin toplanması yaygın olarak kullanılan bir yaklaşımdır; bu tür yöntemler "kaynak modeli" yaklaşımı olarak adlandırılabilir ve bu yöntemlerle hesaplanan alanlar tüm uzaydaki gerçek alandan farklı olabilir. Bu çalışmada, nesneden yayılan kırınım deseninin doğru olarak hesaplamasını sağlayan dört algoritma önerdik. Bu önerilen algoritmalar "alan modeli" yaklaşımı olarak adlandırılabilir. İlk algoritma, kırınım alanının, düzlemsel dalgaların nesnenin yüzeyini belirleyen manifolt üzerindeki kesitini işlevlere ayrıştırılmasına dayanmaktadır. İkinci algoritma, verilen kırınım deseni örnekleri ile enine bir düzlem üzerindeki kırınım deseni arasındaki ilişkiyi veren sistem matrisinin yaklaşık tersinin alınmasına dayanır. Üçüncü ve dördüncü algoritmalar yinelemeli yöntemlerdir. Üçüncü algoritmada,

kırınım deseni dışbükey kümeleri üzerine izdüşüm metoduyla hesaplanmaktadır. Dördüncü algoritmada, sistem matrisinin yakaşık tersinin alınması eşlenik eğim (conjugate gradient) yöntemi ile hesaplanır. Verilen kırınım deseni örneklerinin sayısı yeterli ve bu örneklerin yerleri uygun ise önerilen algoritmalar uzaydaki gerçek kırınım desenini verir. Gerçek kırınım desenini hesaplayabilmek için, verilen örnek sayısının tüm uzaydaki kırınım desenini oluşturan düzlem dalgaların sayısından fazla olması gerekmektedir. Verilen örneklerin birbirleriyle bağımlılıkları çözümü etkilemektedir. Örneklerin manifolt üzerinden rastgele alınması örneklerin birbirleriyle bağımlılıklarını azaltmaktadır. Yinelemeli algoritmalar, verilen örnek sayısı tüm uzaydaki kırınım desenini oluşturan düzlem dalgaların sayısından en az 1.4 kat fazla olduğunda diğer algoritmalara göre kırınım alanı hesabını daha kolay yapar.

Anahtar Kelimeler: Sayısal Holografi, Skalar Optik Kırınım, Düzlem Dalga Ayrıştırımı, Sinyal Ayrıştırımı, Dışbükey Kümelerin Üzerine İzdüşüm, Eşlenik Eğim (Conjugate Gradient), Özdeğer Dağılımı, Bilgisayarla Üretilmiş Holografi

ACKNOWLEDGMENTS

I would like to express my sincere thanks to my supervisor Prof. Dr. Levent Onural for his guidance, support, and encouragement during the course of this research.

I also would like to thank Prof. Dr. Haldun Özaktaş, Prof. Dr. Orhan Arıkan, Assoc. Prof. Dr. Mehmet Tankut Özgen and Assist. Prof. Dr. İbrahim Körpeoğlu for reading and commenting on the thesis.

This work is supported by EC within FP6 under Grant 511568 with acronym 3DTV.

I also would like to thank to TÜBİTAK (The Scientific and Technological Research Council of Turkey) for financial support.

Finally, I want to express my gratitude to my family for their love, support, and understanding. I owe them a lot. I dedicate this dissertation to them.

Contents

List of Figures

List of Tables

List of Publications

This dissertation is based on the following publications.

[Publication-I] G.B. Esmer, V. Uzunov, L. Onural, H.M. Ozaktas and A. Gotchev, "*Diffraction field computation from arbitrarily distributed data points in space*", Signal Processing-Image Communication, vol. 22, no. 2, pp. 178-187, 2007.

[Publication-II] V. Uzunov, A. Gotchev, G.B. Esmer, L. Onural and H. Ozaktas, "*Non-Uniform Sampling and Reconstruction of Diffraction Field*", TICSP Series 34, Florence, Italy, 2006.

[Publication-III] G.B. Esmer, L. Onural, H. Ozaktas and A. Gotchev, "*An algorithm for calculation of scalar optical diffraction due to distributed data over 3D space*", ICOB, Workshop On Immersive Communication And Broadcast Systems, Berlin, Germany, 2005.

[Publication-IV] E. Ulusoy, G.B. Esmer, H.M. Ozaktas, L. Onural, A. Gotchev and V. Uzunov, "*Signal Processing Problems and Algorithms in Display Side of 3DTV*", ICIP, Atlanta, GA, USA, 2006.

[Publication-V] G.B. Esmer, L. Onural, V. Uzunov, A. Gotchev and H.M. Ozaktas, "*RECONSTRUCTION OF SCALAR DIFFRACTION FIELD FROM DISTRIBUTED DATA POINTS OVER 3D SPACE*", 3DTV-Con, Kos Island, Greece, 2007.

[Publication-VI] G.B. Esmer, L. Onural, H.M. Ozaktas, V. Uzunov and A. Gotchev, "*PERFORMANCE ASSESSMENT OF A DIFFRACTION FIELD COMPUTATION METHOD BASED ON SOURCE MODEL*", 3DTV-ConII, Istanbul, Turkey, 2008.

[Publication-VII] M. Kovachev, R. Ilieva, P. Benzie, G.B. Esmer, L. Onural, J. Watson, and T. Reyhan, *Three-Dimensional Television: Capture, Transmission, Display, Chapter 15: Holographic 3DTV Displays Using Spatial Light Modulators*, pp. 529556, Springer-Verlag Berlin Heidelberg, 2008.

[Publication-VIII] M. Kovachev, R. Ilieva, L. Onural, G.B. Esmer, T. Reyhan, P. Benzie, J.Watson, and E. Mitev, *Reconstruction of computer generated holograms by spatial light modulators*, in LECTURE NOTES IN COMPUTER SCIENCE, vol. 4105, pp. 706713, 2006.

The contributions of the author to Publications I, III, IV, V, VI, VII and VIII were as follows. As the first author in Publication-III, -V and -VI, the author designed and implemented the algorithms, performed the mathematical derivations, reported experiments; and preparation of the manuscript. The author designed and implemented the first algorithm proposed in Publication-I, and also he prepared the entire manuscript except the part related to the second algorithm. In Publications-IV, -VII, -VIII, the first algorithms in the documents were designed, implemented and the related manuscript was prepared by the author.

Dedicated to My Family ...

Chapter 1

Introduction

In this dissertation, calculation methods of the exact diffraction field created by an object are discussed and presented. The calculation of the exact diffraction field is important in 3D visualization, because as a 3D visualization technique, digital holography (DH) depends on the calculated diffraction field created by an object. Even if DH is commonly used to describe the capturing process of optical diffraction fields by charged coupled devices (CCDs), it is also used to explain the calculation of the diffraction fields by numerical operations as in computer generated holography. In this work, diffraction field due to an object is obtained by employing numerical operations. The properties of the object are carried to the generated digital hologram by the calculated diffraction field due to that object. Hence, calculation of the exact diffraction field due to the object paves the way to capture the information carrying optical waves related to the object without any loss.

Visual media is a highly versatile tool with many applications. Three dimensional (3D) visualization is an advanced mode within visual media. The developed 3D viewing techniques in the literature are based on the 3D perception capabilities of an object by the human visual system [3–7]. 3D is perceived

as a consequence of the depth cues. Each viewing technique satisfies some of the depth cues used by the human visual system. The quality of the 3D display system is determined by the sense of depth and the resolution of the system. There are several 3D visualization techniques which can provide successful 3D perceptions. To have successful perceptions of a 3D scene, the depth cues such as binocular disparity, motion parallax, occlusion and accommodation have to be satisfied. For instance, binocular disparity can be satisfied by having a slightly different image for each eye [8–10]. Isolation of the images can be obtained by using special equipments (i.e., goggles) or techniques (i.e., holography). In [8–10], it is mentioned that if the spectator has to wear a goggle to isolate the images to have 3D perception, then the viewing technique is called as stereoscopy and if the spectator does not need a goggle to see the scene in 3D then it is called as auto-stereoscopy. Even if the mentioned classification in 3D visualization can be commonly found in the literature [8–10], such a classification is confusing. Therefore, an alternative classification of the 3D visualization techniques can be defined according to the number of images displayed. For instance, if there are two images, then the technique can be called as stereoscopy; and if there are more than two images, then the technique can be called as multi-view. As holography, there are some 3D visualization techniques that can provide infinite number of images because viewing direction can be changed continuously. By increasing the number of viewing directions, more natural viewing and 3D perception can be obtained.

In holography, diffracted optical waves due to a 3D object are attempted to be replicated physically [11, 12]. Illumination of the hologram results in replication of the original optical waves and provide the same 3D perception as if looking at the object itself. Quality of the optical duplication of the object depends on the size, the resolution and other properties of the hologram such as accuracy of the captured diffraction field.

The information carrying optical waves related to the object can be mimicked by the calculated diffraction field. Then, the calculated diffraction field is used in the generation of the digital hologram. Therefore, more accurate calculations of the diffraction field created by the object provide better reconstructions of the object due to the generated digital hologram. In this dissertation, four diffraction field calculation methods are proposed and these methods provide to calculate the exact diffraction field mimicking the information carrying optical waves created by an object.

Holography can be explained by the interference of the waves and the principles of the optical diffraction [3, 5, 6, 13]. The interference pattern is obtained by the superposition of two or more waves and the principles of the optical diffraction can be explained by the behavior of the propagating waves over the space. The optical diffraction created by an object is a complex valued signal which carries amplitude and phase information. The amplitude and the phase information of the optical diffraction field can be captured and stored by modulating the diffraction field by a reference wave. The employed modulation process is an amplitude modulation as in communication systems [13, 14]. Holographic patterns can also be generated in a computer environment by using signal processing techniques [7, 12, 15, 16]. The propagation behavior of the optical diffraction field created by an object can be simulated by numerical methods. One of the challenging issues during the holographic pattern generation process is the computation of the optical diffraction field due to a 3D object, because such a calculation is a costly process as a consequence of the associated computational complexity [11, 12, 16]. High computational complexity in diffraction field computation arises due to dealing with complex amplitude signals and kernels whose sizes are taken as large as possible to get more detailed and larger reconstructed objects. Moreover, the optical diffraction due to an object with a depth information may not be calculated by a linear shift invariant model. Further simplifications are applied on the computation of diffraction field kernel and the structure of the

object, such as representation of the object using planar slices or fewer number of points [17–19].

A holographic signal can be generated by the interference of a reference wave and the diffraction field due to an object. This process can be performed either optically or by computation and each method has its benefits and problems. One of the problems of optical capturing is the sensitivity of holographic signals to vibrations. Even small displacements caused by the vibrations can spoil the captured field. As a solution to the vibration problem, mostly fast charged coupled device (CCD) sensors are used for capturing the holographic signals [20]. On the other hand, there is no such problem of vibrations when the holographic signal is generated by numerical methods. Furthermore, by using the numerical methods, holographic signals that would be generated by artificial objects can be obtained [12].

The capture and generation of the holographic signals can be a troublesome processes in general as mentioned above, but how to drive a holographic display is another challenging problem. Each display device has its own specific properties, thus tuning the holographic signal according to the properties of the display is needed to get a reconstructed object with higher resolution and contrast [21, 22]. The commercially available display devices can be still or dynamic [5, 16]. In still displays, holographic signal can be written only once, for example on holographic films. Liquid crystal (LC) panels and digital micromirror devices (DMD) are two commonly used types of dynamic displays [23–25]. The holographic signal on the dynamic displays can be refreshed as fast as the video frame rate supported by those devices [18]. However, resolution limits of still displays are usually higher than the achievable maximum resolution of the dynamic displays.

The algorithms to generate holographic patterns by numerical methods are computationally complex. To overcome such difficulties, two approximations are commonly used for diffraction field computation; these are called as Fresnel and

far-field approximations. The major advantage of Fresnel and far-field approximations is to reduce the computational complexity mainly due to the separability of functions that represent the light propagation [12, 15, 16, 26]. Therefore, computational complexity and the amount of memory allocation decrease drastically under these approximations. Further approximations can also be employed to reduce the complexity [17, 27–29]. Independent of the approximations employed to the models of wave propagation, the shapes of the underlying object may also be approximated. For example, objects can be represented as point clouds or planar meshes. Computation time of holographic fringe patterns can be further curtailed by running the algorithms on graphical processing units (GPU) instead of central processing units (CPU). As a consequence, a significant computation speed up can be achieved [17, 18, 30, 31].

A 3D object can be built from sample points and it is a widely used technique in both computer graphics and holography [17, 18, 32]. These sampled objects can carry the characteristics of the original continuous object. The diffraction field due to the sampled object can be computed by superposing the diffraction fields created by each sample point and it is assumed that each sample point acts as a point light source. Such approaches in diffraction field computation, where each object point is modeled as a point light source, utilize the so called "source model". Several fast algorithms, which are based on the source model, are proposed in the literature. Some of these algorithms employ look-up tables [11] or segmentation of the diffraction fields emanated from point sources [17]. Moreover, rapid computations are also achieved by employing a GPU [17, 18, 30, 31]. 3D objects can also be formed by stitching planar patches [32]. Then, diffraction field of the object is computed by adding the diffraction fields due to these patches [27, 33, 34]. Even though the source model based algorithms are commonly used to compute diffraction field due to an object, the computed field due to the 3D object will not be the correct field. The deviation from the correct solution is induced by the superposition of the fields emanating from the building blocks of

the object (In some scenarios, these building blocks are taken as points, planar patches or slices along transversal axes). In the source model, it is assumed that each building block emits light as if other blocks do not exist. Such independently computed fields for each block are then superposed. The field obtained after superposition can only provide the correct field if there are no mutual couplings between the fields emitted by these blocks. However, the actual field over a block is generally affected from all other sources. As a result of this, the source values over the blocks deviate from the given actual field values. Therefore, the result may be significantly in error. To overcome the deviation problem, alternative procedures, which are called as "field model" algorithms, are proposed in this dissertation. In the field model, the diffraction field computation due to an object is attacked by a simultaneous calculation of the field over the entire space. Therefore, the exact field over the entire space can be computed.

In this dissertation, four field model based algorithms are presented. These algorithms pave the way to compute the exact diffraction field created by an object. The exact field is obtained by simultaneous calculation of the field over the entire space. In the first algorithm, objects are modeled as continuous manifolds. Then, a continuous signal is defined on the manifold representing the diffraction field over the manifold. Afterwards, the field on the manifold is sampled. In the rest of the algorithms, which are proposed in this work, the manifold is not known explicitly. Only the samples taken over the manifold are provided. Consequently, all the presented algorithms based on the field model compute the continuous diffraction field over the entire space from the samples which are taken over the manifold. Among the four algorithms, the first algorithm is based on the decomposition of the diffraction field on a basis function set which is formed by the intersections of the propagating plane waves by the manifold. The second one uses a brute force computation of the pseudo inversion of the system matrix (System matrix represents the diffraction field relationship between a hypothetical plane over transversal axes and the given samples over the manifold). The

algorithm based on pseudo inversion of the system matrix is generated as a performance comparison tool for the algorithms which work iteratively to compute the diffraction field over the entire space from the given samples on the manifold. First iterative algorithm utilizes projection operation onto convex sets. The second one employs conjugate gradient search algorithm to compute the inverse of the system matrix.

In this dissertation, even if we focus into the calculation of the exact diffraction field due to an object, it will be beneficial for the reader to understand the fundamentals of the holography and its evolution. Therefore, next two sections are included to Chapter 1.

1.1 Holography

Holography is one of the successful and natural 3D viewing techniques [12], because it targets the recreation of the diffracted optical waves due to an object. In holographic techniques, diffraction field due to an object carries the information related to that object. The scattered light from an object is recorded and then the optical replica of the captured light is attempted to be generated. Therefore, the information on the reconstructed object is related to the captured diffraction field. The diffraction field can be obtained by using optical setups or by employing digital calculations. If the digital calculations are chosen to find the diffraction field, then performing more accurate diffraction field calculations will provide more related information about the object. The exact replication of the object can be possible when the diffraction field created by the object is calculated without any error. In this work, four algorithms for computation of exact diffraction field due to an object are proposed.

The theory of the holography can be explained by the principles of the optical wave propagation and the mathematics of the interference. The interference of

the diffraction field of the object, $\mathbf{\Psi}$, and a reference beam, $\mathbf{R}$, is needed during the recording process. When the recorded pattern is illuminated by the same reference beam, the diffracted light from the recorded pattern provides a 3D image of the object. We prefer to choose the reference wave as a plane wave which has a simple representation,

$$\mathbf{R} = R_0 \exp(jkx \sin\theta_x) \exp(jky \sin\theta_y) \exp(jkz \sin\theta_z) \tag{1.1}$$

where R_0 is the complex amplitude of the reference wave, k is the wave number, $\frac{2\pi}{\lambda}$ and λ is the optical wave length; and θ_x, θ_y and θ_z denote the incidence angles of the reference beam to the recording medium. The captured diffraction field over the medium is expressed as [13, 15, 16, 26]

$$\mathbf{I} = |\mathbf{\Psi} + \mathbf{R}|^2. \tag{1.2}$$

The expansion of Eq. 1.2 is

$$\mathbf{I} = |\mathbf{\Psi}|^2 + |\mathbf{R}|^2 + \mathbf{\Psi}\mathbf{R}^* + \mathbf{\Psi}^*\mathbf{R} \tag{1.3}$$

where * denotes the complex conjugation. The first term in Eq. 1.3 is the object self-interference. It has a spatially varying structure and it can distort the reconstructed image if it is not suppressed or spatially separated. Spatial separation of the first term can be achieved by having larger reference wave incidence angles. The second term is the reference bias and it is a DC signal when the reference wave is chosen as in Eq. 1.1. The other two terms, $\mathbf{\Psi}\mathbf{R}^*$ and $\mathbf{\Psi}^*\mathbf{R}$, are the signals that carry the necessary holographic information needed in the reconstruction process.

In the reconstruction process, the recorded hologram is illuminated by the same reference wave. The diffraction from the illuminated hologram is expressed as [13]

$$\mathbf{R}_r = \mathbf{R}|\mathbf{R}|^2 ** \mathbf{h}^* + \mathbf{R}|\mathbf{\Psi}|^2 ** \mathbf{h}^* + |\mathbf{R}|^2\mathbf{\Psi} ** \mathbf{h}^* + \mathbf{R}^2\mathbf{\Psi}^* ** \mathbf{h}^* \tag{1.4}$$

where $\mathbf{h}$ denotes the impulse response of the free space diffraction and $**$ represents the 2D convolution. The third term in Eq. 1.4 gives the reconstruction of

the object. The last term also carries the same information related to the object, it is called as twin image and gives the reconstruction of the object at a different distance.

There are many different types of holograms. Common hologram types are transmission, reflection, rainbow , integral, embossed, computer generated and volume holograms [35].

Holography has a great potential in scientific and artistic applications. Some typical applications are high resolution imaging of tiny objects [36], multiple imaging [37–39], holograms of artificially generated objects [40–43], information storage [44–46], character recognition [47, 48], holographic interferometry [3, 5] and 3DTV [49].

1.2 History of Holography

Holography was invented by Nobel price winner scientist Dennis Gabor in 1948. While he was working to improve the resolution of an electron microscope, he came up with the theory of holography [50]. The theory is based on the modulation of the diffraction field by another wave. As a result of the modulation, entire optical information related to object can be stored on a photographic film, even if only the intensity of the optical wave can be captured by a film. He named the theory as holography which is originated from the Greek words "holos" and "gramma". The word holos means whole and gramma indicate the message. At the end of 40's, there was no truly coherent light sources, so there had not been any further development in holography during the following decade [6].

In 1960, N. Bassov, A. Prokhorov and C. Townes invented the laser. By using the coherent light source, the holograms allowing to reconstruct sharper images was produced [6]. In 1962, E. Leith and J. Upatnieks developed the off-axis

holography technique. In the same year, Y. N. Denisyuk produced holograms that could be viewed by using white light. In 1965, a computer generated hologram (CGH) method was presented by B. R. Brown and A. W. Lohmann [6]. In 1989, MIT Media Laboratory Spatial Group designed and built a holographic video system [11, 51]. That system could work in real-time [51]. However, the information content was reduced by the elimination of the vertical parallax, reduction of resolution and reduction of the image size and the horizontal viewing zone [11].

1.3 Organization of the dissertation

The organization of the dissertation is as follows. In the next chapter, mathematical background and principles of the scalar optical diffraction are presented. In Chapter 3, the computation of the exact diffraction field over the entire space from the diffraction field over a given manifold is presented. The presented method in Chapter 3 is based on the decomposition of the diffraction field onto a function set which is obtained from the intersections of the propagating plane waves by the manifold. In Chapter 4, three more field model algorithms are presented and some simulation results are shown as an illustration and evaluation purposes. Two of the presented algorithms in Chapter 4 are based on iterative methods and the other one is developed because of the comparison purposes. Furthermore, performances of the presented algorithms related to the distributions of the given samples over the space and the number of the given samples are investigated under several scenarios. In Chapter 5, effect of the distribution of the given samples is analyzed when the source model approach is used to compute the diffraction field due to the given samples. In Chapter 6, some conclusions about the proposed algorithms, employed to compute diffraction field due to an object, are given.

Chapter 2

Scalar Diffraction Theory

In this dissertation, algorithms for calculation of the exact diffraction field due to an object, which may have non-planar surface, are proposed. The proposed algorithms are based on the fundamentals of the scalar optical diffraction so, it is important to understand these fundamentals. In this chapter, not only did we present the fundamentals of the scalar diffraction, but we also showed the diffraction field calculation methods like plane wave decomposition and Rayleigh-Sommerfeld diffraction integral only explain the diffraction due to a field given on a planar surface. Therefore, to compute the exact field over the space due to the field defined over a non-planar surface, further improvements on the diffraction field computation methods like plane wave decomposition and Rayleigh-Sommerfeld diffraction integral, are needed. Straightforward application of these methods, which is the superposition of the diffraction fields emitted by the sample points, in computation of the diffraction field over the entire space due to the field defined over a non-planar surface will give erroneous results. In Chapters 3 and 4, algorithms for calculation of the exact diffraction field due to a field given on a non-planar surface, that are based on the diffraction field relationship presented in this chapter, are proposed.

Diffraction of light is investigated under four categories in the literature: ray optics, wave optics, electromagnetic optics and quantum optics [26]. Ray optics is the simplest approach. In ray optics, diffraction phenomena described by rays within a set of geometrical rules. Ray optics uses the approximation of infinitesimal wavelength, though it paves the way to explain many simple experiments. In these simple experiments, the illuminated objects are much larger then the wavelength of the light. As a result of this, infinitesimal wavelength approximation is satisfied. In ray optics approach, we assume that the light follows an optical path according to Fermat's principle: "light rays travel along the path of least time" [26]. The optical path is determined by the variation of the refractive index n over the medium that all the optical activities occur. Wave optics can provide solutions to some phenomena associated with the diffraction of light that can not be explained by the ray optics, such as diffraction due to small objects whose sizes are comparable to wavelength. Wave optics also explains the interference phenomena that can not be described by ray optics [15, 16, 26]. The major difference between the wave and the ray optics is the wavelength. If we assume that the wavelength in wave optics is infinitesimal then it becomes ray optics. Wave optics is based on scalar wave model of the light. In other words, polarization of the propagating wave is omitted. However, wave optics can not cover the entire diffraction phenomena; for example, it can not clarify the refraction and reflection of light at the boundaries between dielectric materials and the vectorial nature of the light. Electromagnetic optics is needed to explain these kinds of problems. The mentioned three approaches, which are ray, wave and electromagnetic optics, form the bases of classical optics. Electromagnetic optics is the most general approach in classical optics, but there are still some situations that can not be explained within classical optics. These situations may be described by the quantum mechanical nature of the light. The quantum optics theory can handle virtually all optical phenomena.

In this work, we deal with free space propagating optical waves. Therefore, we assume that wave optics principles are sufficient to explain all the diffraction related scenarios that we are interested in. As a result of this, we employ the scalar optical formulations in diffraction field calculations.

2.1 Fundamentals of the Scalar Optical Diffraction

Foundations of the scalar optical diffraction and the necessary derivations can be found in [15, 16]. The scalar optical diffraction field expression, which is derived in [15, 16], explains the diffraction field relationship between a field defined over a planar surface and an observation point. An illustration of the planar surface and the observation point can be seen from Figure 2.1. Please note that, in all the notations in this work x and y axes are taken as transversal directions, and z axis is the longitudinal direction. In Figure 2.1, the position vector $\mathbf{r}_0$ denotes the location of the observation point P_0 and the vector $\mathbf{r}_S$ is the position vector that designates a point on the planar surface S_0 on which the given diffraction field is known. The vector $\mathbf{r}_{0S}$ represents the difference vector $\mathbf{r}_0 - \mathbf{r}_S$. The vector $\mathbf{n}$ is the outward normal unit vector. In Figure 2.1, the planar surface S_0 is chosen as $z = 0$. The optical disturbance at the point P_0 due to a field defined over a planar surface S_0 is expressed as [15, 16]

$$\psi(\mathbf{r}_0) = -\frac{1}{2\pi} \int\limits_{S_0} \psi(\mathbf{r}_S)(jk - \frac{1}{|\mathbf{r}_{0S}|}) \frac{\exp(jk|\mathbf{r}_{0S}|)}{|\mathbf{r}_{0S}|} \cos(\theta) dS, \tag{2.1}$$

where $\cos(\theta) = \frac{z}{|\mathbf{r}_{0S}|}$, $|\mathbf{r}_{0S}| = \sqrt{(x_0 - x_S)^2 + (y_0 - y_S)^2 + {z_0}^2}$ and $k = \frac{2\pi}{\lambda}$. The expression given in Eq. 2.1 is in the form of a convolution integral,

$$\psi(\mathbf{r}_0) = \int\limits_{S_0} \psi(\mathbf{r}_S) h(\mathbf{r}_0 - \mathbf{r}_S) dS \tag{2.2}$$

where the input and the output signals are $\psi(\mathbf{r}_S)$ and $\psi(\mathbf{r}_0)$, respectively. The impulse response of the system that is used to describe the diffraction phenomena

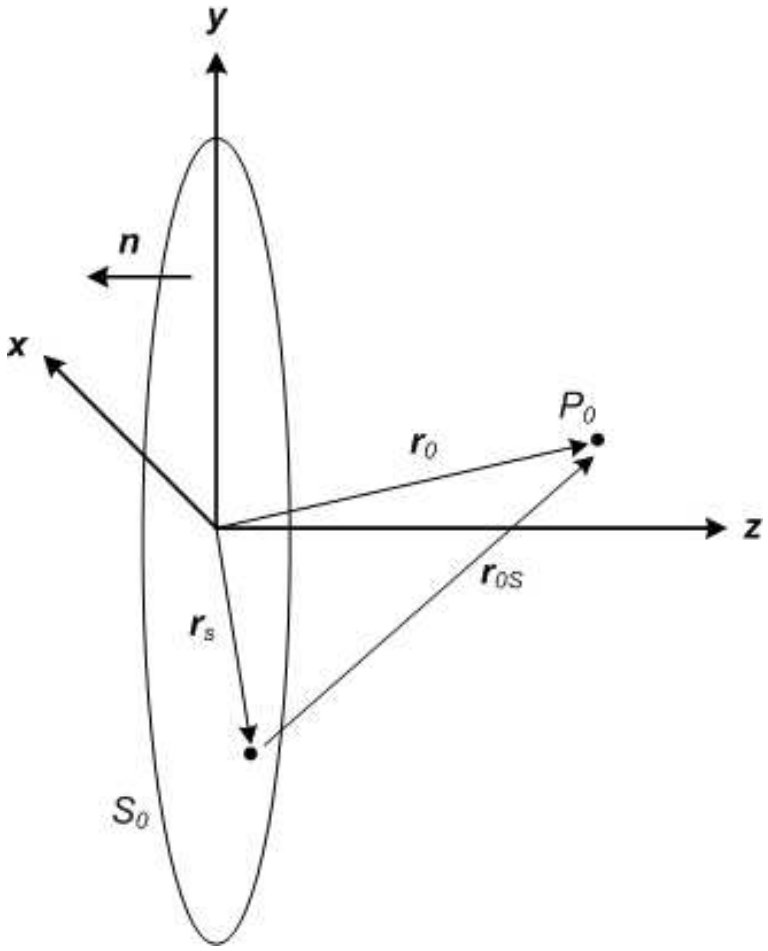

Figure 2.1: An illustration of the observation point P_0 and the planar surface S_0

is

$$h(\mathbf{r}) = -\frac{1}{2\pi}(jk - \frac{1}{|\mathbf{r}|})\frac{\exp(jk|\mathbf{r}|)}{|\mathbf{r}|}\cos(\theta). \tag{2.3}$$

The diffraction field relationship given in Eq. 2.1 is valid only for a planar surface, S_0. Therefore, the expression given in Eq. 2.1 will give erroneous results when it is used for the non-planar surfaces. The relation given by Eq. 2.1 can also be expressed in the frequency domain by employing convolution theorem and Weyl decomposition which is [16, 52–54]

$$\frac{\exp(jk|\mathbf{r}|)}{|\mathbf{r}|} = \frac{j}{2\pi}\int_{-\infty}^{\infty}\frac{\exp[j(k_x x + k_y y + k_z z)]}{k_z}dk_x dk_y, \text{ for } z \geq 0 \tag{2.4}$$

where k_x and k_y are the spatial frequencies of the propagating plane waves along x and y axes, respectively; and the spatial frequency along the z-axis, k_z, is a function of k_x and k_y, because of dealing with monochromatic diffraction fields.

The spatial frequency k_z is expressed as

$$k_z = \left\{ \begin{array}{ll} \sqrt{k^2 - {k_x}^2 - {k_y}^2}, & \text{if } k \geq {k_x}^2 + {k_y}^2 \\ j\sqrt{{k_x}^2 + {k_y}^2 - k^2}, & \text{if } k \leq {k_x}^2 + {k_y}^2 \end{array} \right\} \tag{2.5}$$

The derivative of the expression given in Eq. 2.4 is found as

$$\begin{aligned} \frac{\partial\left\{\frac{\exp(jk|\mathbf{r}|)}{|\mathbf{r}|}\right\}}{\partial z} &= (jk - \frac{1}{|\mathbf{r}|})\frac{\exp(jk|\mathbf{r}|)}{|\mathbf{r}|}\cos(\theta) \\ &= -\frac{1}{2\pi}\int_{-\infty}^{\infty} \exp[j(k_x x + k_y y + k_z z)]dk_x dk_y, \text{ for } z \geq 0 \end{aligned} \tag{2.6}$$

which is also taken into consideration as an inverse Fourier transform,

$$\begin{aligned} \frac{\partial\left\{\frac{\exp(jk|\mathbf{r}|)}{|\mathbf{r}|}\right\}}{\partial z} &= -\frac{1}{2\pi}\int_{-\infty}^{\infty} \exp(jk_z z)\exp[j(k_x x + k_y y)]dk_x dk_y, \text{ for } z \geq 0 \\ &= -2\pi\mathcal{F}^{-1}\big\{\exp(jk_z z)\big\}. \end{aligned} \tag{2.7}$$

By substituting the expression in Eq. 2.6 into the expression given in Eq. 2.1, we obtain

$$\begin{aligned} \psi(\mathbf{r}_0) &= \frac{1}{(2\pi)^2}\int_{S_0} \psi(\mathbf{r}_S)\int_{-\infty}^{\infty} \exp\{j[k_x(x_0 - x_S) + k_y(y_0 - y_S) + k_z z_0]\}dk_x dk_y dS \\ &= \frac{1}{(2\pi)^2}\int_{-\infty}^{\infty} \Psi(k_x, k_y)\exp[j(k_x x_0 + k_y y_0 + k_z z_0)]dk_x dk_y. \end{aligned} \tag{2.8}$$

The function $\Psi(k_x, k_y)$, defined in Eq. 2.8, is the Fourier transform of the field over the planar surface S_0 which is equal to $z = 0$,

$$\Psi(k_x, k_y) = \int_{S_0} \psi(\mathbf{r}_S)\exp[-j(k_x x_S + k_y y_S)]dS. \tag{2.9}$$

The expression given by Eq. 2.8 can be seen as an inverse Fourier transform. The diffraction field relationship given by Eq. 2.8 is called as the plane wave decomposition (PWD) and it can also be written as [16, 52–54]

$$\psi(x, y, z) = \mathcal{F}^{-1}\{\mathcal{F}[\psi(x, y, 0)]\exp\left[j({k^2 - {k_x}^2 - {k_y}^2})^{\frac{1}{2}}z\right]\} \tag{2.10}$$

where $\psi(x, y, 0)$ is the input field over the planar surface $z = 0$. The operator $\mathcal{F}$ denotes the Fourier transform and the inverse Fourier transform is shown as

$\mathcal{F}^{-1}$. Fourier transform of the input field gives the complex coefficients of the plane waves that forms the diffraction field over the entire space as

$$(2\pi)^2 A(k_x, k_y) = \mathcal{F}\Big\{\psi(x, y, 0)\Big\}. \tag{2.11}$$

The same diffraction field can be calculated by both PWD and RS diffraction integral when the condition $r \gg \lambda$ is satisfied [52, 53]. Such a condition causes elimination of the evanescent wave components in the input field. The approximation of omitting the evanescent waves can be seen in Eq. 2.1 by dropping of term $\frac{1}{|\mathbf{r}|}$. In this case the impulse response of the RS diffraction integral can be rewritten as

$$h_z(x, y) = \frac{1}{j\lambda} \frac{\exp(jk\sqrt{x^2 + y^2 + z^2})}{\sqrt{x^2 + y^2 + z^2}} \cos\theta. \tag{2.12}$$

The effect of discarding the evanescent waves can be seen in the frequency domain as having only k_x and k_y satisfying ${k_x}^2 + {k_y}^2 \leq k^2$. Then, the frequency response associated with the RS kernel is expressed as

$$h_z(x, y) = \mathcal{F}^{-1}\big\{ \exp\big[j(k^2 - {k_x}^2 - {k_y}^2)^{\frac{1}{2}} z\big]\big\}, \quad \sqrt{{k_x}^2 + {k_y}^2} \leq k. \tag{2.13}$$

The inverse Fourier transform of the evanescent part of the diffraction field is found as

$$-\frac{\exp\left(jk\sqrt{x^2 + y^2 + z^2}\right)}{(x^2 + y^2 + z^2)} \cos\theta = \mathcal{F}^{-1}\big\{ \exp\big[j(k^2 - {k_x}^2 - {k_y}^2)^{\frac{1}{2}} z\big]\big\}, \ \sqrt{{k_x}^2 + {k_y}^2} \geq k. \tag{2.14}$$

However, evanescent parts of the diffraction field left out from the diffraction field calculations in this dissertation, because we are dealing with only propagating waves.

PWD is an effective method to compute scalar optical diffraction, thus it is commonly used in diffraction field computation. PWD is not only used to compute diffraction field between two parallel planes but also it can be used to demystify the diffraction field relation between tilted planes as

$$\psi(\mathbf{Rx} + \mathbf{b}) = \frac{1}{4\pi^2} \mathcal{F}^{-1}{}_{\mathbf{k}' \to \mathbf{x}} \Big\{ 4\pi^2 \mathcal{F}_{\mathbf{x} \to \mathbf{k}}\{\psi(\mathbf{x})\}\Big|_{\mathbf{k} \to \mathbf{Rk}'} \exp(j(\mathbf{Rk}')^T \mathbf{b}) J(k_z, k'_z) \Big\} \tag{2.15}$$

where $\psi(\mathbf{x})$ denotes the diffraction field over 3D space and the position vector is shown by $\mathbf{x}$ [34, 55, 56]. The Jacobian term is shown as $J(k_z, k'_z)$ equal to $\frac{k_z}{k'_z}$. The rotation and transition are denoted by matrix $\mathbf{R}$ and vector $\mathbf{b}$, respectively.

The diffraction field relationship between two tilted planes can be expressed exactly as shown above without any approximations (except discarding the evanescent waves). Furthermore, fast computation of the expression given above can be achieved by using the fast Fourier transform (FFT). As a consequence of fast computation of the diffraction field between tilted planes, it can be used to compute the diffraction field of an object which is formed by planar patches. Diffraction field of each planar patch will be superposed to obtain the field emitted by the object. The expression given above can be employed in enlarging the viewing angle in a holographic imaging setup with multiple spatial light modulators (SLMs) which are not placed on the same plane. Also, similar viewing enlargement can be obtained by using single SLM with time-multiplexing vibrations around an axis.

The scalar diffraction field relationship between two tilted planes may provide advantages on both diffraction field computation due to an object and enlarging the viewing angle of a single SLM. Being a challenging problem, several methods are proposed to compute scalar optical diffraction between tilted planes. In the algorithm proposed by Rabal, Fourier transform was used to calculate the intensity pattern from a tilted plane onto another plane perpendicular to the initial beam propagation direction [57]. Leseberg and Frére are the first researchers employed Fresnel approximation to calculate the diffraction pattern of a tilted plane [27]. Then, they suggested another diffraction field computation method for the off-axis tilted objects [58]. Tommasi and Bianco proposed an algorithm to calculate the relation between the plane wave spectrum of the rotated planes [59]. They also used their algorithm to calculate the computer generated holograms of off-axis objects [60]. Then, they showed that their diffraction field computation

method can be applied to model a space-variant optical interconnect [61]. Then, a method which is based on Rayleigh-Sommerfeld scalar diffraction integral was presented by Delen and Hooker. The method proposed by Delen and Hooker calculates full-scalar diffraction [62]. Matsushima, Schimmel and Wyrowski uses the same scalar diffraction method as Delen and Hooker presented, but in addition Matsushima, Schimmel and Wyrowski used several interpolation algorithms in their method to decrease the error on the calculated field [33]. The method proposed by Delen and Hooker was improved to solve more general scenarios in [34,55,56]. The improved method provides to have a tilt around x-axis and/or y-axis for the planes on which diffraction fields are defined. Moreover, the observation plane can be placed at further distances. The method presented in [34,55,56] can also be used to obtain the diffraction pattern of 3D objects. Furthermore, an analysis on the effect of using discrete Fourier transform in calculation of the diffraction fields between tilted planes is given in [34].

2.2 Discretization of Diffraction Field

The input field is taken as a bandlimited spatial function, whose bandlimit is within $\pm k$. This constraint comes from dealing with propagating monochromatic waves having wavelength λ, hence we can not have a harmonic component in the transverse plane which has a higher frequency than $\frac{1}{\lambda}$*cycles / unit length* [16, 26, 34]. In some cases, further restrictions on the bandwidth along the transverse direction x and y are imposed. For instance, k_x and k_y can be restricted to be $-B_x \leq k_x < B_x$ and $-B_y \leq k_y < B_y$, where $B_x, B_y \leq k$ [1, 34, 55, 56, 63–68]. Thus, k_x and k_y may assume any real value only within this allowed interval. To get a manageable numerical simulations, a finite number N of possible values for both of k_x and k_y is used. One possibility of choosing these values is to use uniform sampling, $k_x = l_x \frac{2B}{N}$ and $k_y = l_y \frac{2B}{N}$ where l_x, $l_y = -N/2, \cdots, N/2-1$ for even N and a similar formula for odd N. Discretization of the transverse

frequencies as described results in a field which is periodic along the transverse directions x and y, with a fundamental period $X = \frac{\pi N}{B}$. Therefore, a careful choice of simulation parameters is necessary if the consequences of this periodicity effect are to be minimized [1, 34, 55, 56, 63–68]. Therefore, the field becomes

$$\psi(x,y,z) = \sum_{m_x=0}^{N-1}\sum_{m_y=0}^{N-1} A_D(m_x,m_y)\exp\left[j(k^2 - {k_x}^2 - {k_y}^2)^{\frac{1}{2}}z\right] \exp\left(j\frac{2B}{N}m_x x\right)\exp\left(j\frac{2B}{N}m_y y\right) \tag{2.16}$$

where $A_D(m_x, m_y)$ is the complex amplitudes of the plane waves and

$$k_x = \begin{cases} 2\pi\frac{m_x}{X} & ,\ m_x \in [0, \frac{N}{2}) \\ 2\pi\frac{(m_x - N)}{X}, & m_x \in [\frac{N}{2}, N) \end{cases} \tag{2.17}$$

$$k_y = \begin{cases} 2\pi\frac{m_y}{X} & ,\ m_y \in [0, \frac{N}{2}) \\ 2\pi\frac{(m_y - N)}{X}, & m_y \in [\frac{N}{2}, N) \end{cases} . \tag{2.18}$$

This periodic and bandlimited function with a sampling period $X_s = \pi/B$, which is its Nyquist rate, yields N samples per period. Restricting our attention to these samples, $x = n_x X_s$, $y = n_y X_s$ and $z = pX_s$, where n_x and n_y are integers spanning one period, and p is the distance between the lines along the longitudinal direction z. The expression in Eq. 2.16 can be written as

$$\psi(n_x X_s, n_y X_s, pX_s) = \sum_{m_x=0}^{N-1}\sum_{m_y=0}^{N-1} A_D(m_x,m_y)\exp\left[j(k^2 - {k_x}^2 - {k_y}^2)^{\frac{1}{2}}pX_s\right] \exp\left(j\frac{2\pi}{N}m_x n_x\right)\exp\left(j\frac{2\pi}{N}m_y n_y\right) \tag{2.19}$$

where p denotes a real number [1, 34, 55, 56, 63–68]. Each frequency component m determines the propagation direction of the corresponding plane wave. The angles ϕ_x and ϕ_y, which are shown in Figure 2.2, denote the angles between the z axis and the propagation directions:

$$\phi_{m_x} = \begin{cases} \sin^{-1}\left(\frac{\lambda m_x}{N X_s}\right) & ,\ m_x \in [0, \frac{N}{2}) \\ \sin^{-1}\left(\frac{\lambda(m_x - N)}{N X_s}\right), & m_x \in [\frac{N}{2}, N) \end{cases} \tag{2.20}$$

$$\phi_{m_y} = \begin{cases} \sin^{-1}\left(\frac{\lambda m_y}{N X_s}\right) & ,\ m_y \in [0, \frac{N}{2}) \\ \sin^{-1}\left(\frac{\lambda(m_y - N)}{N X_s}\right), & m_y \in [\frac{N}{2}, N) \end{cases} . \tag{2.21}$$

Thus $m_x, m_y \in [0, \frac{N}{2})$ corresponds to the positive ϕ_x and ϕ_y angles, and $m_x, m_y \in [\frac{N}{2}, N)$ corresponds to the negative ϕ_x and ϕ_y angles [1, 34, 55, 56, 63–68]. The relation between k_z, m_x and m_y is

$$k_z = \left\{ \begin{array}{l} \frac{2\pi}{NX_s}\sqrt{\beta^2 - {m_x}^2 - {m_y}^2}, m_x, m_y \in [0, \frac{N}{2}) \\ \frac{2\pi}{NX_s}\sqrt{\beta^2 - (m_x - N)^2 - {m_y}^2}, m_x \in [\frac{N}{2}, N), m_y \in [0, \frac{N}{2}) \\ \frac{2\pi}{NX_s}\sqrt{\beta^2 - (m_x - N)^2 - (m_y - N)^2}, m_x \in [0, \frac{N}{2}), m_y \in [\frac{N}{2}, N) \\ \frac{2\pi}{NX_s}\sqrt{\beta^2 - (m_x - N)^2 - (m_y - N)^2}, m_x, m_y \in [\frac{N}{2}, N) \end{array} \right\} \quad (2.22)$$

where $\beta = \frac{NX_s}{\lambda}$ [1, 34, 55, 56, 63–68]. Therefore, the discrete kernel corresponding to the plane wave decomposition becomes,

$$H_p(m_x, m_y) = \left\{ \begin{array}{l} \exp\left(j\frac{2\pi}{N}\sqrt{\beta^2 - {m_x}^2 - {m_y}^2}\, p\right), m_x, m_y \in [0, \frac{N}{2}) \\ \exp\left(j\frac{2\pi}{N}\sqrt{\beta^2 - (m_x - N)^2 - {m_y}^2}\, p\right), m_x \in [\frac{N}{2}, N), m_y \in [0, \frac{N}{2}) \\ \exp\left(j\frac{2\pi}{N}\sqrt{\beta^2 - {m_x}^2 - (m_y - N)^2}\, p\right), m_x \in [0, \frac{N}{2}), m_y \in [\frac{N}{2}, N) \\ \exp\left(j\frac{2\pi}{N}\sqrt{\beta^2 - (m_x - N)^2 - (m_y - N)^2}\, p\right), m_x, m_y \in [\frac{N}{2}, N) \end{array} \right\} \quad (2.23)$$

and the resultant form of the discrete representation of the plane wave decomposition is

$$\psi_D(n_x, n_y, p) = \sum_{m_x=0}^{N-1} \sum_{m_y=0}^{N-1} A_D(m_x, m_y) H_p(m_x, m_y) \exp\left(j\frac{2\pi}{N} n_x m_x\right) \exp\left(j\frac{2\pi}{N} n_y m_y\right), \quad (2.24)$$

where $N^2 \cdot A_D(m_x, m_y)$ is the DFT of the sampled input field [1, 34, 55, 56, 63–68]. The variable n_x and n_y are restricted to the range $[0, N)$. Therefore, the discrete diffraction field can be expressed as

$$\psi_D(n_x, n_y, p) = DFT_{2D}^{-1}\Big\{ DFT_{2D}\{\psi(n_x, n_y, 0)\} H_p(m_x, m_y) \Big\}. \quad (2.25)$$

The computer generated holograms are based on computation of discrete diffraction field and interference of the diffraction field with a reference wave. In this chapter, we mainly concentrated on the fundamentals of the scalar optical diffraction. Also, we clarified that PWD and RS diffraction integral can only explain the diffraction field relationship when the given field is defined on a planar

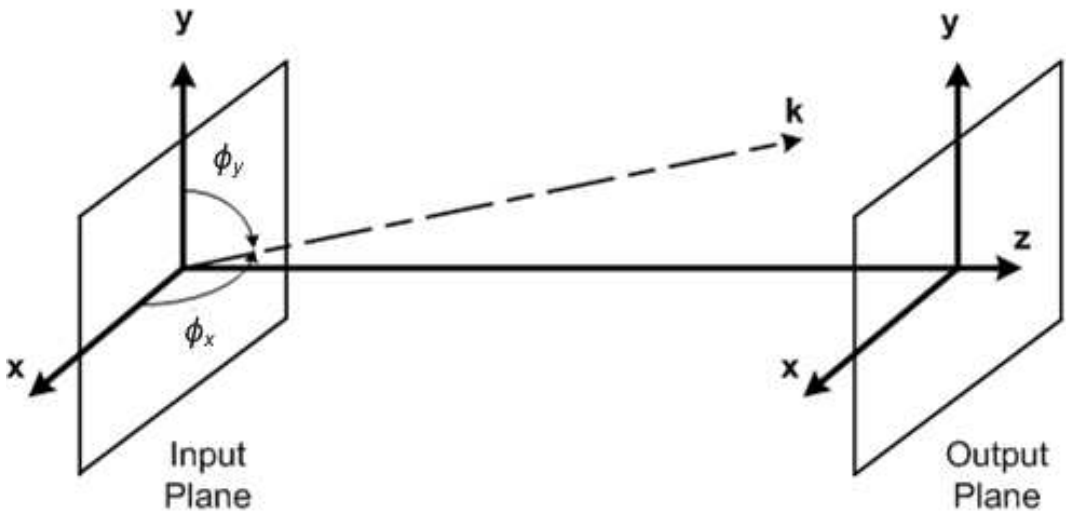

Figure 2.2: The vector **k** is the wave vector of the plane waves.

surface. We choose to eliminate the evanescent waves from the field calculations and it is the only approximation that we applied. Further approximations can be applied to RS diffraction integral to decrease the computational complexity, such as dealing only with paraxial waves [15, 16, 21, 26]. Also, these diffraction field relationships can be tailored according to the properties of the display device, thus it is possible to get sharper and high contrast reconstructed images. Some of these tailored algorithms are based on Rayleigh-Sommerfeld diffraction integral [22] or Fresnel approximation [69].

Chapter 3

Diffraction field calculation from the diffraction pattern over a manifold by a signal decomposition method

The derivation of the continuous scalar optical diffraction field relationship between two planar surfaces can be found in the literature [15, 16, 26]. Several diffraction field models such as Rayleigh-Sommerfeld (RS), plane wave decomposition (PWD), Fresnel and far-field are proposed to express the diffraction field relationship between two parallel planes. In Chapter 2, PWD and the relation between PWD and RS diffraction integral are presented. Fresnel diffraction field can be found from the RS diffraction integral kernel by applying the paraxial approximation. Please note that, these diffraction field models can be used only to describe the relationship between the field values over two planar planes as mentioned in Chapter 2. Again, as described in Chapter 2, the relationship between two slanted planes can also be based on these principles. However, the

computational procedures derived from straightforward application of the above-mentioned models will not give the exact diffraction field due to 3D objects which have curved surfaces. We assume that the objects can be optically represented by their surfaces which can be modeled as 2D manifolds in 3D space. The source model approaches, which are based on PWD, RS diffraction integral and Fresnel approximation, can be employed to compute diffraction fields due to these objects [42, 43, 70–74]. In those source model methods, it is assumed that superposition of the diffraction fields due to the point light sources from those sample points of the object, or from the planar patches forming the object, will give the desired diffraction field from the object. However, in most of the scenarios, there will be a significant deviation from the exact field, because the diffraction fields mutually couple; this is not taken care of by the employed source model formulation. In this work, we propose diffraction field calculation methods which will give the exact diffraction field due to the objects which need not to be defined on a planar surface. We also clearly indicate the flaws in commonly used faulty source model methods in Chapter 5.

An algorithm for computation of the continuous scalar optical diffraction field over the entire space due to the field given over a manifold is presented in this chapter. Manifold is used to indicate the surface on which the given diffraction field is defined. If enough amount of information is obtained from the diffraction field defined over the manifold, then we can reconstruct the diffraction field perfectly over the entire space.

3.1 Fundamentals of the proposed algorithm

A propagating monochromatic wave satisfies the wave equation,

$$\nabla^2 \exp(j\mathbf{k}^T\mathbf{x}) + k^2 \exp(j\mathbf{k}^T\mathbf{x}) = 0, \tag{3.1}$$

where the vector $\mathbf{x}$ is a position vector in 3D, $\mathbf{x} = [x, y, z]^T$. The vector $\mathbf{k}$ denotes the spatial frequencies along x, y and z axes, $\mathbf{k} = [k_x, k_y, k_z]^T$. The vector $\mathbf{k}$ determines the propagation direction of the plane wave. As a result of dealing with monochromatic waves, k_z is a function of k_x and k_y as,

$$k_z = \sqrt{k^2 - {k_x}^2 - {k_y}^2}. \tag{3.2}$$

Also, we assume that the diffraction field defined over the entire space can be decomposed into propagating planar waves,

$$\psi(\mathbf{x}) = \int_K A_{2D}(k_x, k_y) \exp(j\mathbf{k}^T\mathbf{x}) dk_x dk_y \tag{3.3}$$

where K is the frequency bandwidth of the field and $A_{2D}(k_x, k_y)$ is the complex amplitudes of the plane waves. As a result of this, we are dealing with a signal that is Fourier transformable, but this is not a too tight constraint. Furthermore, such signals satisfy the wave equation, because each plane wave is a solution of the wave equation.

Plane waves are also used as basis functions in the Fourier transform. Hence, the results from Fourier transform theory can be directly applied to the problem of finding complex amplitudes of the propagating plane waves. Furthermore, efficient signal processing tools related to Fourier theory can also be utilized.

The complex amplitudes of plane waves can be calculated by the inner product of the diffraction field over the space with the corresponding plane wave as

$$\begin{aligned} 4\pi^2 A_{2D}(k_x, k_y) &= \int_{S_0} \psi(\mathbf{x}) \exp(-j\mathbf{k}^T\mathbf{x}) dx dy \\ &= \langle \psi(\mathbf{x}), \exp(j\mathbf{k}^T\mathbf{x}) \rangle \Big|_{S_0}, \end{aligned} \tag{3.4}$$

where $\langle \cdot, \cdot \rangle$ denotes the inner product and the surface S_0 is the planar surface $z = 0$. The relation between the diffraction field within a volume and over its boundary surface can be obtained from the divergence theorem and the wave

equation as [15, 16],

$$\int_V \Big\{\psi(\mathbf{x})\nabla^2[\exp(-j\mathbf{k}^T\mathbf{x})] - \nabla^2(\psi(\mathbf{x}))\exp(-j\mathbf{k}^T\mathbf{x})\Big\}dV$$
$$= \oint_S \Big\{\psi(\mathbf{x})\frac{\partial[\exp(-j\mathbf{k}^T\mathbf{x})]}{\partial n} - \frac{\partial[\psi(\mathbf{x})]}{\partial n}\exp(-j\mathbf{k}^T\mathbf{x})\Big\}dS \tag{3.5}$$

where V is the volume we are interested in and S is the closed surface which is the boundary of V. The operator $\frac{\partial}{\partial n}$ stands for partial derivative along the outward normal direction at each point on S. The integrals in Eq. 3.5 will give zero, because the function in the volume integral is equal to zero as shown in [15, 16]. The reason of having zero valued function in the volume integral is dealing with source free volume. Then, the closed surface integral can be split into two manifolds. It is assumed that one of the surfaces is planar and the other one is a 2D curved surface that forms an orientable 2D manifold with the planar one. Thereafter, the relation between the surface integrals can be shown as,

$$\int_{S_0} \Big\{\psi(\mathbf{x})\frac{\partial[\exp(-j\mathbf{k}^T\mathbf{x})]}{\partial(-z)} - \frac{\partial[\psi(\mathbf{x})]}{\partial(-z)}\exp(-j\mathbf{k}^T\mathbf{x})\Big\}dxdy$$
$$= -\int_{S_a} \Big\{\psi(\mathbf{x})\frac{\partial[\exp(-j\mathbf{k}^T\mathbf{x})]}{\partial n} - \frac{\partial[\psi(\mathbf{x})]}{\partial n}\exp(-j\mathbf{k}^T\mathbf{x})\Big\}dS \tag{3.6}$$

where S_0 is the planar surface $z = 0$ and S_a stands for the complement part to get closed surface S; i.e., $S = S_0 \cup S_a$. The surface outward normal of S_0 is the unit vector $-\hat{\mathbf{z}}$ and the surface unit outward normal for the S_a is $\hat{\mathbf{n}}$. The first integral is closely related to Fourier transform. It gives the coefficients of the plane wave $\exp(-j\mathbf{k}^T\mathbf{x})$,

$$\int_{S_0} [\psi(\mathbf{x})\frac{\partial(\exp(-j\mathbf{k}^T\mathbf{x}))}{\partial(-z)} - \frac{\partial(\psi(\mathbf{x}))}{\partial(-z)}\exp(-j\mathbf{k}^T\mathbf{x})]dxdy = (j2k_z)(2\pi)^2 A_{2D}(k_x, k_y). \tag{3.7}$$

Derivation of the result given in Eq. 3.7 can be established by the expressions of the partial differential terms $\frac{\partial(\exp(-j\mathbf{k}^T\mathbf{x}))}{\partial(-z)}$ and $\frac{\partial(\psi(\mathbf{x}))}{\partial(-z)}$. Those partial derivatives

are found as

$$\frac{\partial[\exp(-j\mathbf{k}^T\mathbf{x})]}{\partial(-z)} = jk_z \exp(-j\mathbf{kx})\,, \tag{3.8}$$

$$\frac{\partial[\psi(\mathbf{x})]}{\partial(-z)} = -\int\limits_K jk'_z A_{2D}(k'_x, k'_y)\exp(j\mathbf{k}'\mathbf{x})dk'_x dk'_y. \tag{3.9}$$

Then, substituting the expressions in Eq. 3.8, Eq. 3.9 and Eq. 3.4 into the left hand side of Eq. 3.7, and we obtain

$$\begin{aligned}\int\limits_{S_0} \Big\{\psi(\mathbf{x})\frac{\partial[\exp(-j\mathbf{k}^T\mathbf{x})]}{\partial(-z)} - \frac{\partial(\psi(\mathbf{x}))}{\partial(-z)}\exp(-j\mathbf{k}^T\mathbf{x})\Big\}dxdy \\ = \int\limits_{S_0} \Big\{\psi(\mathbf{x})(jk_z)\exp(-j\mathbf{k}^T\mathbf{x}) \\ + \int\limits_K [(jk'_z)A_{2D}(k'_x, k'_y)\exp(j\mathbf{k'}^T\mathbf{x})]dk'_x dk'_y \exp(-j\mathbf{k}^T\mathbf{x})\Big\}dxdy.\end{aligned} \tag{3.10}$$

Then, we use the decomposition of the diffraction field as given by Eq. 3.3 over the manifold S_0 in Eq. 3.10 and we find

$$\begin{aligned}&\int\limits_{S_0} \Big\{\psi(\mathbf{x})\frac{\partial[\exp(-j\mathbf{k}^T\mathbf{x})]}{\partial(-z)} - \frac{\partial(\psi(\mathbf{x}))}{\partial(-z)}\exp(-j\mathbf{k}^T\mathbf{x})\Big\}dxdy \\ &= \int\limits_{S_0} \Big\{ \int\limits_K [A_{2D}(k'_x, k'_y)\exp(j\mathbf{k'}^T\mathbf{x})]dk'_x dk'_y (jk_z)\exp(-j\mathbf{k}^T\mathbf{x}) \\ &+ \int\limits_K [jk'_z A_{2D}(k'_x, k'_y)\exp(j\mathbf{k'}^T\mathbf{x})]dk'_x dk'_y \exp(-j\mathbf{k}^T\mathbf{x})\Big\}dxdy.\end{aligned} \tag{3.11}$$

After then, we change the order of the integrals,

$$\begin{aligned}&\int\limits_{S_0} \Big\{\psi(\mathbf{x})\frac{\partial[\exp(-j\mathbf{k}^T\mathbf{x})]}{\partial(-z)} - \frac{\partial(\psi(\mathbf{x}))}{\partial(-z)}\exp(-j\mathbf{k}^T\mathbf{x})\Big\}dxdy \\ &= \int\limits_K A_{2D}(k'_x, k'_y)j(k_z + k'_z)\int\limits_{S_0}[\exp(j(\mathbf{k}' - \mathbf{k})^T\mathbf{x})dxdy]dk'_x dk'_y \\ &= \int\limits_K j(k_z + k'_z)(2\pi)^2 A_{2D}(k'_x, k'_y)\delta(\mathbf{k}' - \mathbf{k})dk'_x dk'_y \\ &= j(2k_z)(2\pi)^2 A_{2D}(k_x, k_y).\end{aligned} \tag{3.12}$$

From Eq. 3.6, the result of surface integral over S_a is found as,

$$\int_{S_a} \left(\psi(\mathbf{x}) \Big\{ \hat{\mathbf{n}} \cdot \nabla[\exp(-j\mathbf{k}^T\mathbf{x})] \Big\} - \exp(-j\mathbf{k}^T\mathbf{x}) \Big\{ \hat{\mathbf{n}} \cdot \nabla[\psi(\mathbf{x})] \Big\} \right) dS = (j2k_z)(2\pi)^2 A_{2D}(k_x, k_y). \quad (3.13)$$

The surface integral over S_a in Eq. 3.13 will provide to calculate complex coefficients of the plane waves from the diffraction data over S_a. However, to calculate the complex coefficients of the plane waves by Eq. 3.13, the directional derivative of the diffraction field, $\Big\{ \hat{\mathbf{n}} \cdot \nabla[\psi(\mathbf{x})] \Big\}$, over the manifold S_a has to be known, but it is not given. Only the manifold over the space and the diffraction field on the manifold are given. As result of this, Eq. 3.13 can not be performed straightforwardly, thus an alternative solution is proposed. A possible procedure to compute the field over the entire space from the given diffraction field over a manifold S_a can be based on the intersections of the 3D functions, $\exp(j\mathbf{k}^T\mathbf{x})$, by the manifold S_a. However, such intersections of the planes waves by S_a may not form an orthogonal 2D functions. Therefore, orthogonalization is needed in the diffraction field computation process. Analysis over a lower dimensional simple scenario will be helpful to clarify why the complex exponentials may not form an orthogonal functions on S_a and such an analysis can be found in Appendix A. Orthogonal functions are derived from the non-orthogonal functions which are the intersections of $\exp(j\mathbf{k}^T\mathbf{x})$ by the manifold S_a.

In this work, field and source model methods which are used to calculate diffraction field over the entire space from the given field on a manifold are investigated. In the field model, the diffraction field over the entire space is expressed as

$$\hat{\psi}(\mathbf{x}) = \int_K \hat{A}_{2D}(k_x, k_y) \exp(j\mathbf{k}^T\mathbf{x}) dk_x dk_y \quad (3.14)$$

where

$$\hat{A}_{2D}(k_x, k_y) = \underset{A_{2D}(k_x,k_y)}{\arg\min} \Big\{ \int_{S_a} \Big| \psi(\mathbf{x}) - \int_K A_{2D}(k_x, k_y) \exp(j\mathbf{k}^{\mathbf{T}}\mathbf{x}) dk_x dk_y \Big|^2 dS \Big\} \quad (3.15)$$

where $A_{2D}(k_x, k_y)$ denotes the complex amplitudes of the plane waves which are used as basis functions to decompose the field $\psi(\mathbf{x})$ over the entire space. The estimated complex amplitudes of the plane waves that provide the minimization of the difference between the estimated and the given fields is shown as $\hat{A}_{2D}(k_x, k_y)$. As a result of numerical issues, we assume that the diffraction field over the entire space is formed by finite number of propagating plane waves as

$$\psi(\mathbf{x}) = \sum_{\mathbf{k}_M} A_{2D}(k_{m_x}, k_{m_y}) \exp(j\mathbf{k}_M^T \mathbf{x}) \tag{3.16}$$

where $\mathbf{k}_M = [k_{m_x}, k_{m_y}, k_{m_z}]^T$. As a result of dealing with monochromatic waves, k_{m_z} is a function of k_{m_x} and k_{m_y} as $k_{m_z} = \sqrt{k^2 - {k_{m_x}}^2 - {k_{m_y}}^2}$. The spatial frequencies k_{m_x} and k_{m_y} are defined in a discrete set as $k_{m_x}, k_{m_y} \in [-M/2, M/2)$. Then, the least square problem given in Eq. 3.15 is expressed as

$$\hat{A}_{2D}(k_{m_x}, k_{m_y}) = \underset{A_{2D}(k_{m_x}, k_{m_y})}{\arg\min} \left\{ \int_{S_a} \left| \psi(\mathbf{x}) - \sum_{\mathbf{k}_M} A_{2D}(k_{m_x}, k_{m_y}) \exp(j\mathbf{k}_M^T \mathbf{x}) \right|^2 dS \right\} \tag{3.17}$$

As given in Eq. 3.16, the field over the manifold is formed by the propagating plane waves. The minimization of the least square error between the original field and the estimated field over the manifold is achieved according to the decomposition of the field over the functions which are found as the intersections of the propagating plane waves by the manifold. The complex amplitudes of the plane waves are estimated according to the algorithm presented in the following subsection. The estimation of the diffraction field over the manifold is obtained as

$$\hat{\psi}(\mathbf{x}) = \sum_{\mathbf{k}_M} \hat{A}_{2D}(k_x, k_y) \exp(j\mathbf{k}_M^T \mathbf{x}) \tag{3.18}$$

3.2 Decomposition onto an orthogonalized basis function set

Plane waves, whose superposition form the diffraction field over the entire space, generate an orthogonal 3D basis function set over the entire 3D space. However,

when they are intersected by an arbitrary orientable manifold, the resultant 2D functions corresponding to plane waves may not be orthogonal. Therefore, to compute the complex coefficients of the plane waves, we use Gram-Schmidt orthogonalization method to get an orthogonal basis function set [75]. Then, we can easily define proper inner products to compute the complex coefficients of the plane waves.

For illustration and evaluation purposes, a simple numerical simulation is designed. In this simulation, for simplicity, we deal with 1D objects and fields over the entire 2D space due to these 1D objects. Extension of the method for the 2D objects in 3D space is feasible, but there will be some numerical issues due to the larger data sets. Nevertheless, the method for the 3D space is presented at the end of this section, together with possible numerical problems that can be encountered. As a result of numerical concerns, we assume that the diffraction field is formed by a finite number of plane waves. Then, the diffraction field over 1D manifold can be expressed as,

$$\psi(\mathbf{x}) = \sum_{k_{m_x}} A_{1D}(k_{m_x}) \exp(j\mathbf{k}_M^T \mathbf{x}) \tag{3.19}$$

where $\mathbf{x}$ denotes the 1D manifold over 2D space, $\mathbf{x} = [x, z(x)]^T$ and the spatial frequencies are shown as $\mathbf{k}_M = [k_{m_x}, k_{m_z}]^T$ where $k_{m_z} = \sqrt{k^2 - {k_{m_x}}^2}$. Eq. 3.19 can be written in more compact form using matrix vector notation as,

$$\boldsymbol{\psi} = \boldsymbol{\Phi}\mathbf{a} \tag{3.20}$$

where $\boldsymbol{\psi}$ is the vector that represents diffraction field along the manifold. The vector $\mathbf{a}$ is the complex coefficients of the plane waves that we want to compute. Matrix $\boldsymbol{\Phi}$ is the system matrix formed by projection of the plane waves on the manifold as,

$$\begin{aligned} \boldsymbol{\Phi} &= \left[\exp(j{\mathbf{k}_1}^T\mathbf{x}) \,\middle|\, \exp(j{\mathbf{k}_2}^T\mathbf{x}) \,\middle|\, \ldots \,\middle|\, \exp(j{\mathbf{k}_M}^T\mathbf{x}) \right] \\ &= \left[\boldsymbol{\phi}_1 | \boldsymbol{\phi}_2 | \ldots | \boldsymbol{\phi}_M \right]. \end{aligned} \tag{3.21}$$

The matrix $\mathbf{\Phi}$ has M column vectors, denoted by the vectors $\boldsymbol{\phi}_i$. As mentioned above, the plane waves along the manifold are not orthogonal to each other in most of the scenarios. Therefore, we used Gram-Schmidt orthogonolization to form a set of orthogonal functions. After having the orthogonalization of the functions along the manifold, Eq. 3.20 can be expressed as,

$$\boldsymbol{\psi} = \mathbf{QRa} \tag{3.22}$$

where the columns of the matrix $\mathbf{Q}$ form the orthogonal basis functions that describes the system. The matrix $\mathbf{Q}$ has M column vectors as

$$\mathbf{Q} = [\ \mathbf{q}_1 \,|\, \mathbf{q}_2 \,|\, \ldots \,|\, \mathbf{q}_M\ ]. \tag{3.23}$$

The matrix $\mathbf{R}$ is an upper triangular matrix. Inner product of $\boldsymbol{\psi}$ by the complex conjugate of the orthogonal basis functions will provide possible solution to the complex coefficients of the plane waves as,

$$\mathbf{Q}^H\boldsymbol{\psi} = \mathbf{Ra}. \tag{3.24}$$

Back-substitution can be used to calculate the elements of the vector $\mathbf{a}$, because $\mathbf{R}$ is an upper triangular matrix, but back-substitution may not provide robust reconstruction generally. Therefore, we use singular value decomposition of $\mathbf{R}$ in reconstruction of the complex amplitudes of the plane waves. Then, the linear relation between the diffraction field on the manifold S_a and the complex coefficients of the propagating plane waves is expressed as

$$\mathbf{Q}^H\boldsymbol{\psi} = \mathbf{U\Sigma V}^H\mathbf{a} \tag{3.25}$$

where $\mathbf{U}$ is the eigenvectors of $\mathbf{RR}^H$ and $\mathbf{V}$ is the eigenvectors of $\mathbf{R}^H\mathbf{R}$. The diagonal elements of matrix $\mathbf{\Sigma}$ are the eigenvalues of the matrix $\mathbf{R}$. Robust reconstruction of the complex coefficients of the plane waves is obtained by discarding the eigenvalues which are smaller than the computational machine error. The elements of the diagonal matrix $\mathbf{\Sigma}^{-1}$ are computed as $\frac{1}{\lambda_i}$ where λ_i is the i^{th} diagonal element of matrix $\mathbf{\Sigma}$. Therefore, such a compensation is needed not

to amplify the computational machine error over the eigenvalues. Compensated solution of the vector $\mathbf{a}$ is

$$\mathbf{a} = \mathbf{V}\boldsymbol{\Sigma}^{-1}\mathbf{U}^{H}\mathbf{Q}^{H}\psi. \tag{3.26}$$

The implementation of the expression given Eq. 3.26 is summarized by the flow chart shown in Figure 3.1.

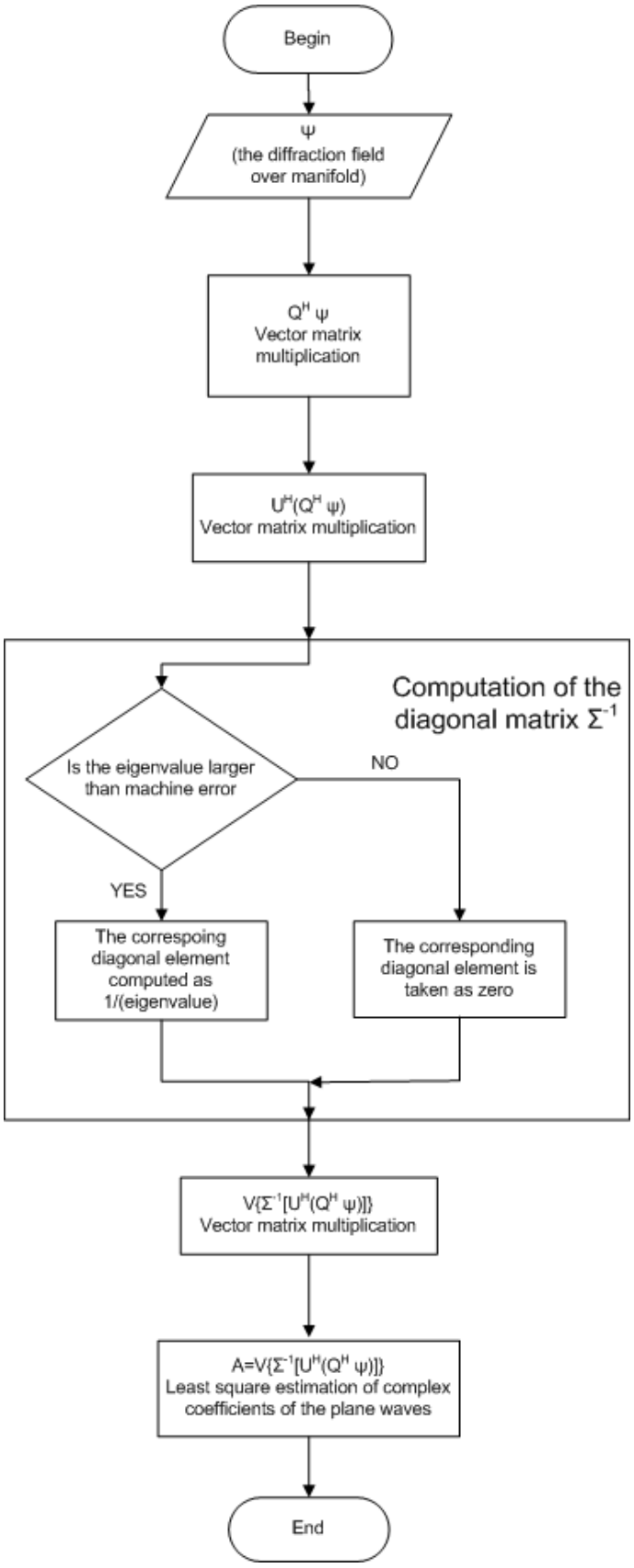

Figure 3.1: Flow chart of the implemented algorithm given by Eq. 3.26

To perform the discrete calculations in the presented algorithm, the samples of diffraction field defined over the manifold are received as input. To take many samples results in a large memory allocation and an increase in the computational complexity. The number of samples, that is needed to get perfect reconstruction of the complex amplitudes of the plane waves, is determined by the number of plane waves used in generation of the diffraction field over the entire space.

The method proposed in this section can also seen as an atomic decomposition. Furthermore, several other decomposition methods can be employed, such as method of frames, matching pursuit and basis pursuit [76]. It is assumed that the diffraction field over the manifold is generated by a linear superposition of the signals which are the intersection of the plane waves over the manifold. However, the lack of orthogonality poses a problem during reconstruction of the complex amplitudes of the plane waves. Therefore, we form a new set of functions which are orthogonal over the manifold. Then, we can calculate the complex amplitudes of the propagating planes that forms the diffraction field over the entire space by employing the generated orthogonal basis functions.

In the first simple simulation, a 2D diffraction field due to a 1D object is considered. Figure 3.2 shows the implemented scenario.

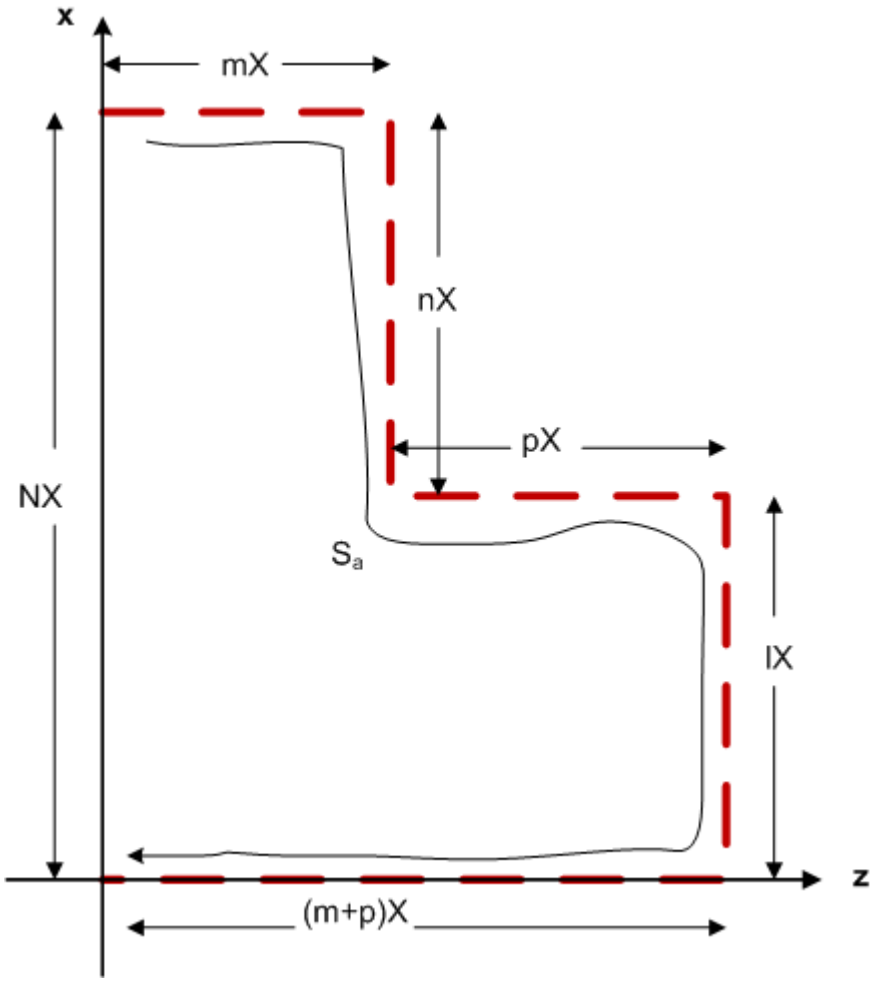

Figure 3.2: Implemented scenario of reconstruction of the entire diffraction field from the field given along 1D manifold S_a.

The manifold S_a and the x-axis form a closed loop. We assumed periodic patterns along the transversal axis which is chosen as x-axis in this scenario, because of the numerical aspects: the period is NX. The variable X is used to control physical distances between consecutive samples and it is taken as $\lambda/2$ for this scenario and the wave length λ is chosen as $0.5\,\mu m$. Larger sampling step sizes can be used if the bandwidth is taken smaller than $\frac{1}{\lambda}$ *cycles / unit length* which is the maximum possible wavelength for propagating waves. Furthermore, we assume that the field over the entire space is formed by $N = 256$ propagating plane waves and their propagating directions are defined by the variable k_{m_x},

which is $k_{m_x} \in [-\frac{N}{2}, \frac{N}{2})$, given in Eq. 3.19. The variables m, n, p and l are chosen as 100, 128, 125, 128, respectively. The diffraction field over the entire space is computed due to a synthetic signal on the reference line which is given as $z = 0$. The lines along the longitudinal axis has 256 samples. The synthetic signal on the reference line is chosen as a unit square pulse whose width is $\frac{1}{8}$ of the period NX along the transversal axis. An illustration of the diffraction field over the 2D space is given in Figure 3.3.

Figure 3.3: Magnitude of the diffraction field computed due to a synthetic signal which is a square pulse of 32 samples located at the center of the reference line of length 256 samples. To see the diffraction along the z-axis, the depth of the space is two times longer than the extend of the field along transversal axis.

These plane waves are intersected by the manifold S_a. Real parts of the cross-sections of the plane waves along the manifold S_a can be seen in Figures 3.4 and 3.5, for two of the 256 plane waves.

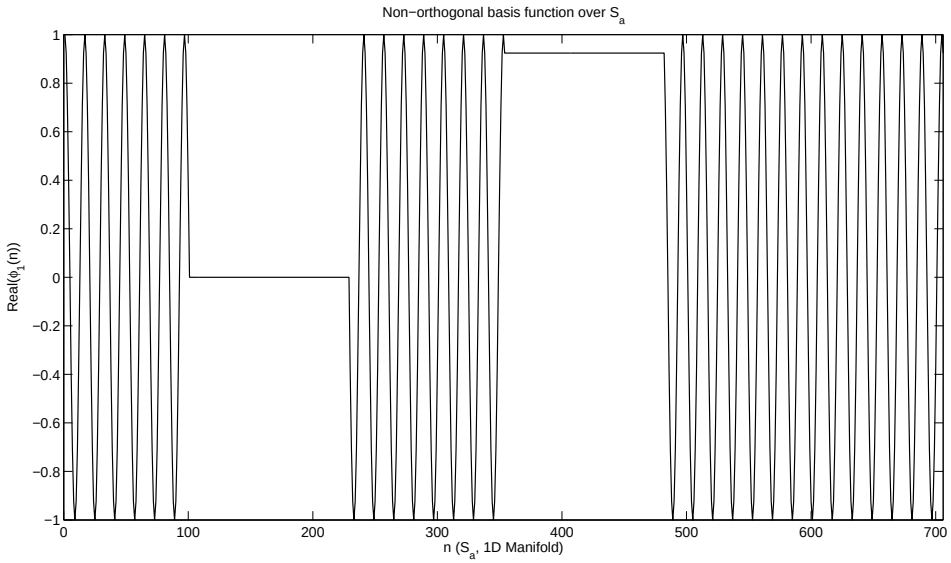

(a)

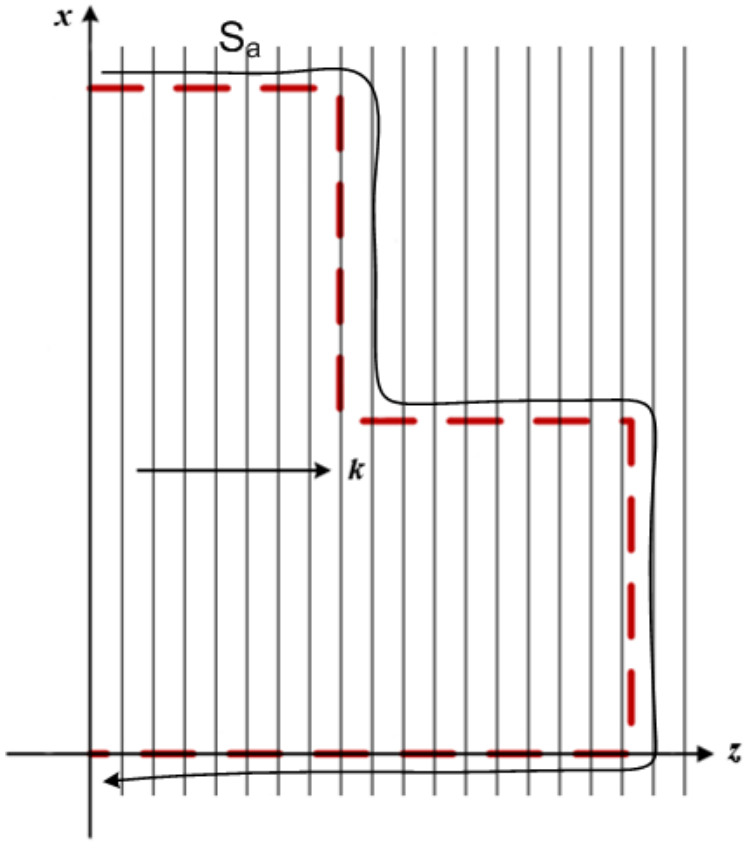

(b)

Figure 3.4: (a) Real part of the propagating plane waves intersected by the 1D manifold S_a (b) Corresponding propagating plane wave.

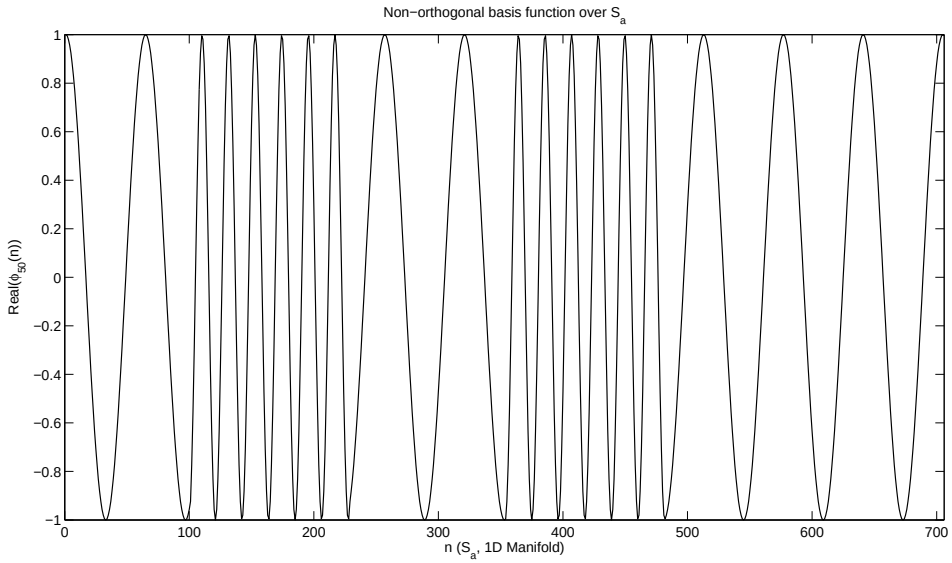

(a)

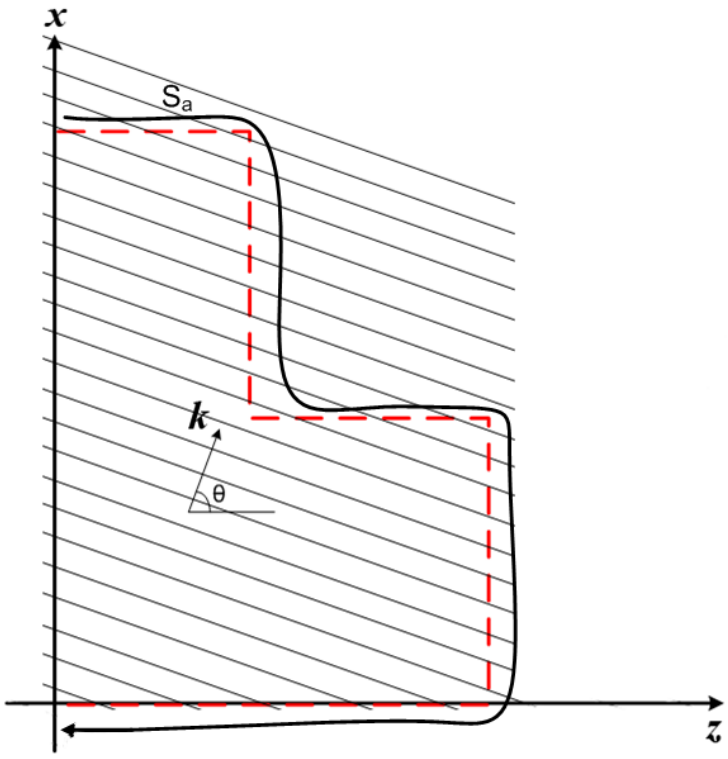

(b)

Figure 3.5: (a) Real part of the propagating plane waves intersected by the 1D manifold S_a (b) Corresponding propagating plane wave.

After performing Gram-Schmidt orthogonalization of these plane waves along the manifold, we obtain a set of orthogonal functions. Real parts of the orthogonal basis functions that are related to the functions given in Figures 3.4 and 3.5, are shown in Figure 3.6.

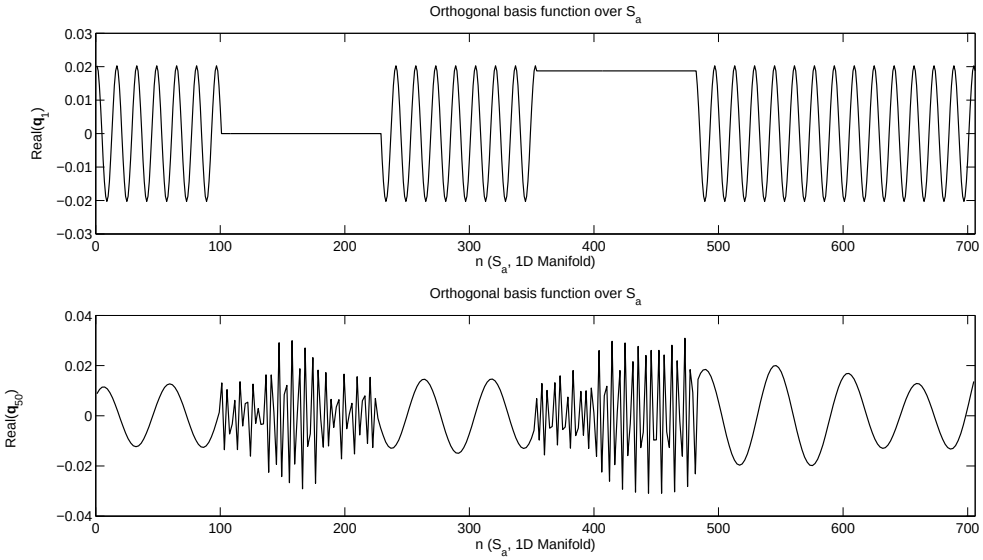

Figure 3.6: Orthgonalized functions along the manifold S_a

Then, the complex coefficients of the plane waves are obtained by Eq. 3.26. In Figure 3.7, the magnitudes of the reconstructed coefficients of the plane waves that form the diffraction field over the space are illustrated. Also, the magnitudes of the differences between the initial and the reconstructed coefficients are shown in Figure 3.7.

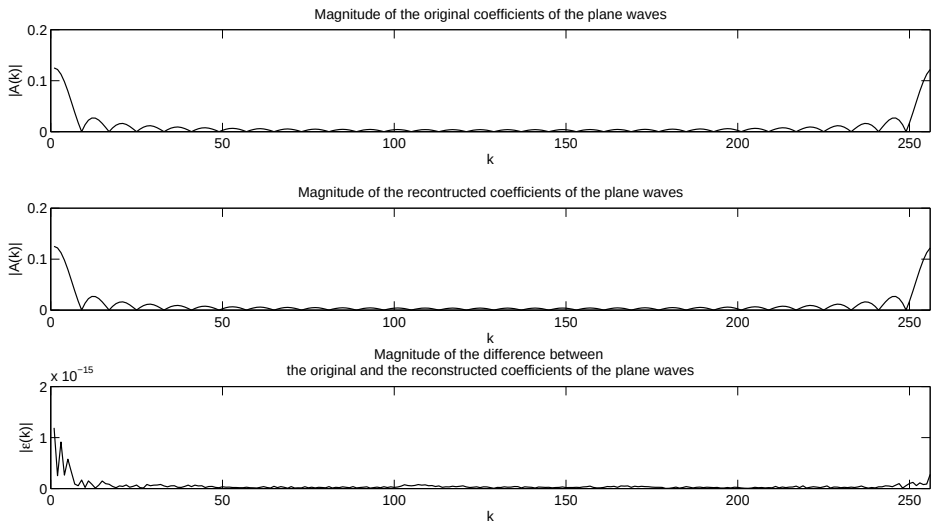

Figure 3.7: Magnitude of the coefficients that form the initial diffraction field over the space. Magnitude of the reconstructed coefficients. Magnitude of the difference between the initial and the reconstructed coefficients.

Both figures represent discrete values for $k_{m_x} \in [-\frac{N}{2}, \frac{N}{2})$ corresponding to plane wave components of the diffraction field, but figures plotted as continuous graphs by using linear interpolation for convenience. Then, the diffraction field along the reference line is reconstructed from the intersections of the plane waves along the reference line. The original and the reconstructed fields are shown in Figure 3.8. The magnitude of the difference between the original and the reconstructed fields is also given in Figure 3.8.

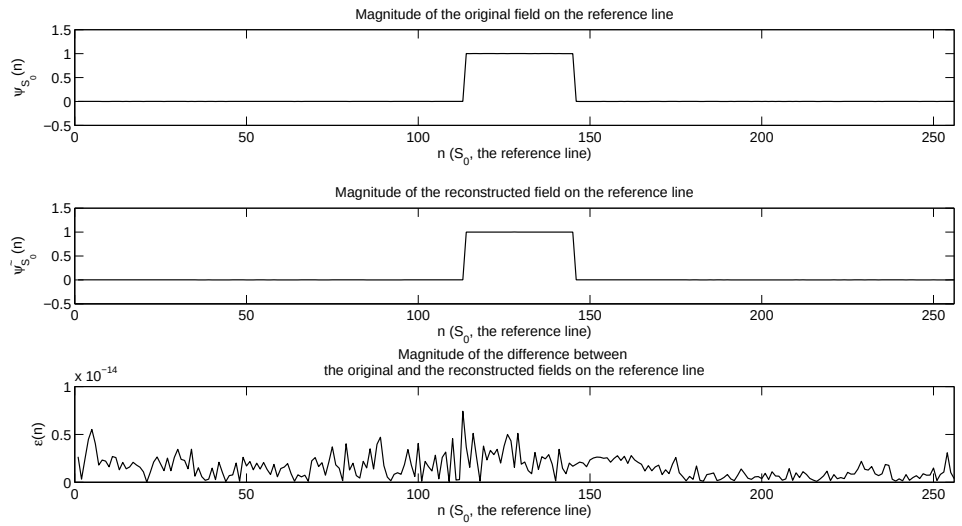

Figure 3.8: Original diffraction field on the manifold S_0. The reconstructed field on S_0 from computed coefficients by using the diffraction field over the manifold. The magnitude of the difference between the original and the reconstructed fields on S_0.

From the reconstructed field along the reference line, the diffraction field along the manifold S_a is computed, as well. Reconstructed field and its difference from the original field are shown in Figure 3.9.

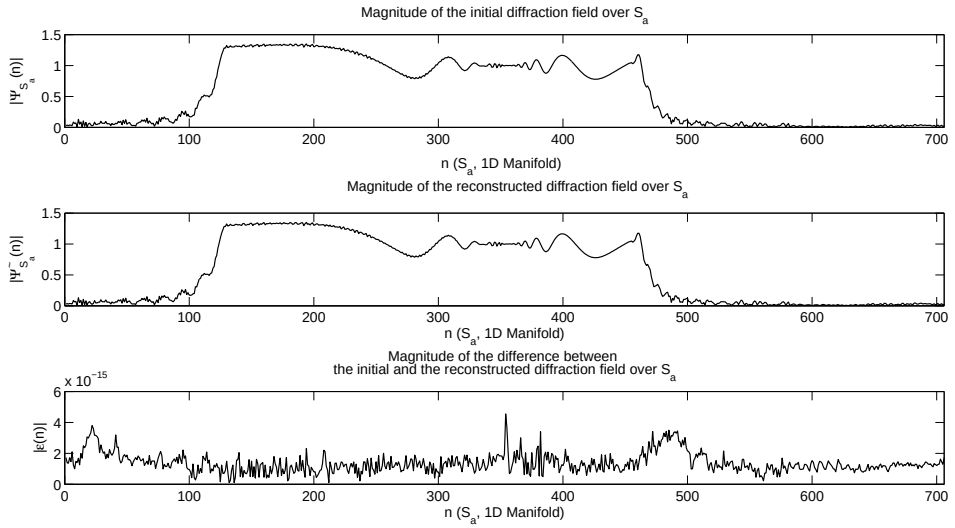

Figure 3.9: Original diffraction field on the manifold S_a. The reconstructed field on S_a from computed coefficients by using the diffraction field over the manifold. The magnitude of the difference between the original and the reconstructed fields on S_a.

In the second scenario, 1D manifold is formed by two straight lines with different angles. In Figure 3.10, an illustration of the manifold S_a is shown.

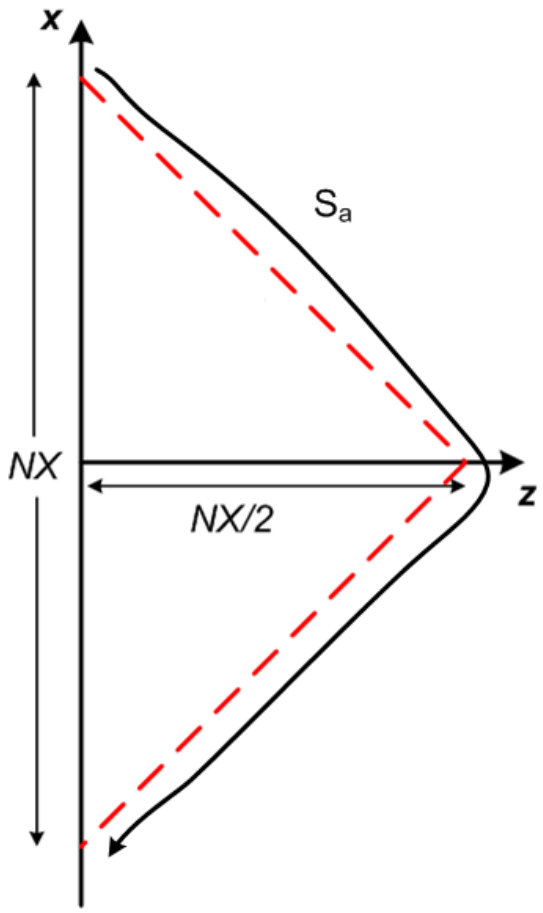

Figure 3.10: Illustration of the manifold S_a over the 2D space.

In this scenario, the sampling period along the manifold is changed to $\frac{\lambda}{\sqrt{2}}$ because in some scenarios, having at least N samples over the manifold S_0 can be enough to reconstruct the field over the manifold S_a. The employed wave length is again chosen as $0.5\,\mu m$. The real part of the signals obtained from the intersections of the propagating plane waves by the manifold S_a can seen from Figure 3.15, for two of the 256 propagating waves. The effect of the shape of the manifold on the intersected plane waves by the manifold is seen as instantaneous frequency shifts.

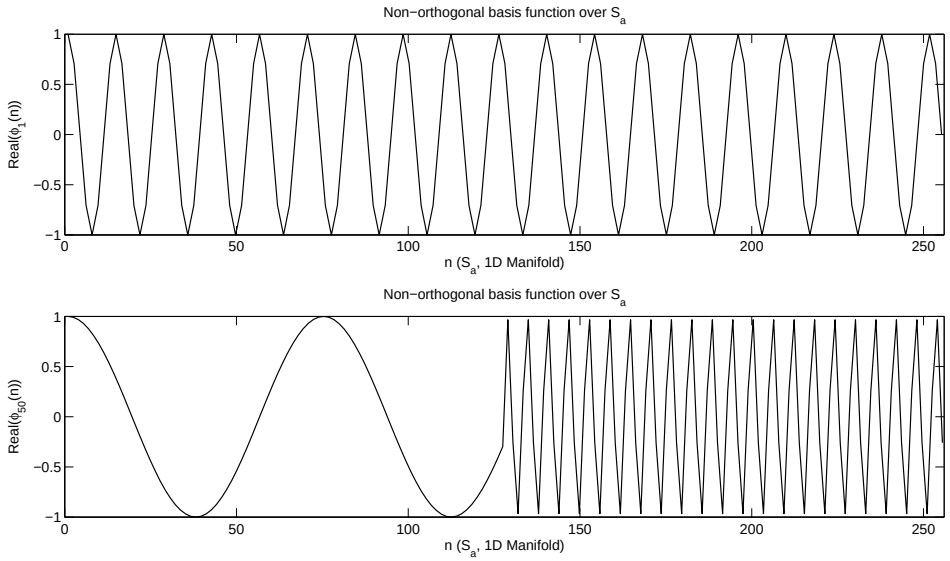

Figure 3.11: Real part of the propagating plane waves intersected by the 1D manifold S_a.

Real parts of the orthogonalized basis functions related to the functions given in Figure 3.15 are shown in Figure 3.12.

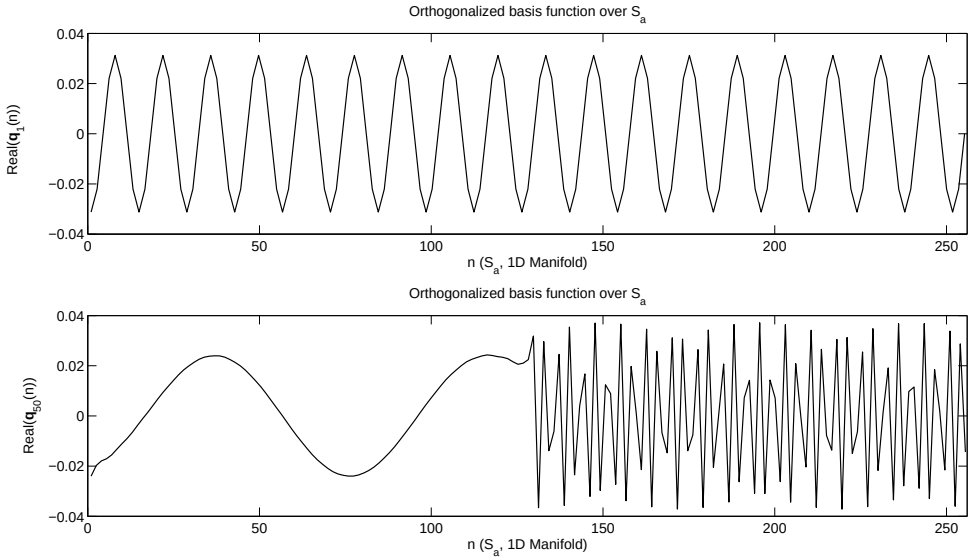

Figure 3.12: Real part of the orthogonalized functions along the manifold S_a.

The coefficients of the plane waves that form the diffraction field over the entire space are reconstructed from the given field over the manifold S_a by the proposed algorithm. Magnitude of the reconstructed coefficients can seen in Figure 3.13.

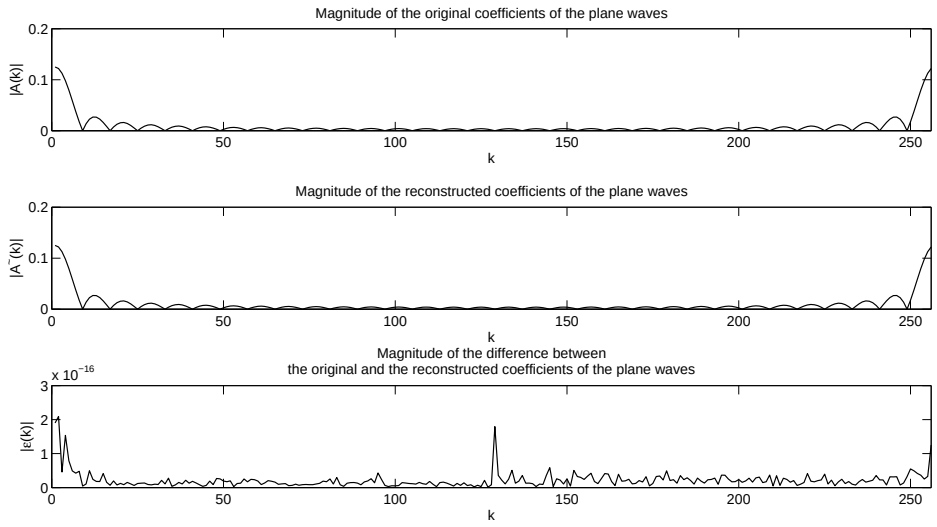

Figure 3.13: Magnitude of the coefficients that form the initial diffraction field over the space. Magnitude of the reconstructed coefficients. Magnitude of the difference between the initial and the reconstructed coefficients.

As it can be seen from Figure 3.14, the diffraction field over the reference line is again reconstructed perfectly. From the reconstructed field on the reference line, the diffraction field on the manifold is computed as shown in Figure 3.15. The field on the manifold is perfectly reconstructed.

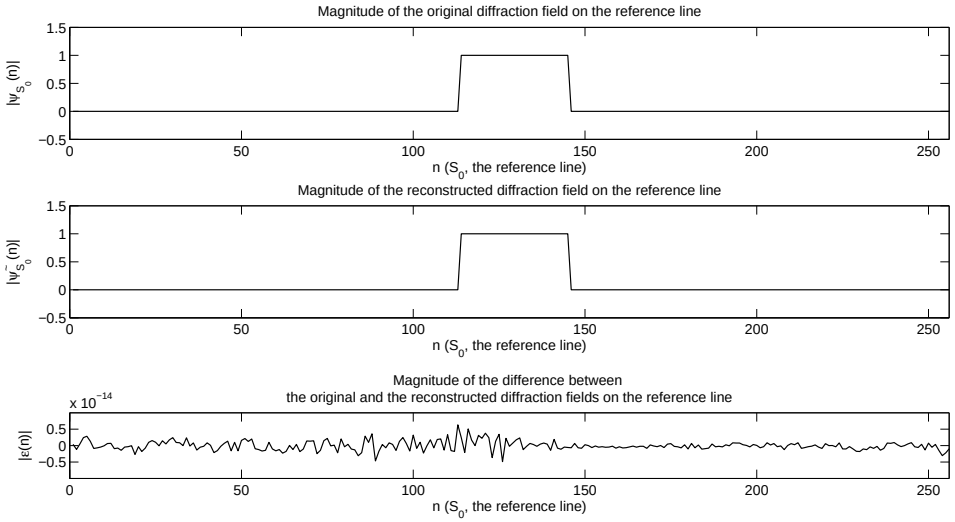

Figure 3.14: Original diffraction function on the manifold S_0. The reconstructed field on S_a from computed coefficients by using the diffraction field over the manifold. The magnitude of the diffraction between the original and the reconstructed fields on S_0.

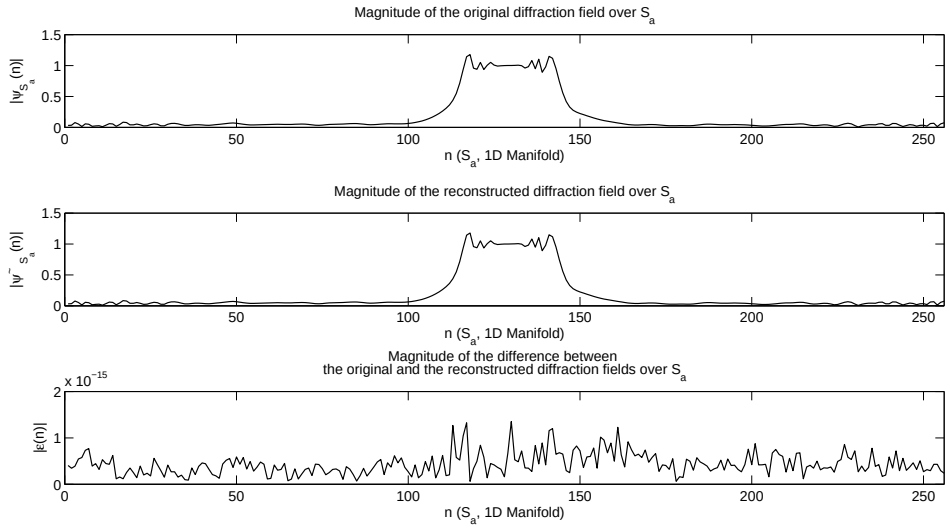

Figure 3.15: Original diffraction field on the manifold S_a. The reconstructed field on S_a from computed coefficients by using the diffraction field over the manifold. The magnitude of the difference between the original and the reconstructed fields on S_a.

In the third simulation, the same diffraction field shown in Figure 3.3 is used as the field over the entire space. The 1D manifold over the 2D space is changed as illustrated in Figure 3.16.

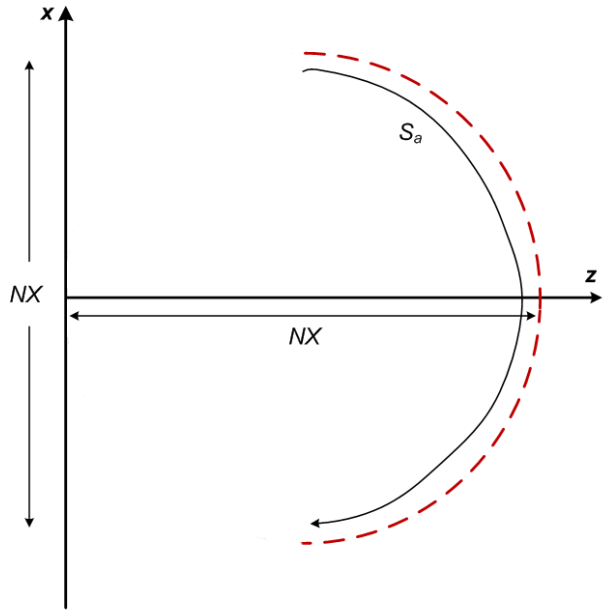

Figure 3.16: Illustration of the manifold S_a over the 2D space.

The manifold S_a is defined as a half circle whose diameter is taken as NX where N is equal to 256 and X is the spatial sampling period which is again taken as $\frac{\lambda}{2}$. The wave length in the implemented scenario is taken as $0.5\,\mu m$. Furthermore, the center of the circle is located at the point $(0, \frac{NX}{2})$. As a result of dealing with a curved manifold, the instantaneous frequencies of the signals obtained from the intersections of the propagating plane waves along the manifold S_a change according to the curvature of the manifold S_a. As an example, the frequency changes on the signals can be seen from the Figure 3.17. Again, the intersections of the plane waves along the manifold are not orthogonal. Therefore, to obtain an orthogonal basis function set, Gram-Schmidt orthogonalization is performed over intersected plane waves on S_a. As an illustration, real parts of the orthogonal basis functions obtained related to the functions, given in Figure 3.17, is shown in Figure 3.18.

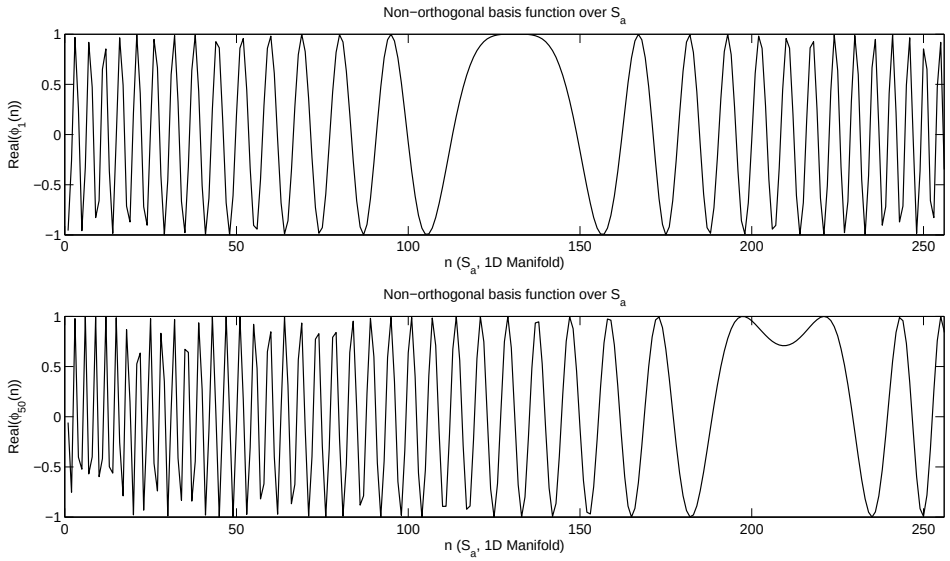

Figure 3.17: Real part of the propagating plane waves intersected by the 1D manifold S_a.

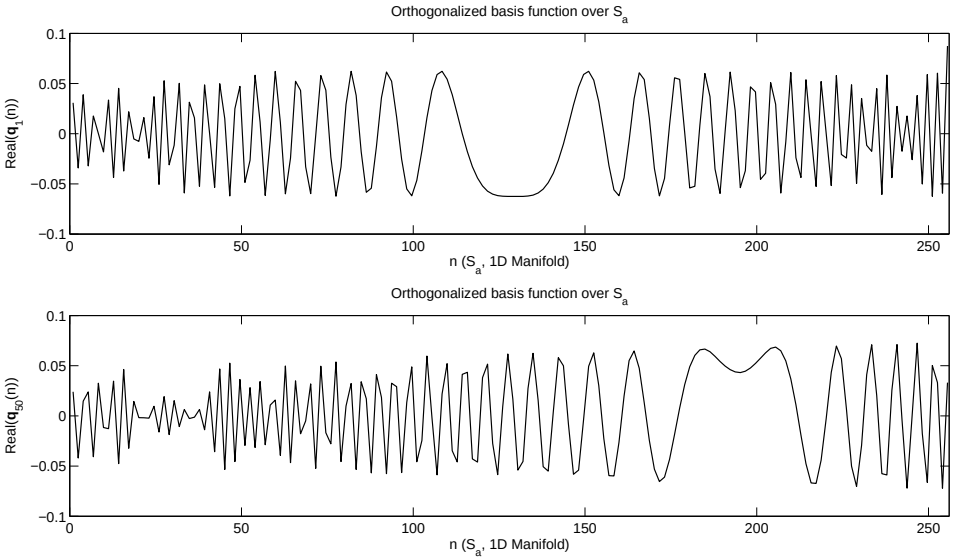

Figure 3.18: Real part of the orthogonalized functions along the manifold S_a.

The reconstructed coefficients of the plane waves by the proposed algorithm can be seen in Figure 3.19.

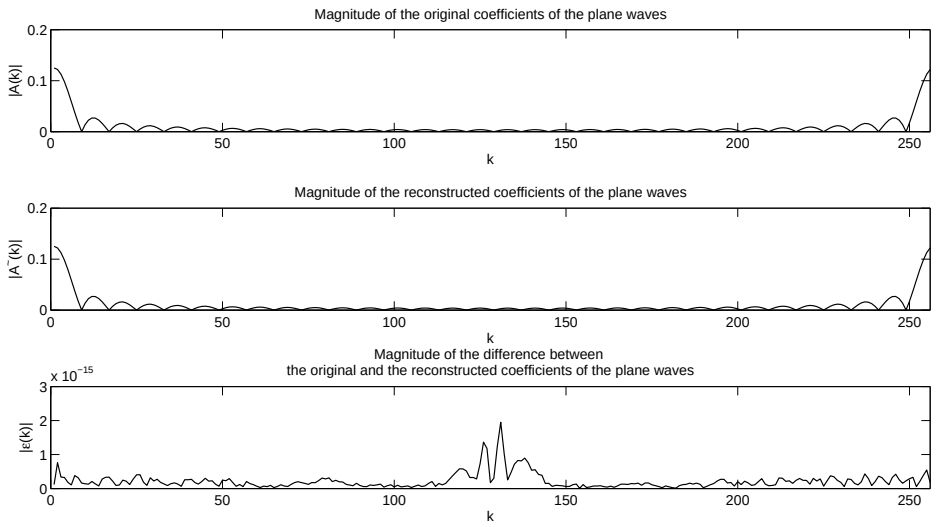

Figure 3.19: Magnitude of the coefficients that form the initial diffraction field over the space. Magnitude of the reconstructed coefficients. Magnitude of the difference between the initial and the reconstructed coefficients.

The diffraction field over the reference line, S_0, is reconstructed from the estimated coefficients and perfect reconstruction of the field is achieved. The magnitudes of the initial and the reconstructed diffraction fields with the magnitude of their difference can be seen from Figure 3.20. The reconstructed diffraction field on the manifold S_a is shown in Figure 3.21 and again perfect reconstruction is achieved.

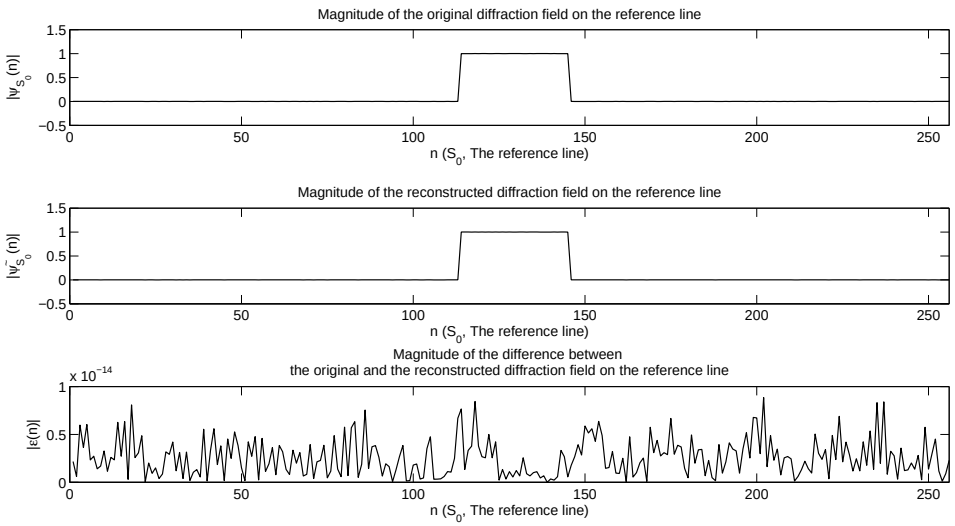

Figure 3.20: Original diffraction function on the manifold S_0. The reconstructed field on S_0 form the orthogonalized basis functions. The magnitude of the diffraction between the original and the reconstructed fields on S_0.

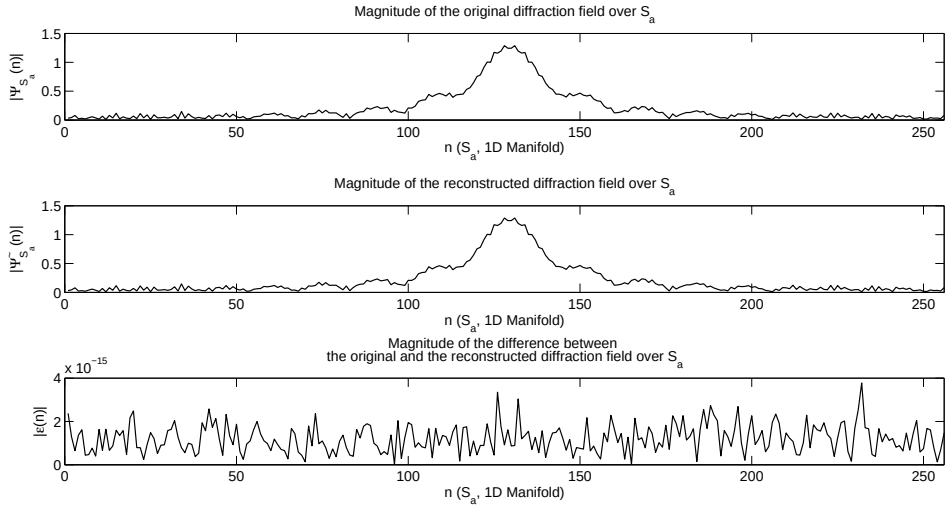

Figure 3.21: Original diffraction field on the manifold S_a. The reconstructed field on S_a form the orthogonalized basis functions. The magnitude of the difference between the original and the reconstructed fields on S_a.

As mentioned above, the presented computation method can be extended to find the diffraction field over the entire 3D space due to diffraction field given over a 2D manifolds. We again assume that the diffraction field over the 3D space is formed by propagating plane waves. Therefore, reconstruction of the complex amplitudes of the plane waves paves the way to compute the diffraction field over the entire space as in the 2D space scenarios. The diffraction field over the 2D manifold S_a can be expressed by the intersections of the plane waves by S_a. The same algorithm used in the 2D space scenarios can also be employed in 3D scenarios after converting each 2D field and coefficient arrays into 1D field and coefficient arrays. Furthermore, each signal, which is the intersection of a plane waves by S_a, is stored as a 2D array. For instance, the diffraction field over the manifold S_a is stored as a 2D array:

$$\boldsymbol{\psi}_{S_a} = \left[\begin{array}{c|c|c|c} \boldsymbol{\psi}_{S_a,1} & \boldsymbol{\psi}_{S_a,2} & \ldots & \boldsymbol{\psi}_{S_a,N} \end{array} \right] \tag{3.27}$$

where $\boldsymbol{\psi}_{S_a,i}$ is as a column vector which represents the variation of the 2D diffraction field given over the manifold S_a along y-axis and the index of the column vector is shown by i. Then, it is converted into a 1D array $\boldsymbol{\psi}_v$ as

$$\boldsymbol{\psi}_v = \left[\begin{array}{c} \boldsymbol{\psi}_{S_a,1} \\ \hline \boldsymbol{\psi}_{S_a,2} \\ \hline \vdots \\ \hline \boldsymbol{\psi}_{S_a,N} \end{array} \right]. \tag{3.28}$$

The signal set which is obtained from the intersections of each plane wave by S_a and computed as $\boldsymbol{\Phi}(i,j) = \exp(j\mathbf{k}_{i,j}^T\mathbf{x})$ where $\mathbf{k}_{i,j} = [k_{m_i}, k_{m_j}, \sqrt{k^2 - {k_{m_i}}^2 - {k_{m_j}}^2}]$; and i and j denote the indices of the discrete spatial frequencies along x and y axes, respectively. The 2D array representations of these signals are obtained as

$$\boldsymbol{\Phi}(i,j) = \left[\begin{array}{c|c|c|c} \boldsymbol{\phi}_{i,j,1} & \boldsymbol{\phi}_{i,j,2} & \ldots & \boldsymbol{\phi}_{i,j,N} \end{array} \right] \tag{3.29}$$

where $\boldsymbol{\phi}_{i,j,l}$ is a column vector as in Eq. 3.27. Then, 2D array is converted into 1D array as in Eq. 3.28,

$$\boldsymbol{\Phi}_v(i,j) = \left[\begin{array}{c} \boldsymbol{\phi}_{i,j,1} \\ \hline \boldsymbol{\phi}_{i,j,2} \\ \hline \vdots \\ \hline \boldsymbol{\phi}_{i,j,N} \end{array}\right]. \tag{3.30}$$

Then, the system matrix $\boldsymbol{\Phi}$ is formed by the 1D arrays $\boldsymbol{\Phi}_v(i,j)$ as

$$\boldsymbol{\Phi} = \Big[\boldsymbol{\Phi}_v(1,1)\big|\ldots\big|\,\boldsymbol{\Phi}_v(1,N)\big|\,\boldsymbol{\Phi}_v(2,1)\big|\ldots\big|\,\boldsymbol{\Phi}_v(2,N)\big|\ldots\big|\,\boldsymbol{\Phi}_v(N,1)\big|\ldots\big|\,\boldsymbol{\Phi}_v(N,N)\Big]. \tag{3.31}$$

To store these arrays, huge amount of memory is needed to be allocated. As a result of the limitations on the memory allocation, extending the presented algorithm to 3D space may not be feasible for the 3D scenarios representing practical cases.

Even though, the proposed extension from 2D to 3D brings memory problems, a simple example is implemented as a proof of concept. The reference plane has 32 samples along both transversal axes. A 32×32 synthetic signal, which has a unit magnitude 2D square pulse located at the center, is written on the reference plane. The width of the pulse is 8 samples along both transversal axes. The 2D manifold in the simulation can be seen in Figure 3.22.

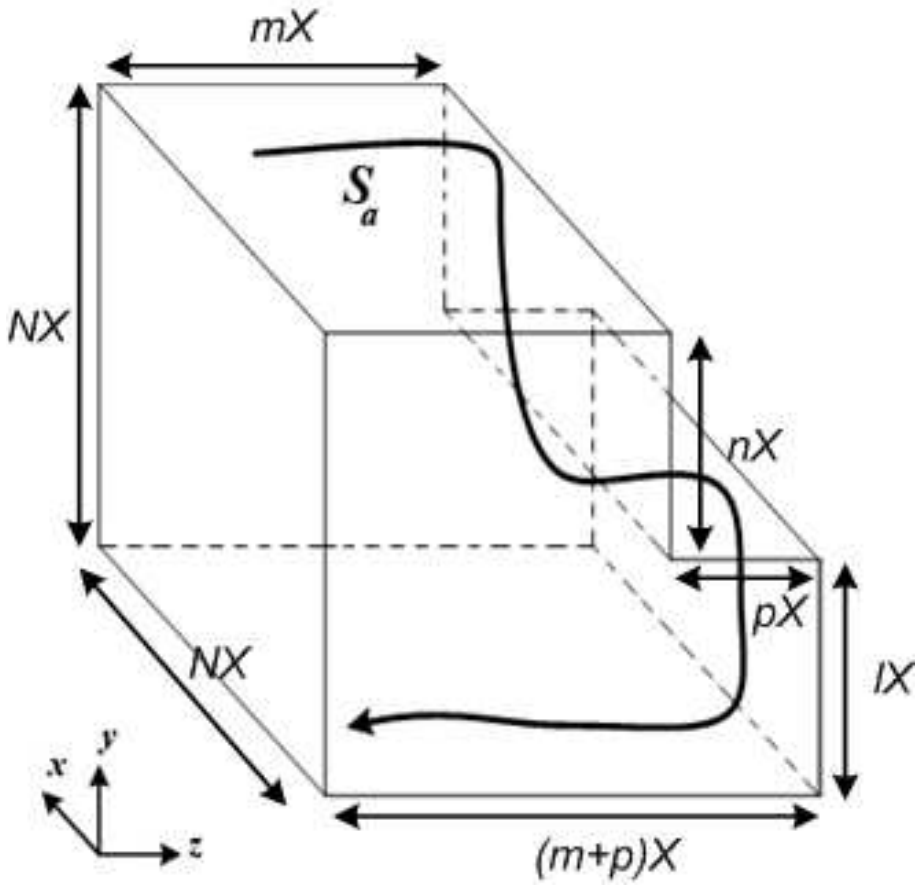

Figure 3.22: Implemented scenario related to 3D space.

The variables m, n, p and l are taken as 12, 16, 10 and 16, respectively; $N = 32$. The spatial sampling over the space is chosen as $\frac{\lambda}{2}$ and the optical wave length is chosen as $0.5\,\mu m$ as in the 2D space scenarios discussed earlier. An illustration of the chosen diffraction field over the reference plane can be seen in Figure 3.23(a). Then, the diffraction field over the entire 3D space due to the 2D square pulse is computed by using the plane wave decomposition. The diffraction over the 2D manifold S_a is shown in Figure 3.24. By using the proposed algorithm, the diffraction field over the reference plane is computed due to the given diffraction field over the 2D manifold S_a. The reconstructed field over the reference plane is shown in Figure 3.23.

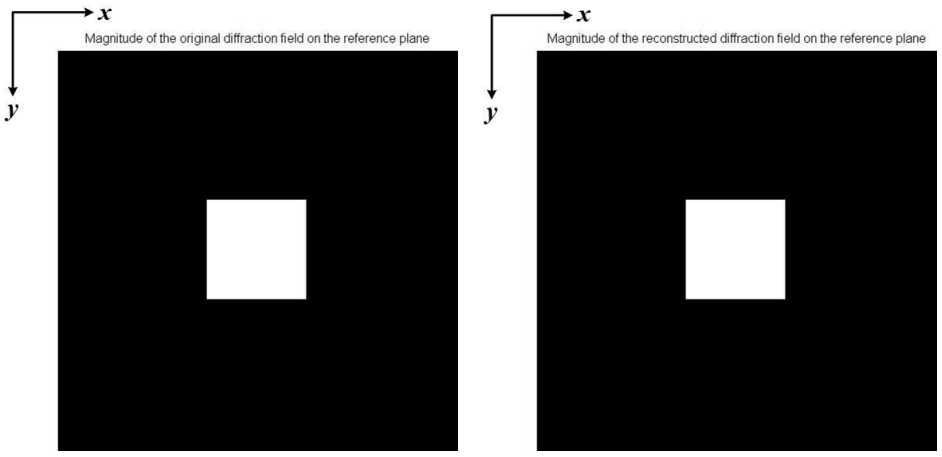

(a) (b)

Figure 3.23: (a) Magnitude of the synthetically generated diffraction field on the reference plane. This is a square pulse in 2D. Its width along both transversal axes is chosen as $8X$ where X is the spatial sampling period. (b) Magnitude of the reconstructed diffraction field over the reference plane from computed coefficients using the diffraction field over the manifold.

The diffraction field over the manifold S_a is computed from the the reconstructed field over the reference plane. Again perfect reconstruction is obtained. The reconstructed diffraction field over the 2D manifold S_a can seen in Figure 3.24.

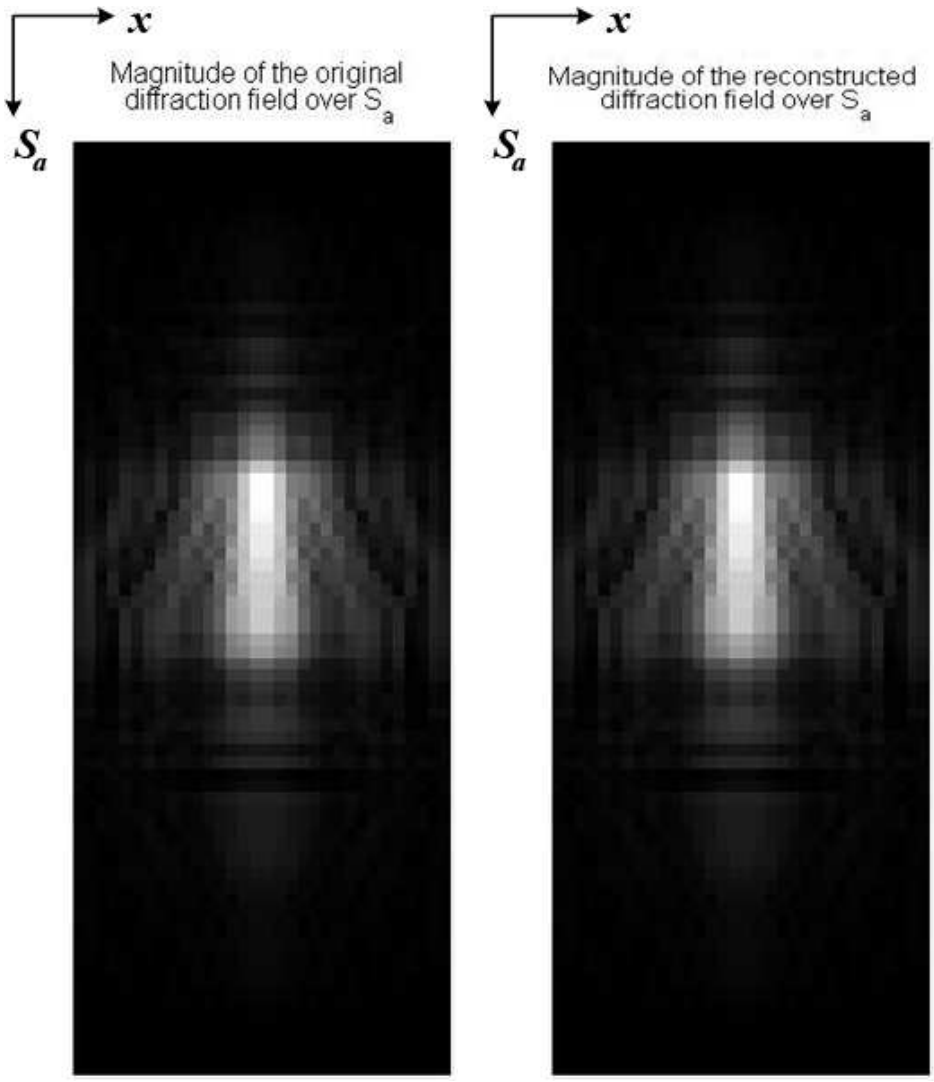

(a) (b)

Figure 3.24: (a) Magnitude of the synthetically generated diffraction field on the manifold S_a. (b) Magnitude of the reconstructed diffraction field on S_a from computed coefficients using the diffraction field over the manifold..

In this chapter, a diffraction field computation algorithm which is based on signal decomposition is presented. The proposed algorithm takes the diffraction field over an orientable manifold as an input and calculates the complex amplitudes of the propagating plane waves which form the diffraction field over the entire space. Decomposition of the diffraction field, defined over the manifold, onto the orthogonal signals, derived from the intersections of the propagating

plane waves by the manifold, provides to compute the complex amplitudes of the plane waves. Then, the exact diffraction field over the entire space can be calculated by superposing the propagating plane waves which are weighted by the computed complex amplitudes. The proposed algorithm can be used to compute exact diffraction field over the entire space for both 2D and 3D space scenarios but in 3D scenarios, large amount of memory allocation is needed.

In the following chapter, three more algorithms which can be used to compute exact diffraction field over the entire space are presented. Two of them are based on iterative solution and the other one is generated because of comparison purposes. Those algorithms also employ PWD in diffraction field calculations as in the presented algorithm in this chapter.

Chapter 4

Field Model Algorithms based on Iterative Methods

Computation of the diffraction field due to an object is a costly process [11, 12]. Thus several approximations on the object representation and the field computation methods are applied [15, 16, 19, 26]. Furthermore, device specific algorithms are generated to achieve faster computations [17, 18, 70, 77]. The diffraction field calculation algorithms presented in the references given above employ the source model approach which is mentioned in Chapter 2. Therefore, the diffraction field created by the object may not be calculated exactly using those algorithms, because the field values on the elementary building blocks of the objects are altered, compared to their original values, when the fields diffracted due to these blocks of the object are superposed. The mutual couplings between the fields emitted by the elementary building blocks are omitted in those algorithms during the superposition process; each diffraction field emitted by an elementary building block is taken into consideration as if it is the only light source in the space. Hence, the calculated diffraction field by using the source model can be different from the exact field over the entire space. As mentioned in Chapter 2, the diffraction field calculation methods like plane wave decomposition (PWD) and

Rayleigh-Sommerfeld (RS) diffraction integrals provide to compute diffraction fields due to a field given on a planar surface. In this chapter, three more field model algorithms are presented to calculate the exact diffraction field over entire space from the samples of the field on the object. Two of them are based on iterative methods and the third one is designed because of performance comparison purposes.

The description of an object in the space is the first issue that has to be considered in computation of the related diffraction field. To define an object, we choose to use continuous manifolds over the space. Manifolds can be used to denote the skin of the object. Besides, there are some object representations that may decrease the computational cost. Commonly used object representations are point clouds, planar patches and planar slices which are taken along the longitudinal axis. These approximations can be interpreted as different sampling procedures applied to the continuous 3D object. Furthermore, the properties of the chosen sampling procedures affect the representation of the object. For instance, when an object is represented by large triangular patches, then the details in the shape of the object can not be displayed. Similar effect can be seen when the object is sampled sparsely on the spatial domain. The object may also be represented by planar slices and each slice may be displayed sequentially. In the rest of the dissertation, point sampling procedure is chosen because the implementation of the proposed algorithms, based on pseudo inversion and conjugate gradient, become feasible.

The second issue on the computation of diffraction field due to an object is to determine the effects of approximations used during the field computation on the accuracy of the computed field and the computational complexity. One of the widely used approximations on the diffraction field computation is to take each sample point on the object surface as a point light source. Then, the superposition of the diffraction fields due to these point sources are taken as the diffraction

field due to the object. This kind of diffraction field calculation methods are called as the "source model" as briefly mentioned in Chapter 1. Another approximation on the field computation is the limit on the field to have only paraxial waves as in Fresnel approximation. Paraxial approximation is valid when the spatial frequencies of the propagating waves, k_x and k_y, are much smaller than the wave number, $k = \frac{2\pi}{\lambda}$, where λ is the optical wave length. Far-field approximation is also commonly employed. Fresnel and far-field approximations provide reasonable results for the regions where spherical wave can be approximated as paraboloidal and planar waves, respectively. However for the region that is closer to the source, those approximations are not valid. Fresnel and far-field approximations pave the way to develop more efficient algorithms, because the diffraction field integral kernels of the Fresnel and Fraunhofer approximations are separable, so computational complexity can be decreased substantially. However by using those approximations, there will be a deviation from correct diffraction field.

In this chapter, three diffraction field computation algorithms based on the "field model" approach, as opposed to the "source model", are presented. In the presented algorithms, we assume that the continuous diffraction field is sampled over a manifold. From the given field values on the samples, the continuous diffraction field over the entire space is computed. As a consequence of the simultaneous solution over the samples, the computed field over the entire space satisfies the wave equation and keeps the field values on the samples unaltered. The resultant continuous diffraction field over the space can be interpreted as the interpolation based on the wave propagation properties by taking the field values on the given samples as constraints.

4.1 Foundations of the proposed field model algorithms

The details of the computation of the scalar monochromatic optical diffraction field between two parallel planes are presented in Chapter 2. Several algorithms may be developed to compute diffraction field due to a given field over a surface. One such algorithm is mentioned in Chapter 3. In addition to the algorithm given in Chapter 3, three more algorithms are presented in this chapter as alternative methods to compute the exact diffraction field over the entire space due to a set of distributed field samples which are taken on a surface. In this chapter, two of the proposed algorithms are based on iterative methods and the third one is designed as a comparison tool. All three algorithms provide simultaneous solution of the diffraction field due to the given diffraction field.

Evanescent wave components of the diffraction fields are omitted in the proposed algorithms because we chose to deal only with propagating waves. Evanescent waves attenuate exponentially, hence they do not carry information after a few λ away from the object. Therefore, there is a frequency bandwidth restriction on the diffraction field that we are interested in. This effect can be seen from the field relationship between two parallel planes in the frequency domain,

$$A(k_x, k_y; z_0) = A(k_x, k_y; 0) \exp(jk_z z_0) \tag{4.1}$$

where $A(k_x, k_y; 0)$ and $A(k_x, k_y; z_0)$ denote the frequency response of the diffraction field over $z = 0$ and $z = z_0$ planes, respectively. The exponential term $\exp(jk_z z_0)$, which represents the phase shift due to translation of the observation plane along the z-axis, can also be interpreted as the Fourier transform of the free space impulse function. As mentioned in the Chapter 2, we deal with monochromatic diffraction fields, hence k_z is a function of k_x and k_y as

$$k_z = \sqrt{k^2 - {k_x}^2 - {k_y}^2} \tag{4.2}$$

where $k = \frac{2\pi}{\lambda}$ *radians / unit length*. For the evanescent waves, k_z is imaginary thus the exponential term $\exp(jk_z z_0)$ becomes pure real and rapidly decreases with increasing z_0. The limits of the frequency band is obtained from dealing with monochromatic propagating waves: k_x and k_y are restricted to be in a circle whose radius is less than or equal to $\frac{2\pi}{\lambda}$ *radians / unit length*.

Plane wave decomposition (PWD) can be used to calculate the scalar optical disturbances exactly (without any approximation) due to a given field over a planar surface. When the evanescent waves are excluded from the calculation of the diffraction field, Rayleigh-Sommerfeld diffraction integral and PWD become equivalent [52, 53]. The proof of this argument can also be seen in Chapter 2. The proposed algorithms in this chapter employ PWD in the calculation of scalar diffraction fields.

The algorithms presented in this chapter are developed for both 2D and 3D space scenarios. The 2D space model can be obtained from the 3D space formulation. Thus, the PWD of a 1D diffraction field over 2D space has to be found from the expressions for 2D field over 3D space by setting no variation along one of the transversal direction. The diffraction field over the entire 3D space due to the field given over $z = 0$ can be expressed as

$$\begin{aligned} \psi(x,y,z) &= \mathcal{F}_{2D}^{-1}\Big\{\mathcal{F}_{2D}\big\{\psi(x,y,0)\big\}\exp[j(k^2 - {k_x}^2 - {k_y}^2)^{\frac{1}{2}}z]\Big\} \\ &= \mathcal{F}_{2D}^{-1}\Big\{\Psi(k_x,k_y,\sqrt{k^2 - {k_x}^2 - {k_y}^2})\exp[j(k^2 - {k_x}^2 - {k_y}^2)^{\frac{1}{2}}z]\Big\} \quad (4.3) \end{aligned}$$

where the operator $\mathcal{F}_{2D}$ is Fourier transform over the (x,y)-plane. To find the 2D space model, we assume that the diffraction field $\psi(x,y,0)$ has no variation along y-axis. Therefore, the Fourier transform of the field $\psi(x,y,0)$ can be expressed as $(2\pi)\Psi(k_x,k_y,\sqrt{k^2 - {k_x}^2 - {k_y}^2})\delta(k_y)$. Then, Eq. 4.3 can be written as

$$\psi(x,y,z) = (2\pi)\mathcal{F}_{2D}^{-1}\Big\{\Psi(k_x,0,\sqrt{k^2 - {k_x}^2})\delta(k_y)\exp[j(k^2 - {k_x}^2)^{\frac{1}{2}}z]\Big\}. \quad (4.4)$$

After substituting the expression

$$\begin{aligned}\psi_{2D}(x,0) &\triangleq (2\pi)\mathcal{F}_{2D}^{-1}\big\{\Psi(k_x,0,\sqrt{k^2-{k_x}^2})\delta(k_y)\big\}\\ &\triangleq \mathcal{F}_{1D}^{-1}\big\{\Psi_{1D}(k_x,\sqrt{k^2-{k_x}^2})\big\}\end{aligned} \tag{4.5}$$

into Eq. 4.4, the diffraction field relation in 2D space can be found as

$$\psi_{2D}(x,z)=\mathcal{F}_{1D}^{-1}\Big\{\mathcal{F}_{1D}\big\{\psi_{2D}(x,0)\big\}\exp[j({k^2-{k_x}^2})^{\frac{1}{2}}z]\Big\} \tag{4.6}$$

where the operator $\mathcal{F}_{1D}$ denotes Fourier transform along only x-axis. The diffraction field $\psi_{2D}(x,z)$ represents the field over the 2D space, and $\frac{1}{2\pi}\mathcal{F}_{1D}\big[\psi_{2D}(x,0)\big]$ represents the complex coefficients of the plane waves.

The discretization procedure of the 1D diffraction field is the same as in 2D diffraction field. The details of the sampling procedure can be found in Chapter 2. The obtained form of the discrete representation of the PWD in 1D is [1, 64–66, 68]

$$\psi_D(n_x,p)=\sum_{m_x=0}^{N-1}A_{1D}(m_x)H_p(m_x)\exp\left(j\frac{2\pi}{N}n_xm_x\right), \tag{4.7}$$

where $N\cdot A_{1D}(m_x)$ is the DFT of the sampled input field and the variable n is defined within the range $[0,N)$. Sampling the field both in spatial and frequency domains cause to have periodic patterns in both spatial and frequency domains. One period of the fields are displayed in the implemented algorithms. The discrete diffraction field can be expressed in a compact form as [1, 65]

$$\psi_D(n_x,p)=DFT^{-1}\Big\{DFT\{\psi_D(n_x,0)\}H_p(m_x)\Big\}. \tag{4.8}$$

The variable m_x determines the propagation direction of the corresponding plane wave as [1, 65]

$$\mathbf{k}=\begin{cases}\left[\frac{2\pi}{NX_s}m_x \quad \frac{2\pi}{NX_s}\sqrt{\beta^2-{m_x}^2}\right]^T & ,m_x\in[0,\frac{N}{2}-1]\\ \left[\frac{2\pi}{NX_s}(m_x-N) \quad \frac{2\pi}{NX_s}\sqrt{\beta^2-(m_x-N)^2}\right]^T & ,m_x\in[\frac{N}{2},N-1]\end{cases} \tag{4.9}$$

where $\beta=\frac{NX_s}{\lambda}$ and λ denotes the optical wave length. An illustration of propagating plane waves in 2D space is given in Figure 4.1.

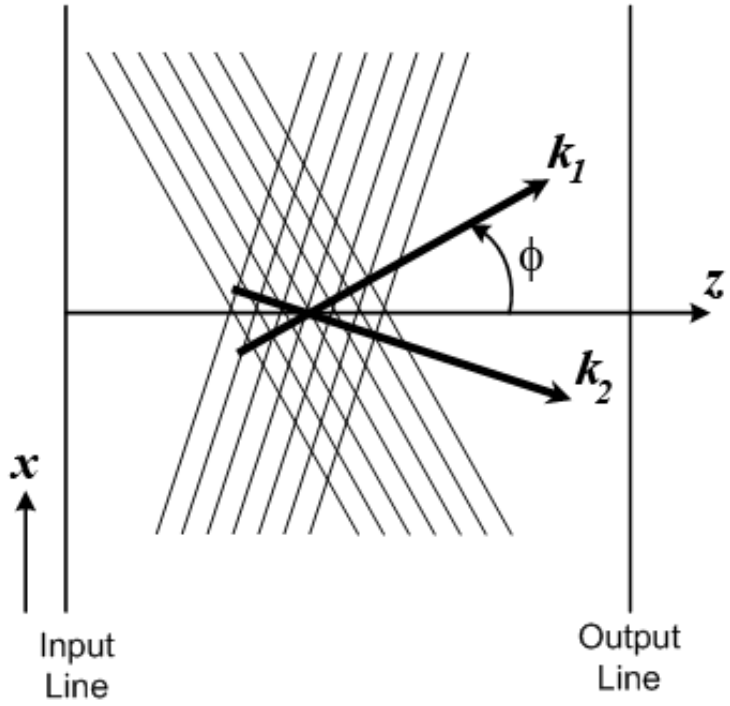

Figure 4.1: The vectors $\mathbf{k}_1$ and $\mathbf{k}_2$ are the wave vectors of the plane waves.

The diffraction field relation between the distributed data set over the space and a given line can not be represented as a shift-invariant system, because the free space impulse function varies with z. Despite that, calculation of the diffraction field on a region over a surface due to a given diffraction field defined over a transversal planar surface is relatively straightforward, because in this case there is no mutual coupling, hence superposition over the given field samples is a valid operation. However, inverse of the mentioned case is not straightforward. In general, the diffraction field samples can be given over a curved surface or a tilted plane or another shape in space. Then, the field over the defined shape is sampled and these samples can be taken into consideration as a set of distributed known data points over the space. A 1D illustration of such a scenario is given in Figure 4.2.

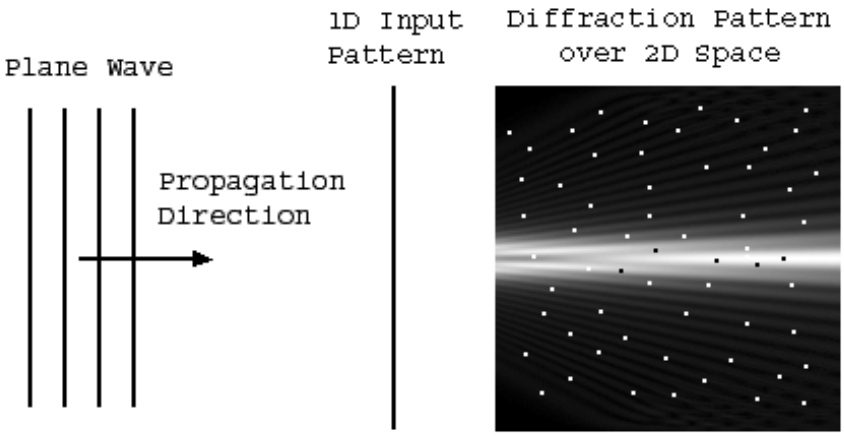

Figure 4.2: An illustration of 1D object illumination and the diffraction pattern of the object over 2D space. Dots on the corresponding diffraction pattern represent the locations of a set of distributed known data points over 2D space.(©2007 Elsevier. Reprinted with permission. Published in [1])

Even if there are several algorithms in the literature that can be used to compute the diffraction field between parallel and tilted lines [33, 34, 60, 62, 78–80]. However, those algorithms can not provide calculation of the exact diffraction field due to the field samples which are taken over a curved surface. In this chapter, only the samples are known and these field samples are taken into consideration as a set of arbitrarily distributed data points. A simple and naive approach employed in computation of the diffraction field due to a set of distributed data points is superposition of the diffraction fields created by these sample points, but it would yield erroneous results. Two simple 1D examples, which are also presented in [1], clarify this fact.

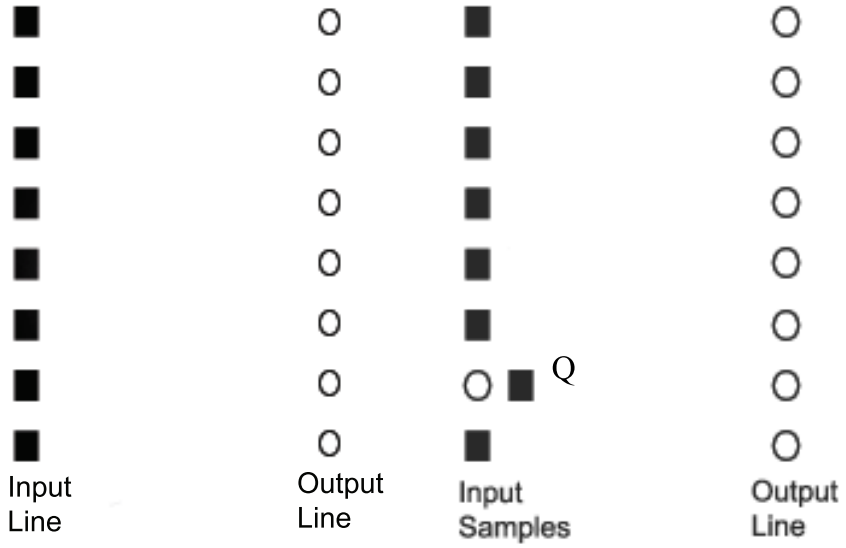

Figure 4.3: (a) Parallel input and output lines (b) Example involving a single displaced known data point (©2007 Elsevier. Reprinted with permission. Published in [1])

In Figure 4.3, the black squares represent given samples while the white circles represent the missing ones. In the first example, the input and output lines are parallel to each other with no missing data points (Figure 4.3(a)). The relationship between the fields on these lines can be represented as a linear shift-invariant system, given by Eq. 4.8. In the second example (Figure 4.3(b)), the field at one of the sample points on the input line is not known. Instead, the field at another sample point Q, not located on the input line, is given in order to compensate the missing data. Each point on the input line contributes to the field at Q, and in turn, the field at Q affects the field at the other points over the input line. Therefore, superposition of the diffraction fields due to isolated samples is not a proper method to calculate the field at unknown regions.

The algorithms presented in this chapter provides simultaneous calculation of the field, therefore all the possible mutual couplings between the given sample points are taken into consideration. The sample points which are taken over the

surface is considered as inputs, then the field over the entire space is computed from this input. All three proposed algorithms utilize the plane wave decomposition for the diffraction field computation.

The first algorithm can be used to compute the diffraction field over a reference line, which is a hypothetical transversal line, from the given samples which are not located over a line. The algorithm uses the pseudo inversion of the system matrix. The system matrix defines the diffraction field relation between the given samples (not on a line) and the unknown field over the reference line [1].

In the second algorithm, it is shown that the diffraction field samples taken over a surface form convex sets and a projection operation can be defined by using the propagation between two parallel planes. As a result of this, performing the defined projection operation iteratively, the exact diffraction field over the entire space can be calculated [1].

The last algorithm is again an iterative method. In this method first, the complex amplitudes of the plane waves forming the diffraction field over the space are computed. Then, by using the plane waves and their complex amplitudes, the field over the entire space is computed. The complex amplitudes are obtained by taking the inverse of the system matrix. In this algorithm, inversion operation is performed by the conjugate gradient search method [64].

All the proposed algorithms in this chapter are based on the relation given by Eq. 4.3 and Eq. 4.8. For simplicity, we use the expression in Eq. 4.8 which is for 2D space scenarios, but extension to 3D space is straightforward and can be found in the following sections. We can rewrite the relation in Eq. 4.8 in matrix vector multiplication [1]

$$\mathbf{g} = \mathbf{A}\mathbf{f}, \tag{4.10}$$

where the vectors $\mathbf{f}$ and $\mathbf{g}$ represent the discrete diffraction fields $\psi_D(n_x, 0)$ and $\psi_D(n_x, p)$ of the reference line and some other line, respectively. The rows of $\mathbf{A}$

are obtained from Eq. 4.8 as [1]

$$\mathbf{A} = \mathbf{W}^{-1}\mathbf{H}_p\mathbf{W}, \tag{4.11}$$

where the matrix $\mathbf{W}$ is the N-point DFT matrix. The matrix $\mathbf{H}_p$ is the diagonal matrix

$$\mathbf{H}_p = \begin{bmatrix} H_p(0) & 0 & \dots & 0 \\ 0 & H_p(1) & & 0 \\ \vdots & & \ddots & \vdots \\ 0 & 0 & \dots & H_p(N-1) \end{bmatrix}. \tag{4.12}$$

The matrix $\mathbf{A}$ is unitary. Furthermore, $\mathbf{A}^k$ represents the diffraction field at a distance pk. Proofs of these properties are given in the Appendix B for the sake of the completeness of the discussion.

4.2 Pseudo-Inversion of System Matrix

The presented algorithm in this section is first published in [1]. The proposed algorithm is based on a straightforward solution by employing linear algebra tools. Also, this approach provides the lowest error among the other proposed algorithms in this chapter. The algorithm presented in this section is used for performance comparison purposes by the other algorithms presented in the following sections.

First, the 2D space model for the algorithm will be presented, then the extension of the algorithm to 3D space will be given. To illustrate and evaluate the performance of the algorithm for arbitrary settings, the samples are taken from randomly distributed locations over the 2D space. Then, the system matrix is formed by the diffraction field relation between the field on the given samples and the reference line. The degree of the freedom of the problem is stated by the number of plane waves forming the diffraction field over the entire space. Not to deal with an under-determined system, the number of randomly located

input samples are kept equal or more than the number of plane waves forming the diffraction field over the entire space. In this approach, the diffraction field on a hypothetical transversal line, which we call it reference line, is calculated by directly solving the linear equations stated by system matrix, $\mathbf{A}_{BF}$.

The given samples of the field are represented by the vector $\mathbf{g}'$ [1],

$$\mathbf{g}' = \begin{bmatrix} g'_1 \\ g'_2 \\ \vdots \\ g'_s \end{bmatrix} \tag{4.13}$$

where s denotes the number of given samples. Each g'_i is a function of both p_i, the distance along the z axis, and $n_{x,i}$, the location along the x axis. The relation between the vector $\mathbf{g}'$ and the vector $\mathbf{f}$ is given by [1]

$$\mathbf{g}' = \mathbf{A_{BF}}\mathbf{f}, \tag{4.14}$$

where $\mathbf{f}$ is the diffraction field along the reference line and the system matrix $\mathbf{A_{BF}}$ is shown as [1]

$$\mathbf{A_{BF}} = \begin{bmatrix} \mathbf{r}(p_1, n_{x,1}) \\ \mathbf{r}(p_2, n_{x,2}) \\ \vdots \\ \mathbf{r}(p_s, n_{x,s}) \end{bmatrix}, \tag{4.15}$$

where $\mathbf{r}(p_i, n_{x,i})$ is a 1 by N row vector from the matrix $\mathbf{A}$ with $p = p_i$. This row vector denotes the diffraction field relation between the field on the reference line and the field on the point whose location is specified by p_i and $n_{x,i}$. The vector $\mathbf{f}$ is calculated as [1]

$$\mathbf{f} = \mathbf{A}^{\dagger}_{\mathbf{BF}}\mathbf{g}', \tag{4.16}$$

where $\mathbf{A}^{\dagger}_{\mathbf{BF}}$ is the pseudo inversion of the system matrix $\mathbf{A_{BF}}$ [1]:

$$\mathbf{A_{BF}}^{\dagger} = \begin{cases} (\mathbf{A_{BF}}^H \mathbf{A_{BF}})^{-1} \mathbf{A_{BF}}^H, s > N \\ \mathbf{A_{BF}}^H (\mathbf{A_{BF}}^H \mathbf{A_{BF}})^{-1}, s < N \end{cases}. \tag{4.17}$$

Here $\mathbf{A_{BF}}^H$ is the conjugate transpose of $\mathbf{A_{BF}}$. Pseudo-inversion of a matrix provides to have least-mean square solution [81]. The diffraction field over the entire space can be computed by using Eq. 4.8 from the diffraction field reconstructed on the reference line.

The proposed algorithm based on the pseudo inversion of the system matrix can also be used to compute the diffraction fields over the 3D space. In the 3D space scenarios, the diffraction field over a hypothetical transversal plane, which is taken as a reference plane, is computed from the arbitrarily located given samples over the space, as in the 2D space scenarios. The field over the reference plane is stored in a 2D array. The system matrix again denotes the diffraction field relationship between the field on the reference plane and the field on the given samples. The problem of computing the diffraction field over the reference plane due to the field samples over the 3D space can be taken into consideration as in the case of 2D space scenarios. Therefore, the diffraction field over the reference plane is transformed into a vectorial representation and the system matrix is converted to a two dimensional array. The pseudo inversion of the system matrix will be obtained as given by Eq. 4.17. Then, the field over the reference plane is calculated as shown by Eq. 4.16.

Therefore, the discrete diffraction field over the reference plane is

$$\psi(n_x, n_y, 0) = \boldsymbol{\psi}_{2D} = \Big[\boldsymbol{\varphi}_1 | \boldsymbol{\varphi}_2 | \ldots | \boldsymbol{\varphi}_N\Big] \tag{4.18}$$

where $\boldsymbol{\varphi}_i$ is a N by 1 column vector. Conversion of the 2D diffraction field over the reference plane is obtained as,

$$\boldsymbol{\psi}_{1D} = \left[\begin{array}{c} \boldsymbol{\varphi}_1 \\ \hline \boldsymbol{\varphi}_2 \\ \hline \vdots \\ \hline \boldsymbol{\varphi}_N \end{array}\right]. \tag{4.19}$$

The conversion of the system matrix is obtained by using a similar technique as mentioned above. The system matrix in the 3D space is constructed by the 2D matrices $\mathbf{h}_i$. The matrix $\mathbf{h}_i$ represents the RS diffraction field kernel for i^{th} sample point and it is computed as

$$\begin{aligned} \mathbf{h}_i &= DFT^{-1}\{DFT[\delta(n_x - n_{x,i}, n_y - n_{y,i})]H_{p_i}(m_x, m_y)\} \\ &= \left[\, \mathbf{h}_{i,1} \middle| \, \mathbf{h}_{i,2} \middle| \, \ldots \middle| \, \mathbf{h}_{i,N} \,\right] \end{aligned} \tag{4.20}$$

where $H_{p_i}(m_x, m_y)$ is defined in Eq. 2.23 and the position of the given sample point is expressed by $n_{x,i}$, $n_{y,i}$ and p_i in the 3D space. The RS diffraction kernel, $\mathbf{h}_i$, is shifted along x and y axes by amount of $n_{x,i}$ and $n_{y,i}$, respectively. The function $\delta(n_x, n_y)$ and the constant N^2 forms a 2D DFT pair. The kernel $\mathbf{h}_i$ defined in Eq. 4.20 is formed by N by 1 column vectors, $\mathbf{h}_{i,j}$ where i denotes the index of the given samples and j indicates the index of column vectors which form the matrix $\mathbf{h}_i$. The conversion of the kernel from 2D to 1D is needed and the conversion of the system matrix is obtained as

$$\mathbf{A}_{BF,2D} = \left[\begin{array}{c|c|c|c} \mathbf{h}_{1,1}^T & \mathbf{h}_{1,2}^T & \ldots & \mathbf{h}_{1,N}^T \\ \hline \mathbf{h}_{2,1}^T & \mathbf{h}_{2,2}^T & \ldots & \mathbf{h}_{2,N}^T \\ \hline & \vdots & & \\ \hline \mathbf{h}_{s,1}^T & \mathbf{h}_{s,2}^T & \ldots & \mathbf{h}_{s,N}^T \end{array}\right]. \tag{4.21}$$

Each row of the matrix $\mathbf{A}_{BF,2D}$ represents diffraction field relationship between the field on the reference plane and the field at a sample point. By concatenation of the row vectors $\mathbf{h}_{i,j}^T$, we form each row vector of the matrix $\mathbf{A}_{BF,2D}$.

Then, the field over the reference plane is computed as

$$\boldsymbol{\psi}_{2D} = \mathbf{A}_{BF,2D}^{\dagger}\mathbf{g}' \tag{4.22}$$

where $\mathbf{g}'$ is a column vector whose length is s and it represents the given samples of the diffraction field over the 3D space.

4.3 Projection onto convex sets

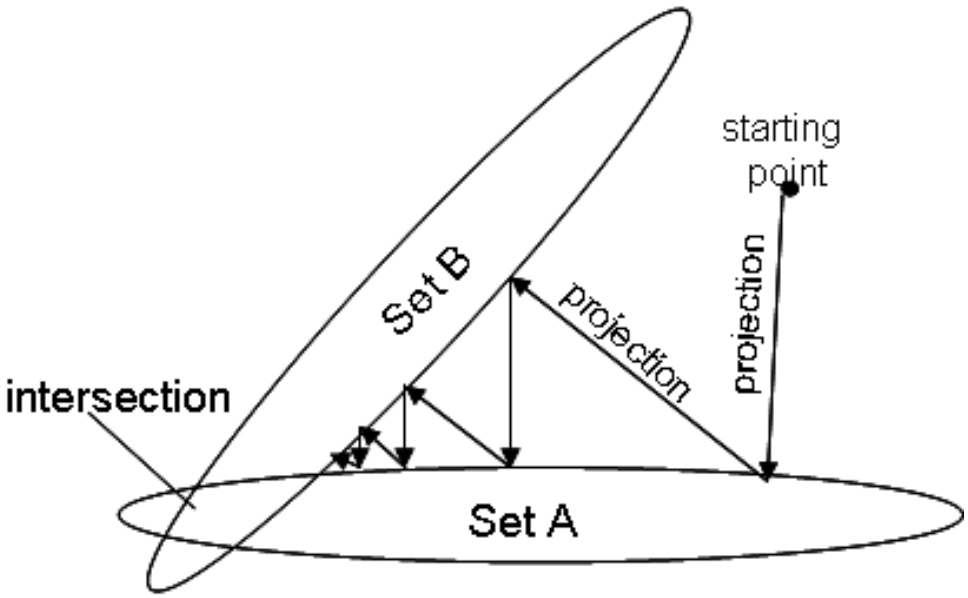

Figure 4.4: Projections Onto Convex Sets (POCS) (©2007 Elsevier. Reprinted with permission. Published in [1])

The second algorithm is also first published in [1]. The presented algorithm in this section is based on the projection onto convex sets (POCS) algorithm which is an iterative method [82, 83]. POCS is a versatile signal processing tool that it has been applied to various problems in holography and image restoration related problems [84–86]. In POCS algorithm, a priori information is used to constrain the size of the feasible solution set [84–88]. Then, starting with an arbitrary infeasible point, a number of convex constraints are applied iteratively to find a solution in a feasible region which is defined by the intersection of convex solution sets [82,83]. Iterative projections onto the convex sets provide convergence to the intersection of the convex sets. An illustration, which summarizes the procedure, is given in Figure 4.4. To satisfy the completeness of the document, the proof of the problem which shows that it can be set as a POCS problem is given in Appendix C.

Diffraction field on the missing points are set to arbitrary values on the first line $z = 0$. Then, the diffraction field on the second line is computed from the field on the first line. After then, the field values at the location of given samples are set to the given field values. Then, the same process is performed for the next line. The goal is to compute the diffraction field over the entire space by repeating the mentioned process. After passing through all lines, the unknown points on the first line are computed by using the data on the last line.

The algorithm can be summarized as follows [1]:

1. Initialize the field values on the first line $f(x_{i_l}, 0) = \mathbf{v}_0, f(x_{\bar{i}_l}, 0) = q(x_{\bar{i}_l}),$ for any $q(x)$
2. for $i = 1$ to n_{it}
   (a) for $l = 2$ to M
      i. $f(x, z_l) = \mathbf{A} f(x, z_{l-1})$
      ii. $f(x_{\mathbf{i}_l}, z_l) = \mathbf{v}_l$
   (b) end
   (c) $f(x, 0) = \mathbf{A}^{-M+1} f(x, z_M)$
   (d) $f(x_{\mathbf{i}_l}, 0) = \mathbf{v}_0$;
3. end

where n_{it} is the number of iteration.

The proposed POCS based algorithm for 3D space scenarios is first presented in [67]. The same iterative method also provides perfect reconstruction in 3D space scenarios when the number of given independent samples are equal or larger than the number of plane waves forming the diffraction field over the entire space. In 3D scenarios, instead of computing the diffraction field from

one transversal line to another, we compute diffraction field from one transversal plane to another.

The pseudo code of the algorithm for 3D scenarios is [1]

1. Initialize the field values over first plane $f(n_{i_1}, m_{i_1}, 1) = \mathbf{v}_1, f(n_{\bar{i}_1}, m_{\bar{i}_1}, 1) = q(n_{\bar{i}_1}, m_{\bar{i}_1}),$ for any $q(n, m)$
2. for $i = 1$ to n_{it}
   (a) for $l = 2$ to M
      i. $f(n, m, p_l) =$
      $DFT_{2D}^{-1}\{DFT_{2D}\{f(n, m, p_{l-1})\}H_1(n_f, m_f)\}$
      ii. $f(n_{\mathbf{i}_l}, m_{\mathbf{i}_l}, p_l) = \mathbf{v}_l$
   (b) end
   (c) $f(n, m, 1) =$
   $DFT_{2D}^{-1}\{DFT_{2D}\{f(n, m, p_M)\}H_{-M+1}(n_f, m_f)\}$
   (d) $f(n_{\mathbf{i}_1}, m_{\mathbf{i}_1}, 1) = \mathbf{v}_1$;
3. End

where $\mathbf{v}_l$ is the vector of the known samples on the plane $z = p_l X_s$, and i_l and $\bar{i}_l$ are the vector of indices of the known (given) and the unknown (desired) values on the plane $z = p_l X_s$, respectively. $q(n, m)$ is an arbitrary function whose samples are initially used in place of the unknown samples and n_{it} is the total number of iterations.

4.4 Conjugate Gradient

The algorithms mentioned above first focus on reconstruction of the diffraction field on a specific location (line for 2D and plane for 3D) and then compute the

field over the entire space due to the reconstructed field on that specific location. In this algorithm, we compute the coefficients of the plane waves that form the field over entire space. The presented algorithm is based on the conjugate gradient (CG) method. As in the above mentioned algorithms, it can also be used for both 2D and 3D scenarios. 2D and 3D space algorithms are first published [64] and [67], respectively. As in the previous sections, we first present the algorithm for a 2D setup; the extension to 3D setup is given afterwards. The plane wave decomposition is again used to describe the relationship between the diffraction field and the complex coefficients of the plane waves as,

$$\psi_{2D}(x_i, z_i) = \sum_{m_x=-\frac{N}{2}}^{\frac{N}{2}-1} A_{1D}(m_x) \exp\left(j\frac{2\pi}{NX} m_x x_i\right) \exp\left[j\frac{2\pi}{NX}(\beta^2 - {m_x}^2)^{\frac{1}{2}} z_i\right] \quad (4.23)$$

where $\psi_{2D}(x_i, z_i)$ are the given diffraction field samples arbitrarily located at (x_i, z_i) over the space, $i = 1, 2, \ldots, s$. The complex coefficients of the plane waves represented by $A_{1D}(m_x)$ and there are N plane waves that form the diffraction field. The spatial sampling is X and NX is the period along the transversal axis which is chosen as the x-axis.

The linear system given in Eq. 4.23 can be expressed in a matrix form,

$$\boldsymbol{\psi} = \mathbf{R}\mathbf{a} \quad (4.24)$$

where $\mathbf{a} = [A_{1D}(\frac{-M}{2}), A_{1D}(\frac{-M}{2}+1), \ldots, A_{1D}(\frac{M}{2}-1)]^T$ are the unknown complex coefficients of the plane waves and the vector $\boldsymbol{\psi} = [\psi_{2D}(x_1, z_1), \psi_{2D}(x_2, z_2), \ldots, \psi_{2D}(x_s, z_s)]^T$ denotes the given field samples. The matrix $\mathbf{R}$, which is s by N, denotes the system matrix,

$$\mathbf{R} = \left\{r_{p,q}\right\} \quad (4.25)$$

where the matrix element $r_{p,q}$ is found as [64],

$$r_{p,q} = \exp\left(j\frac{2\pi}{NX} m x_p\right) \exp\left[j\frac{2\pi}{NX}(\beta^2 - (q - \frac{M}{2} + 1)^2)^{\frac{1}{2}} z_p\right]. \quad (4.26)$$

The inner product of the i-th row of $\mathbf{R}$ with $\mathbf{a}$ is equal to the diffraction field at the point (x_i, z_i).

As in the first algorithm in this chapter, pseudo inverse of $\mathbf{R}$ will give the least-square solution for Eq. 4.24,

$$\mathbf{a} = \mathbf{R}^{\dagger}\mathbf{u}. \tag{4.27}$$

The way to compute the pseudo inverse of the matrix $\mathbf{R}^{\dagger}$ depends on the number of given samples. When $s \geq N$ then the system in Eq 4.24 is over-determined and pseudo-inverse of $\mathbf{R}$ has the form [64],

$$\mathbf{R}^{\dagger} = (\mathbf{R}^{H}\mathbf{R})^{-1}\mathbf{R}^{H} \tag{4.28}$$

where $\mathbf{R}^{H}$ is the conjugate transpose of $\mathbf{R}$. But, when $s < N$ the system in Eq. 4.24 is under-determined. Then, the pseudo-inverse of $\mathbf{R}$ is

$$\mathbf{R}^{\dagger} = \mathbf{R}^{H}(\mathbf{R}^{H}\mathbf{R})^{-1}. \tag{4.29}$$

In this case there are many solutions. We may not reconstruct the initial field, because the amount of given information is not sufficient.

The computational complexity associated with the computation of having the pseudo inverse of $\mathbf{R}$ is high. The same bottleneck is encountered in the first algorithm. Therefore, a numerically fast and stable algorithm is needed to find the least square solution for

$$\hat{\mathbf{a}} = \underset{\mathbf{a}\in\mathcal{R}_{\mathcal{M}}}{\arg\min} \|\boldsymbol{\psi} - \mathbf{R}\mathbf{a}\|. \tag{4.30}$$

In the literature, there is a myriad of iterative algorithms for solving the least square problems [81, 89]. In these algorithms, the problem is to deal with the slow convergence when the system matrix has a large condition number. To overcome the problem, symmetric matrices are generated. We can obtain symmetric matrices for both over-determined and under-determined cases as $\mathbf{Q}' = \mathbf{R}^{H}\mathbf{R}$ and $\mathbf{Q}'' = \mathbf{R}\mathbf{R}^{H}$, respectively. Symmetric matrices allows taking advantage of the conjugate gradient (CG) method to invert them in a fast and robust way. CG provides convergence in at most n iterations for n-dimensional problems [81].

The dimensionality of the of the problem becomes $n = M$ when the problem is the over-determined case; $n = s$ for under-determined cases.

The formulation of the over-determined scenarios is obtained by multiplying both sides of Eq. 4.24 with $\mathbf{R}^H$ to get [64]

$$\mathbf{R}^H\mathbf{R}\mathbf{a} = \mathbf{R}^H\boldsymbol{\psi}. \tag{4.31}$$

After, having necessary changes of variables as,

$$\mathbf{Q} = \mathbf{Q}' = \mathbf{R}^H\mathbf{R}, \quad \mathbf{x} = \mathbf{a} \quad \textit{and} \quad \mathbf{b} = \mathbf{R}^H\boldsymbol{\psi} \tag{4.32}$$

we obtain $\mathbf{Q}\mathbf{x} = \mathbf{b}$.

In the under-determined cases, the expression given in Eq. 4.24 can be rewritten as [64]

$$\mathbf{R}\mathbf{R}^H\mathbf{v} = \boldsymbol{\psi} \tag{4.33}$$

where $\mathbf{v}$ denotes the complex coefficients of the plane waves. The relation between the vector $\mathbf{a}$ and $\mathbf{v}$ is $\mathbf{a} = \mathbf{R}^H\mathbf{v}$. The similar form for the under-determined case can be achieved as in over-determined case by the substitutions,

$$\mathbf{Q} = \mathbf{Q}'' = \mathbf{R}\mathbf{R}^H, \quad \mathbf{x} = \mathbf{v} \quad \textit{and} \quad \mathbf{b} = \boldsymbol{\psi}, \tag{4.34}$$

and then we get $\mathbf{Q}\mathbf{x} = \mathbf{b}$. Please note that, for the under-determined case, the complex coefficients can be calculated after multiplying $\mathbf{x}$ by $\mathbf{R}^H$.

The CG algorithm for the general case proceeds as follows [64]:

1. Compute the matrix $\mathbf{R}$ as indicated by Eq.4.25 and Eq.4.26;
2. If $s < N$ compute $\mathbf{Q}$ and $\mathbf{b}$ using Eq. 4.34, otherwise compute them using Eq. 4.32.
3. Initialize $\hat{\mathbf{x}}^{[0]}$ arbitrarily, $\mathbf{d}_0 = \mathbf{b} - \mathbf{Q}\hat{\mathbf{x}}^{[0]}$ and $\mathbf{g}_0 = -\mathbf{d}_0$
4. for $k = 1$ to $n_{it} \leq M$

(a) $\alpha_k = -\frac{\mathbf{g}_k^T \mathbf{d}_k}{\mathbf{d}_k^T \mathbf{Q} \mathbf{d}_k}$

(b) $\hat{\mathbf{x}}^{[k+1]} = \hat{\mathbf{x}}^{[k]} + \alpha_k \mathbf{d}_k$

(c) $\mathbf{g}_{k+1} = \mathbf{Q}\hat{\mathbf{x}}^{[k+1]} - \mathbf{b}$

(d) $\beta_k = -\frac{\mathbf{g}_{k+1}^T \mathbf{Q} \mathbf{d}_k}{\mathbf{d}_k^T \mathbf{Q} \mathbf{d}_k}$

(e) $\mathbf{d}_{k+1} = -\mathbf{g}_{k+1} + \beta_k \mathbf{d}_k$

end

5. If $s < N$ compute $\hat{\mathbf{a}} = \hat{\mathbf{x}}$, otherwise $\hat{\mathbf{a}} = \mathbf{R}^H \hat{\mathbf{x}}$.

6. Reconstruct the diffraction field $u(x, z)$ from the estimated Fourier coefficient vector $\hat{\mathbf{a}}$ using Eq. 4.23.

The presented CG based diffraction field algorithm is also employed to solve 3D scenarios, but there is a problem in the implementation of the algorithm for the 3D case as in the cases of the first algorithm proposed in this chapter and the algorithm presented in Chapter 3. In the implementation of these algorithms for 3D space scenarios, large memory spaces have to be allocated. Thus, these algorithms provide feasible solutions only for coarse objects.

The CG based algorithm for the 3D space scenarios is first published in [67]. As in the algorithm for 2D space scenarios, the algorithm for 3D space scenarios is also based on the inverse discrete Fourier transform. As in the previously mentioned algorithms, the diffraction field over the entire 3D space is formed by propagating plane waves. As a result of numerical issues, we assume that there are N^2 plane waves propagating in the 3D space. The diffraction field at a point in 3D space can be found from the propagating plane waves as [67]

$$\psi(x,y,z) = \sum_{n_f=-N/2}^{N/2-1} \sum_{m_f=-N/2}^{N/2-1} A_D(n_f, m_f) \exp\left\{ j\left[k^2 - (\frac{2B}{N} n_f)^2 - (\frac{2B}{N} m_f)^2\right]^{\frac{1}{2}} z \right\} \exp[j\frac{2B}{N}(n_f x + m_f y)] \quad (4.35)$$

where $A_D(n_f, m_f)$ denotes the complex amplitudes of the propagating plane waves. The bandwidth of the diffraction field is represented by B. The algorithm extended to 3D space is based on Eq. 4.35. The relationship given in Eq. 4.35 can be expressed as a matrix multiplication,

$$\mathbf{g}' = \mathbf{R}\mathbf{a} \tag{4.36}$$

where the vector $\mathbf{a}$ represents the complex amplitudes of the propagating plane waves as $A_D(n_f, m_f)$. In Eq. 4.35, these complex amplitudes of the plane waves are represented by a 2D array $\mathbf{A}_D$ as

$$\mathbf{A}_D = \left[\begin{array}{c|c|c|c} \mathbf{a}_1 & \mathbf{a}_2 & \dots & \mathbf{a}_N \end{array} \right]. \tag{4.37}$$

The 2D array $\mathbf{A}_D$ is converted into the vector $\mathbf{a}$ as

$$\mathbf{a} = \left[\begin{array}{c} \mathbf{a}_1 \\ \hline \mathbf{a}_2 \\ \hline \vdots \\ \hline \mathbf{a}_N \end{array} \right]. \tag{4.38}$$

The system matrix, $\mathbf{R}$, determines the relation between the field on the reference plane and the complex amplitudes of the plane waves in Eq. 4.35. The system matrix is computed as [67]

$$r = \left[\begin{array}{ccc|ccc|c|ccc} r_{1,1,1} & \dots & & r_{1,1,2} & \dots & r_{1,N,2} & \dots & r_{1,1,N} & \dots & r_{1,N,N} \\ \hline r_{2,1,1} & \dots & r_{2,N,1} & r_{2,1,2} & \dots & r_{2,N,2} & \dots & r_{2,1,N} & \dots & r_{2,N,N} \\ \hline & \vdots & & & \vdots & & \ddots & & \vdots & \\ \hline r_{s,1,1} & \dots & r_{s,N,1} & r_{s,1,2} & \dots & r_{s,N,2} & \dots & r_{s,1,N} & \dots & r_{s,N,N} \end{array} \right]. \tag{4.39}$$

The elements of the matrix $\mathbf{R}$ is obtained as

$$r_{l,n_f,m_f} = \exp\left\{ j\left[k^2 - (\frac{2B}{N} n_f)^2 - (\frac{2B}{N} m_f)^2 \right]^{\frac{1}{2}} z_l \right\} \exp[j(\frac{2B}{N} n_f x_l + \frac{2B}{N} m_f y_l)] \tag{4.40}$$

where x_l, y_l and z_l are the locations of the given samples over the 3D space. The vector $\mathbf{g}'$ denotes the diffraction field on the given samples in Eq. 4.35.

The complex amplitudes of the plane waves are obtained by the multiplication of $\mathbf{g}'$ by the pseudo inverse of $\mathbf{R}$. The algorithm is summarized as [67]

1. Compute the $\mathbf{R}$ by using Eq. 4.40 and Eq. 4.39
2. If $s < N^2$ compute $\mathbf{Q} = \mathbf{R}\mathbf{R}^H$ and $\mathbf{b} = \mathbf{u}$, otherwise compute $\mathbf{Q} = \mathbf{R}^H\mathbf{R}$ and $\mathbf{b} = \mathbf{R}^H\mathbf{u}$
3. Initialize $\hat{\mathbf{x}}^{[0]}$ arbitrarily, $\mathbf{d}_0 = \mathbf{b} - \mathbf{Q}\hat{\mathbf{x}}^{[0]}$ and $\mathbf{g}_0 = -\mathbf{d}_0$
4. for $n = 1$ to $n_{it} \leq N^2$
   (a) $\alpha_n = -\frac{\mathbf{g}_n^T\mathbf{d}_n}{\mathbf{d}_n^T\mathbf{Q}\mathbf{d}_n}$
   (b) $\hat{\mathbf{x}}^{[n+1]} = \hat{\mathbf{x}}^{[n]} + \alpha_n\mathbf{d}_n$
   (c) $\mathbf{g}_{n+1} = \mathbf{Q}\hat{\mathbf{x}}^{[n+1]} - \mathbf{b}$
   (d) $\gamma_n = -\frac{\mathbf{g}_{n+1}^T\mathbf{d}_n}{\mathbf{d}_n^T\mathbf{Q}\mathbf{d}_n}$
   (e) $\mathbf{d}_{n+1} = -\mathbf{g}_{n+1} + \gamma_n\mathbf{d}_n$
5. end
6. If $s < N^2$ compute $\hat{\mathbf{a}} = \mathbf{R}^H\hat{\mathbf{x}}$, otherwise $\hat{\mathbf{a}} = \hat{\mathbf{x}}$
7. Reconstruct the diffraction field on the reference plane from the estimated complex amplitudes of the plane waves by utilizing the inverse FT relation.

4.5 Comparison of the algorithms

To illustrate and evaluate the proposed algorithms, we use the diffracted field due to a simple function in both 2D and 3D space. First, the results obtained from 2D scenarios are illustrated and evaluated. Then, the results for 3D space scenarios are given.

In 2D scenarios, we have $M = 256$ lines with $N = 256$ samples per line. The range of p which represents the distance along z-axis, is taken as $[129, 384]$. The diffraction field over the entire space is computed from a simple function defined on the reference line by using Eq. 4.8. The defined simple function on the reference line is a unit amplitude square pulse with 32 samples located at the center of the reference line. The calculated field over the entire 2D space due to the function on the reference line can be seen in Figure 4.5(a). The evaluation of the performances of the algorithms based on according to normalized error on the reconstructed field and the computational complexity of the implemented algorithm. The normalized error on the reconstructed field over the entire space is computed as

$$\frac{\sum_{n=0}^{N-1}\sum_{p=129}^{384}|\psi'_D(n,p)-\psi_D(n,p)|^2}{\sum_{n=0}^{N-1}\sum_{p=129}^{384}|\psi_D(n,p)|^2} \tag{4.41}$$

where $\psi'_D(n,p)$ and $\psi_D(n,p)$ are the reconstructed and original diffraction fields over the entire space, respectively. The error on the reconstructed field is normalized by the power of the original field, hence the computed normalized error becomes unitless. The obtained normalized errors for the presented algorithms in this chapter are tabulated according to different given number of samples over the space, as shown in Table 4.1, 4.2 and 4.3. Each value of normalized error in the tables is obtained by having average of the errors obtained from 15 different selection of diffraction field samples taken over the entire space for each s. Thus, each reconstructed diffraction pattern corresponds to a different random choice of the positions of the s known data points within the field. In the numerical implementations of the algorithms, the complex arithmetic operations are needed such as complex multiplications and additions. Computation times of these operations can be affected by properties of the assembled hardware and the behavior of the installed operating system. To implement the proposed algorithms, large amount of complex operations have to be performed. Moreover, during the execution of the algorithms, large amount of data fetch and write

operations are needed. Therefore, actual computation times of the algorithms depend on not only the number of complex operations but also the computer architecture and the operating system behavior. Even if the actual computation time can not be determined only from the performed arithmetic operations, we assume that a good estimate of it can be obtained from the number of complex multiplications that are needed to implement the algorithm.

The algorithm based on the pseudo inversion of the system matrix $\mathbf{A}_{BF}$ provides the lowest normalized errors among the proposed algorithms even for the under-determined scenarios. But, implementation of the algorithm becomes costly when the number of given samples s is increased. The calculated normalized errors for different s are shown in Table 4.1. As expected, better reconstruction of the initial diffraction field is obtained when s is increased. Furthermore, perfect reconstructions are possible when s is equal to the number of samples on the reference line, N, or larger than N. In this algorithm, first the pseudo inverse of $\mathbf{A}_{BF}$ is taken, then the field over the entire space is computed from the reconstructed field on the reference line. The diffraction field between consecutive lines is computed by using Eq. 4.8. To implement Eq. 4.8, we need to compute the DFT algorithm twice. Common FFT algorithms, which can be implemented by having $\frac{N}{2}\log_2 N$ complex multiplications, are used to compute DFTs. As a result this, calculation of the diffraction field over the entire space due to the field on the reference line costs $M(N\log_2 N + N)$ complex multiplications. The first term in parenthesis comes from forward and inverse FFT algorithms and the second term is the multiplication of the discrete kernel by the DFT coefficients of the input field. The expression in the parenthesis has to be performed M times because there are M lines in the space. To compute the pseudo inverse of $\mathbf{A_{BF}}$, we chose to have Householder transformations. According to [90], the related number of complex multiplications is estimated as [1]

$$sN^2 - N^3/3. \tag{4.42}$$

The total number of complex multiplications for the matrix inversion method is [1]

$$sN^2 - N^3/3 + MN\log_2 N + MN. \tag{4.43}$$

Figure 4.5 shows simulations for values of s close to N when pseudo inversion of the system matrix is computed.

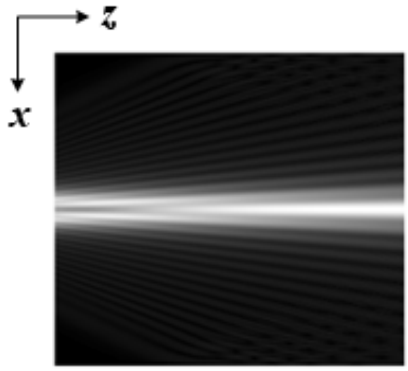

(a)

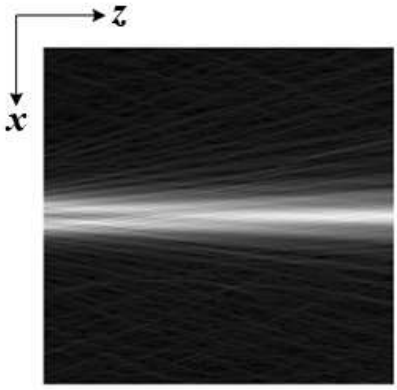

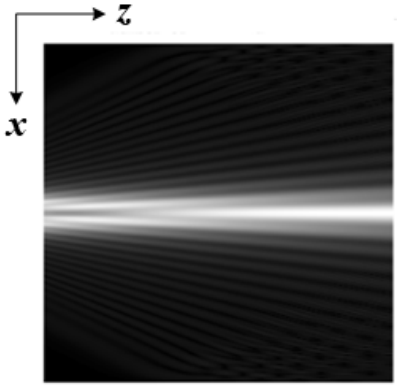

(b) (c)

Figure 4.5: Initial diffraction field over the entire 2D space; $N = 256$ samples per line(a) and reconstructed diffraction fields from s known data points by pseudo-inversion of the system matrix (b and c); (b) when $s = 230$; (c) when $s = 282$. (©2007 Elsevier. Reprinted with permission. Published in [1])

The normalized errors for the POCS based algorithm are also obtained from the average of 15 different random selections of locations of given samples for each s. The normalized errors are tabulated in Table 4.2. As in the previous algorithm, the error on the reconstructed field decreases when the number of given samples increases. Furthermore, the error on the reconstructed field changes by the number of performed iterations. By having more iterations, we can have less error on the reconstructed field. However, when the number of given samples are less than N, then we can not get perfect reconstruction even if we increase the number of iterations. It is observed from the implemented simulations that there is a certain number of iterations to get the saturated error on the reconstructed field for each s. This behavior can be seen in Figure 4.8 for 200 iterations. When the number of given samples are decreased, the number of iterations needed to reach the saturated error level is increased. Faster convergence can be achieved for larger values of s.

The total number of complex multiplications is used to determine the computational complexity of the POCS based algorithm. In each iteration of the POCS algorithm, the field over the M lines is computed by Eq. 4.8. As presented in the discussion related to pseudo inversion algorithm, Eq. 4.8 can be implemented by $N\log_2 N + N$ complex multiplications. In each iteration, the diffraction field over M lines are computed. Therefore, total number of complex multiplications needed to implement POCS algorithm is [1]

$$n_{it}\big(MN\log_2 N + MN\big), \tag{4.44}$$

where n_{it} denotes the number of iterations. The number of the given samples affect the computational complexity indirectly. As shown in Figure 4.6, more given points result in less iterations to achieve the same error level. There is a sharp transition right after $s = N$ in the number of iterations. When the number of given samples is larger than N, a reasonable number of iterations is enough to reach the desired error level. For example, when s is equal to $2N$, less

than 10 iterations are sufficient to have good reconstruction of the diffraction field. On the other hand, the computational complexity of the pseudo inversion algorithm is drastically increased when more samples are provided. In Figure 4.6, comparison of the computational complexities of pseudo inversion, POCS and CG based algorithms is illustrated. The number of iterations for the POCS algorithm becomes less when $s \geq 1.4N$ compared to pseudo inversion algorithm and the CG algorithm outperforms the other two algorithms when $s \geq 1.2N$. In Figure 4.7, the initial field and the reconstructed fields by POCS algorithms over the entire space are shown for values of s close to N.

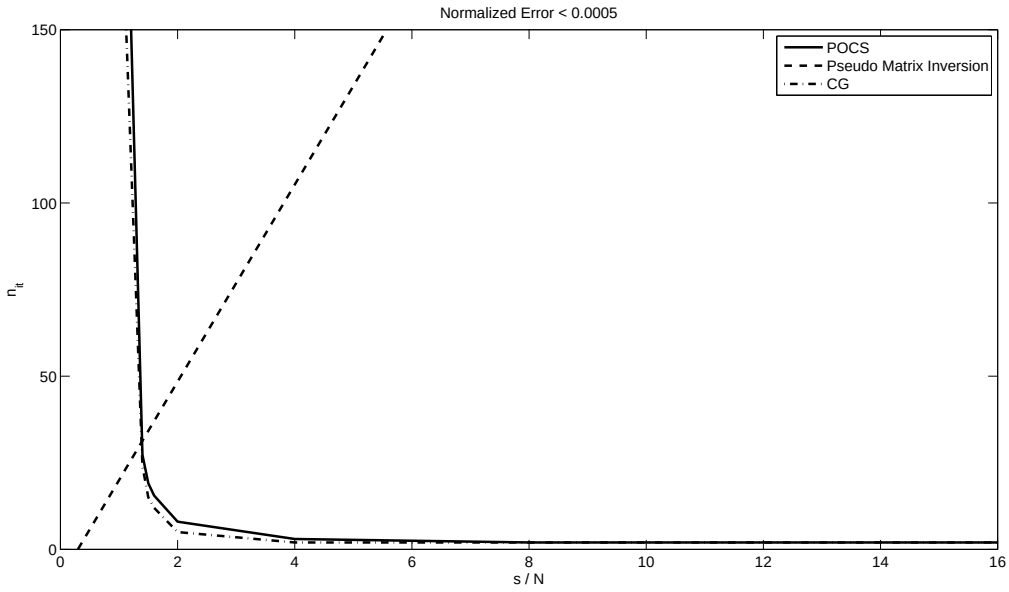

Figure 4.6: Evaluation of computational efficiency of the algorithms for different numbers of known samples s. Solid line: number of POCS iterations n_{it} needed to achieve normalized error < 0.0005. Dashed line: number of iterations for which POCS and matrix inversion methods give the same computational costs. Dashdot line: number of iterations needed for CG under the same normalized error conditions mentioned above.

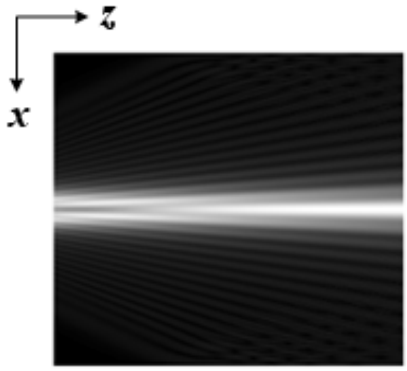

(a)

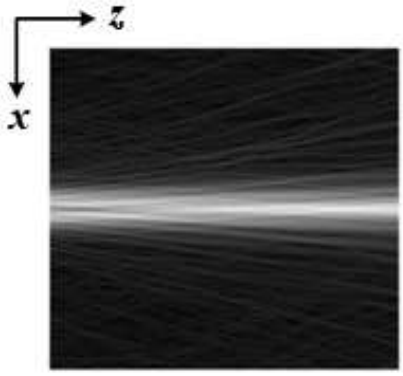

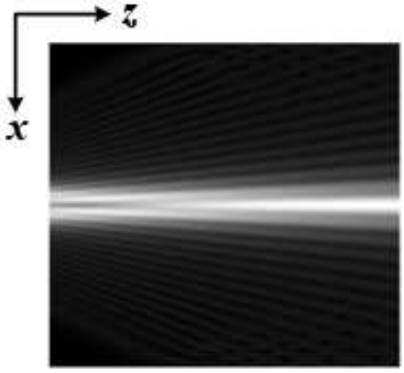

(b) (c)

Figure 4.7: Initial diffraction field over the entire 2D space; $N = 256$ samples per line(a) and reconstructed diffraction fields from s known data points (b and c) by POCS algorithm (b) when $s = 230$; (c) when $s = 282$. (©2007 Elsevier. Reprinted with permission. Published in [1])

Number of given samples = s	Ave. norm. error
77	0.6928
128	0.5112
179	0.3104
205	0.2176
230	0.0858
256	0.0000
282	0.0000
307	0.0000
333	0.0000
512	0.0000
1024	0.0000
2048	0.0000
4096	0.0000
8192	0.0000
16384	0.0000

Table 4.1: Normalized error of the matrix inversion method for different numbers of given data points over 2D space. Each normalized error is obtained by averaging the results of 15 simulations.(©2007 Elsevier. Reprinted with permission. Published in [1])

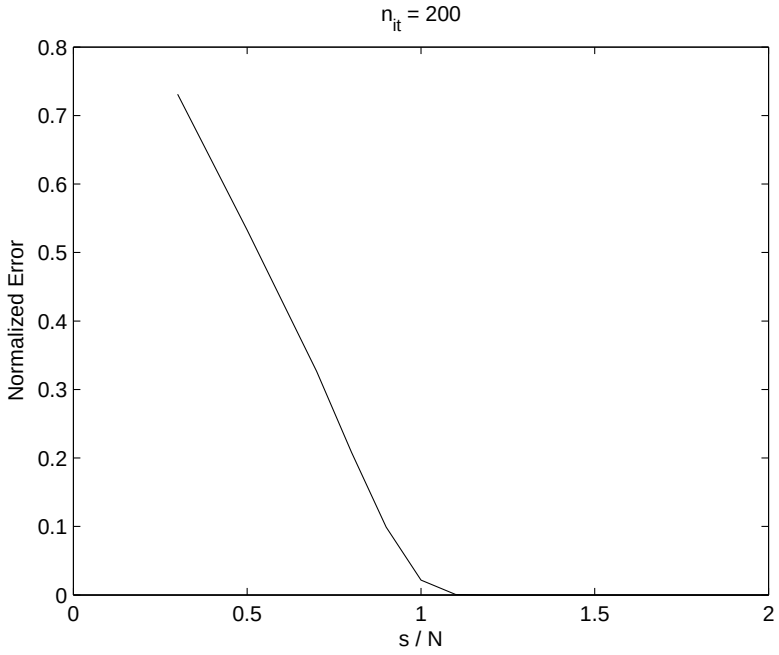

Figure 4.8: Normalized error for different numbers of known samples at 200 iterations. (©2007 Elsevier. Reprinted with permission. Published in [1])

s	Number of iterations n_{it}									
	10	20	30	50	100	200	300	500	1000	3000
77	0.7312	0.7312	0.7312	0.7312	0.7312	0.7312	0.7312	0.7312	0.7312	0.7312
128	0.5336	0.5328	0.5328	0.5328	0.5328	0.5328	0.5328	0.5328	0.5328	0.5328
179	0.3392	0.3288	0.3272	0.3264	0.3264	0.3264	0.3264	0.3264	0.3264	0.3264
205	0.2357	0.2183	0.2133	0.2101	0.2087	0.2084	0.2084	0.2083	0.2083	0.2083
230	0.1590	0.1304	0.1194	0.1098	0.1023	0.0991	0.0984	0.0981	0.0980	0.0980
256	0.1022	0.0708	0.0575	0.0441	0.0307	0.0216	0.0177	0.0138	0.0099	0.0053
282	0.0606	0.0311	0.0200	0.0104	0.0033	0.0007	0.0002	0.0000	0.0000	0.0000
307	0.0369	0.0127	0.0058	0.0017	0.0002	0.0000	0.0000	0.0000	0.0000	0.0000
333	0.0201	0.0048	0.0015	0.0002	0.0000	0.0000	0.0000	0.0000	0.0000	0.0000
512	0.0001	0.0000	0.0000	0.0000	0.0000	0.0000	0.0000	0.0000	0.0000	0.0000
1024	0.0000	0.0000	0.0000	0.0000	0.0000	0.0000	0.0000	0.0000	0.0000	0.0000
2048	0.0000	0.0000	0.0000	0.0000	0.0000	0.0000	0.0000	0.0000	0.0000	0.0000
4096	0.0000	0.0000	0.0000	0.0000	0.0000	0.0000	0.0000	0.0000	0.0000	0.0000
8192	0.0000	0.0000	0.0000	0.0000	0.0000	0.0000	0.0000	0.0000	0.0000	0.0000
16384	0.0000	0.0000	0.0000	0.0000	0.0000	0.0000	0.0000	0.0000	0.0000	0.0000

Table 4.2: Normalized error for different numbers of iterations n_{it} and given known data points s.(©2007 Elsevier. Reprinted with permission. Published in [1])

The assessment of the CG algorithm is obtained by the same scenarios used in the evaluation of the previous algorithms which are based on the pseudo matrix inversion and POCS. The Figure 4.9 shows the reconstructed fields by CG algorithm for values of s close to N. As it can seen form the Figure 4.9, when the number of samples is less than N, the deviation on the reconstructed field from the initial field can also be detected visually.

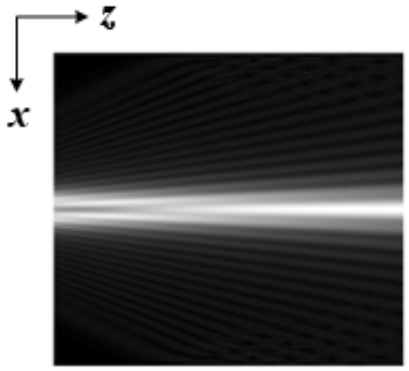

(a)

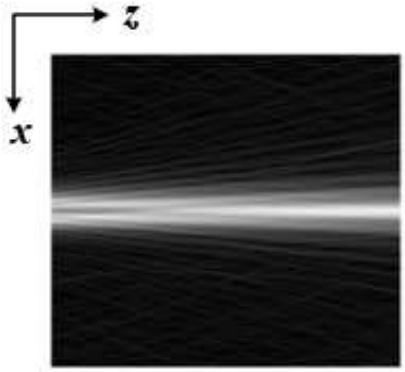

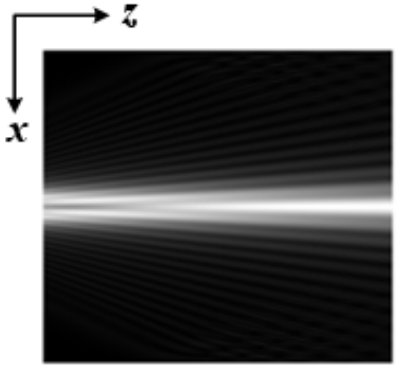

(b) (c)

Figure 4.9: Initial diffraction field over the entire 2D space; $N = 256$ samples per line(a) and reconstructed diffraction fields from s known data points (b-c); (b) CG algorithm with $s = 230$; (c) CG algorithm with $s = 282$.

The numerical evaluation procedure of the error is also the same as in the previously mentioned algorithms that is given by Eq. 4.41. Performance of the CG algorithm in reconstructing the initial field from the given samples is tabulated for different numbers of known data points s, in Table 4.3. For each s, the normalized errors are computed from 15 different random selections of data point sets which are taken from the field over the entire space. Then, the

	Conjugate gradient algorithm								Direct
	number of iterations n_{it}								matrix
s	10	20	30	50	100	200	500	1000	inversion
77	0.7242	0.7161	0.7161	0.7161	0.7161	0.7161	0.7161	0.7161	0.7161
128	0.8218	0.5402	0.5395	0.5395	0.5395	0.5395	0.5395	0.5395	0.5395
205	0.8867	0.4141	0.2368	0.2163	0.2154	0.2151	0.2150	0.2150	0.2150
256	0.9420	0.5081	0.3497	0.2151	0.1882	0.1417	0.0886	0.0553	0.0000
282	0.5781	0.1810	0.0702	0.0112	0.0059	0.0008	0.0000	0.0000	0.0000
307	0.3650	0.0654	0.0125	0.0003	0.0000	0.0000	0.0000	0.0000	0.0000
333	0.2163	0.0199	0.0016	0.0000	0.0000	0.0000	0.0000	0.0000	0.0000
384	0.0780	0.0017	0.0000	0.0000	0.0000	0.0000	0.0000	0.0000	0.0000
512	0.0067	0.0000	0.0000	0.0000	0.0000	0.0000	0.0000	0.0000	0.0000
1024	0.0000	0.0000	0.0000	0.0000	0.0000	0.0000	0.0000	0.0000	0.0000

Table 4.3: Reconstruction results for the rectangular field. The table shows the normalized error e for different numbers of given data points s. When CG algorithm is utilized different error values are shown for increasing number of iterations.

average of the computed normalized errors is taken as the error related to corresponding s value. We compare the error performance of the CG algorithm with the pseudo-inversion of the system matrix, because the best error performance is achieved by the algorithm based on pseudo-inversion of system matrix. The computational cost for the CG algorithm is again estimated by the number of the complex multiplications. For each iteration, the matrix $\mathbf{Q}$ is multiplied by a vector. Therefore, there will be $2N^2$ complex multiplications for the over-determined case for each iteration, where N is the number of plane waves. For the under-determined cases, CG algorithm presents poor error performance, thus computational complexity for these scenarios are not considered. To find the estimate of the complex amplitudes of the plane waves in n_{it} iterations, we need $2n_{it}N^2$ complex multiplications, but for the under-determined case we need sN additional complex multiplications to find the estimate of the complex amplitudes of the plane waves. The number of given samples implicitly affects the computational complexity, because an increment on the amount of given information content causes decrement on the number of iterations needed to achieve the desired level of error on the estimated amplitude of the plane waves. The

desired level of error is again taken as 0.0005. Figure 4.6 shows computational costs to achieve the desired level of error. As it can be seen form Figure 4.6, there is a sharp decrease on the computational costs right after $s = N$ and larger values of s, because the desired level of error reached in a small number of iterations. For instance, if the number of samples is taken as $s = 2N$, then the desired level of error is reached in less than 15 iterations.

All three algorithms provide exact reconstruction of the initial field if the number of given samples is equal to or larger than the degree of freedom of the stated problem of diffraction field calculation. Obviously, it is very rare to have linearly dependent data. As mentioned above the degree of freedom of the problem is determined by the number of plane waves forming the diffraction field over the entire space. The Figures 4.5, 4.7 and 4.9 can be used for visual evaluation of the reconstructed fields. As it can be seen from those reconstructed fields, there is not much visual difference between the results of the three methods.

All the proposed algorithms in this chapter can be extended to solve diffraction field over 3D space. Mathematical basis of extension to 3D is presented above. As a proof of concept, a simple scenario is implemented and illustrated. Please note that, these algorithms tested under several scenarios, but only one of them is presented. An illustration of the implemented scenario is shown in Figure 4.10

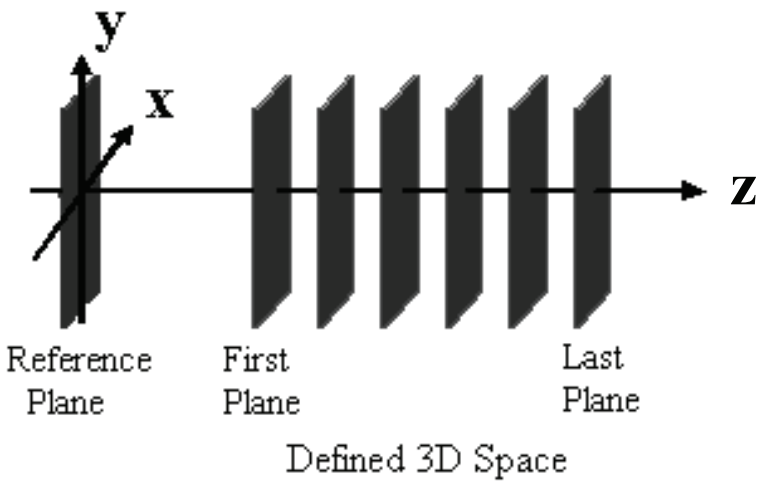

Figure 4.10: Illustration of the implemented 3D space scenario.

The pattern over the reference plane consists of N by N samples where $N = 64$. There are uniformly located 64 transversal planes in the illustrated 3D space and there is 64 by 64 uniform grid on each transversal plane. The samples are taken uniformly random from the space. The distance between the reference plane and the first transversal plane is equal to four. The original diffraction pattern on the reference plane is shown in Figure 4.11.

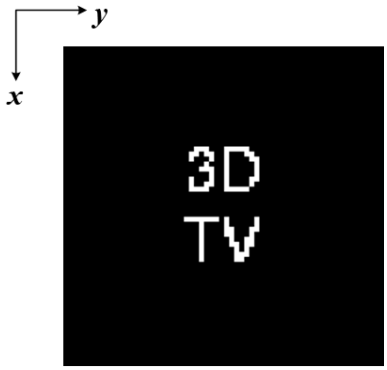

Figure 4.11: The original diffraction pattern defined on the reference plane, $z = 0$.

Typical results of the algorithms for 3D space scenarios can be seen in Figures 4.12, 4.13 and 4.14.

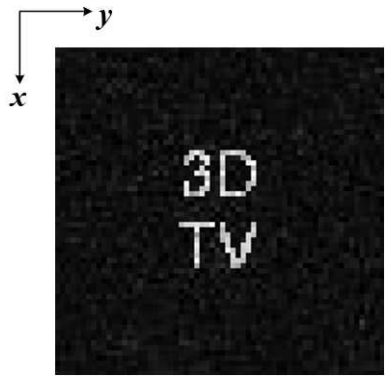

(a)

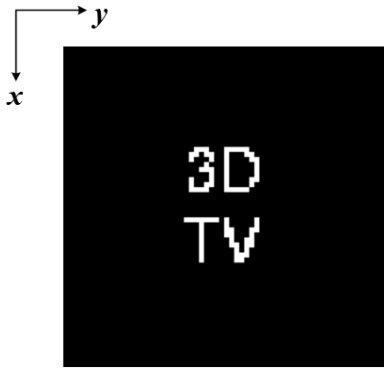

(b)

Figure 4.12: Magnitude of the reconstructed diffraction field over the reference plane when the algorithm based on pseudo inversion of the system matrix is employed. (a) with $s = 0.6N^2$ (b) with $s = 2N^2$.

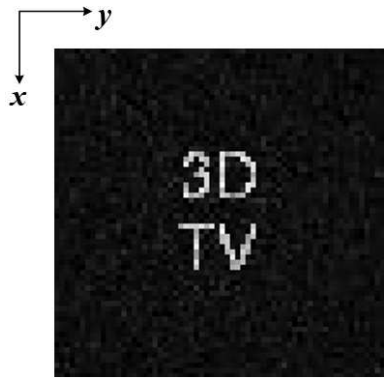

(a)

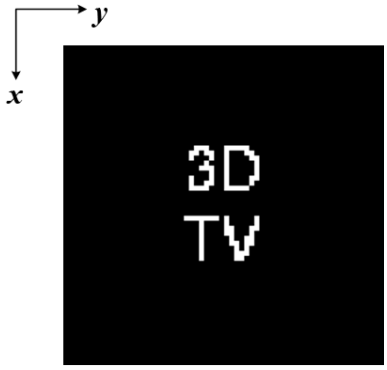

(b)

Figure 4.13: Magnitude of the reconstructed diffraction field over the reference plane when the POCS based algorithm is employed. The same scenario is implemented as in Figure 4.12 with $s = 0.6N^2$ (b) with $s = 2N^2$.

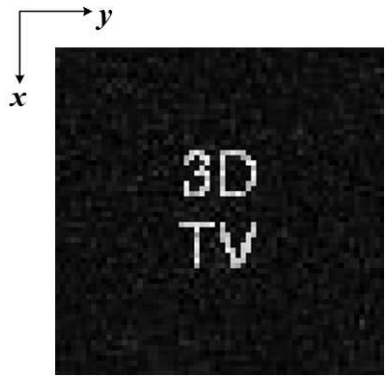

(a)

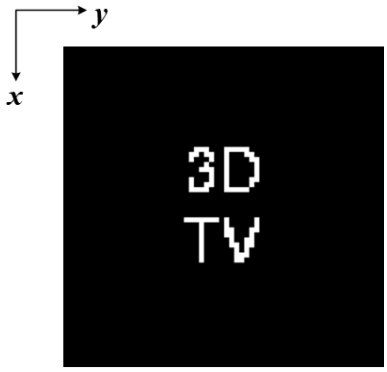

(b)

Figure 4.14: Magnitude of the reconstructed diffraction field over the reference plane when the CG based algorithm is employed. The same scenario is implemented as in Figure 4.12 with $s = 0.6N^2$ (b) with $s = 2N^2$.

As in the 2D space algorithms, when the number of given samples is equal to or larger than the degree of freedom of the problem, then the field over the entire space can reconstructed perfectly. In this scenario, the degree of freedom of the problem is N^2.

The performances of the algorithms can also be evaluated according to their computational complexities. We assume that the computational complexity of the algorithms are determined by the number of complex multiplications. When the number of samples are increased, faster convergence for the POCS and CG based algorithms is achieved. Thus, the computational complexities of the POCS and CG based algorithms decrease, because their computational complexities are

directly determined by the number iteration. To implement the POCS based algorithm, we need

$$n_{it}(MN^2 \log_2 N + MN^2) \tag{4.45}$$

complex multiplications, where n_{it} denotes the number of iterations, M is the number of transversal planes in the space and N^2 is the number of samples over a transversal plane. The number of iterations is related to the number of the given samples implicitly. For the CG based algorithm, we need

$$2n_{it}N^4 + sN^2 + MN^2 log_2 N \tag{4.46}$$

complex multiplications in the implementation. The number of iterations again related to the number of given samples. On the other hand, the computational complexity of the algorithm based on pseudo inversion of the system matrix increases when the number of the given samples is increased. Implementation of the pseudo inversion of the system matrix is costly. We need

$$sN^4 - N^6/3 + 2N^2 log_2 N + MN^2 \tag{4.47}$$

where s is the number of given samples.

4.6 Effect of sample locations on the solution

Proposed field model algorithms provide least square solution due to the given samples. If the amount of information is enough to reconstruct the initial field over the space, then perfect reconstruction can be obtained. Performances of the proposed algorithms are affected from both the number of given samples and their locations. There are some cases that even if the number of given samples is larger than the number of plane waves, perfect reconstruction is not possible. In this section, how the performances of the proposed field algorithms are affected by the locations of the given samples is presented. To have a comparison, performance

of the source model algorithm compared to these field model algorithms in this chapter is investigated in Chapter 5 under the same scenarios used in this section.

The effect of the number of given samples on the reconstruction of the field is already mentioned in the Section 4.5. But, there are some scenarios where even if the number of given samples is larger than the degree of freedom of the problem, perfect reconstruction may not be possible. The amount of information is based not only on the number of given samples but also on how the given samples are distributed over the space. The dependency between the samples is determined by their distribution over the space. For instance, the given samples are independent when they are taken over a transversal planar surface. The dependency can also be kept at a minimum when the samples are taken uniformly random. When the dependency between the samples are high, then we can not reconstruct the diffraction field perfectly. Then, to get better reconstruction, we have to increase the number of samples; this increases the amount information.

Accuracy in the solution is determined by the condition number of the system matrix. The condition number of a matrix is equal to the ratio of the largest eigenvalue to smallest eigenvalue [75]. In this section, we scrutinize how the solution is affected by the distribution of the given samples over the space. The effect of the distribution of the samples over the entire space is investigated by the eigenvalue distribution of the system matrix, $\mathbf{A}_{BF}$, that is defined in Section 4.2. The algorithm based on pseudo inversion of the system matrix is used among the three algorithms for performance evaluation according to locations of the given samples, because minimum amount of normalized error can be yielded by this algorithm. To reconstruct the initial field perfectly, the condition number of the system matrix has to be close to one. If the condition number of the system matrix is large, then the problem becomes ill-conditioned and even small numerical errors induce large amount of errors on the reconstructed field [75]. In

this section, we analyze the distribution of the eigenvalues under several scenarios to understand when the perfect solution possible.

The method used to analyze the effect of the distribution pattern of the given samples over the space on the solution is tested by various complex valued functions, but only the simulation results of the field diffracted due to a unit-square function, which is used in Section 4.5, are presented. The diffraction field over the entire space is computed by using Eq. 4.8. The space is formed by $M = 256$ transversal lines and each transversal line has $N = 256$ samples. Sampling periods in both x- and z-axes are the same, and taken as $X = \lambda$. As it is presented in Section 4.5, when the number of given samples is less than the degree of freedom of the problem, perfect reconstruction can not be achieved. Therefore, in this section the performance assessment of the field algorithm, based on pseudo inversion of the system matrix, is tested for over-determined systems. Hence, the number of given samples over the entire space is chosen as $1.2N \simeq 307$.

To have a better visual assessment, the magnitude of the initial and the reconstructed diffraction fields along the reference line is repeated N times to get a square (N by N) image. According the mentioned visualization method, the diffraction pattern on the reference line is illustrated as in Figure 4.15.

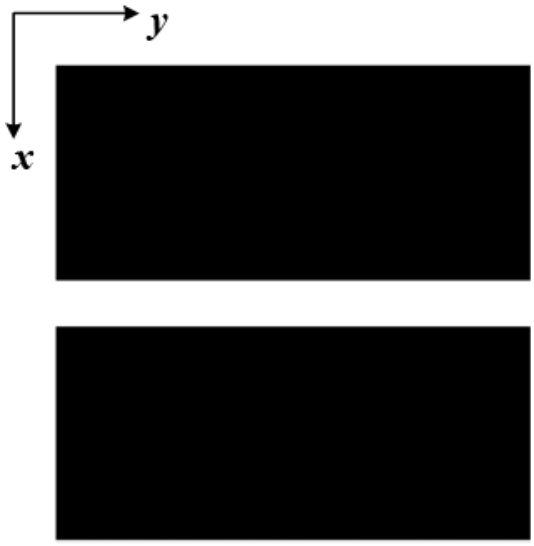

Figure 4.15: Magnitude of the synthetically generated diffraction field on the vertical reference line that is repeated N times horizontally to form N by N image for visualization purposes.

The magnitude of the diffraction field due to the synthetically generated diffraction field on the reference line over the entire 2D space is shown in Figure 4.16.

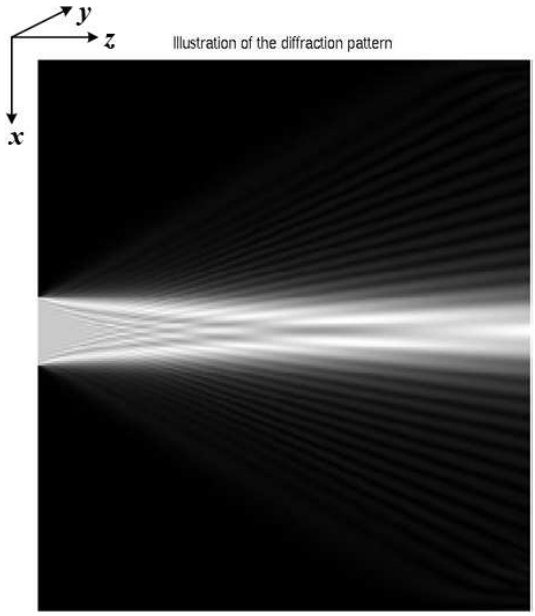

Figure 4.16: Magnitude of the diffraction field over entire 2D space.

The similarity relations between the given samples can be detected by analyzing the eigenvalue distribution of the $\mathbf{A}_{BF}$ matrix. If the given samples are highly correlated, most of the eigenvalues of the $\mathbf{A}_{BF}$ matrix will be practically zero. Thus, pseudo inverse of the $\mathbf{A}_{BF}$ will not provide the perfect reconstruction of the initial diffraction field, because of being ill-conditioned. One of the preferable ways to increase the number of non-zero eigenvalues is to take samples of the diffraction field over the entire space uniformly random. Another way to decrease the condition number is to take the samples within a region which has a full extent along the transversal axis. Then, approximately N samples is enough to have full rank $\mathbf{A}_{BF}$ matrix.

To see the impact of the distribution of the samples on the reconstruction the diffraction field on the reference line, we start with investigating the effect of the depth of the region along the longitudinal axis. In the first scenario, the distance from the region in which the samples are given to the reference line is taken as 100λ and its thickness varies from 4λ to 32λ along the longitudinal axis. Figure 4.17 shows the locations of the given samples over the space for the implemented scenarios. The perfect reconstruction of the diffraction fields on the reference line is achieved by the implemented scenarios, as illustrated in the Figure 4.17. The eigenvalue distribution of $\mathbf{A}_{BF}$, as shown in Figure 4.19, also indicates that perfect reconstruction is expected for these type of scenarios. All cases shown in Figure 4.17 yield the same perfect reconstruction shown in Figure 4.18. To have a convenient visual evaluation an N by N image is formed by repeating the reconstructed pattern N times, as described before.

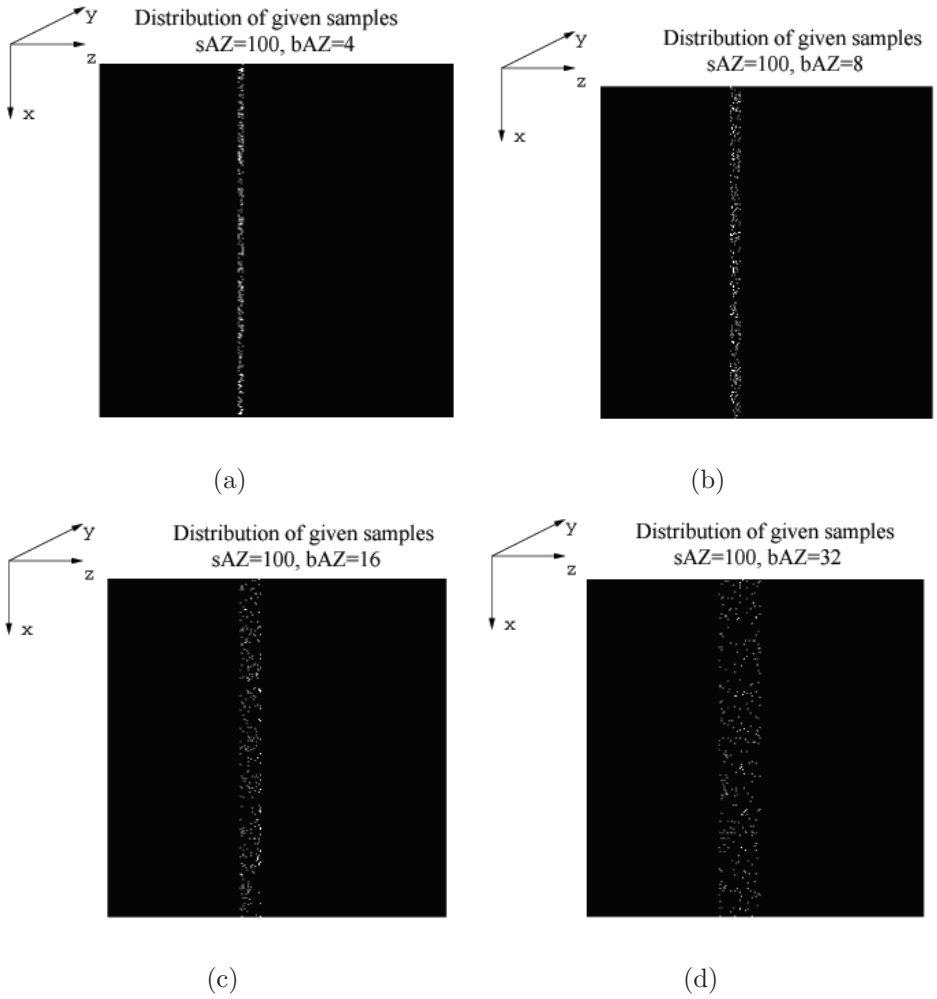

Figure 4.17: (a) Locations of the given data points. The thickness of the volume which contains all data points is 4λ and the distance between this volume and the reference line is 100λ. The reference line is at $z = 0$. The number of given samples, s, is taken as 307. (b) The thickness is 8λ. (c) The thickness is enlarged to 16λ. (d) to 32λ. (©2008 IEEE. Reprinted with permission. Published in [2])

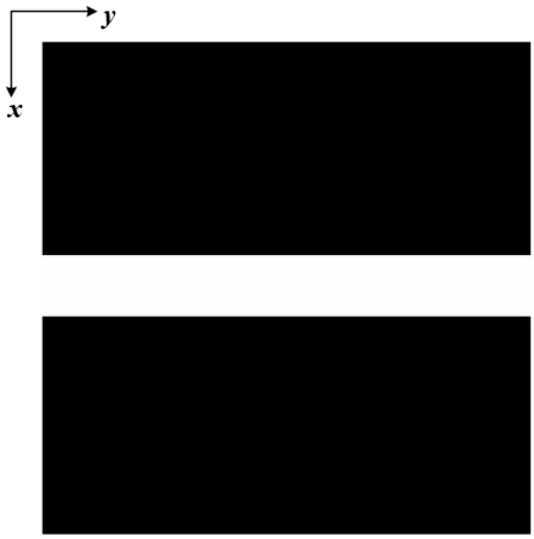

Figure 4.18: Reconstructed field on the reference line under the scenarios illustrated in Figure 4.17. To have conventional visual evaluation over N by N image, the reconstructed field on the vertical reference line is repeated N times horizontally.

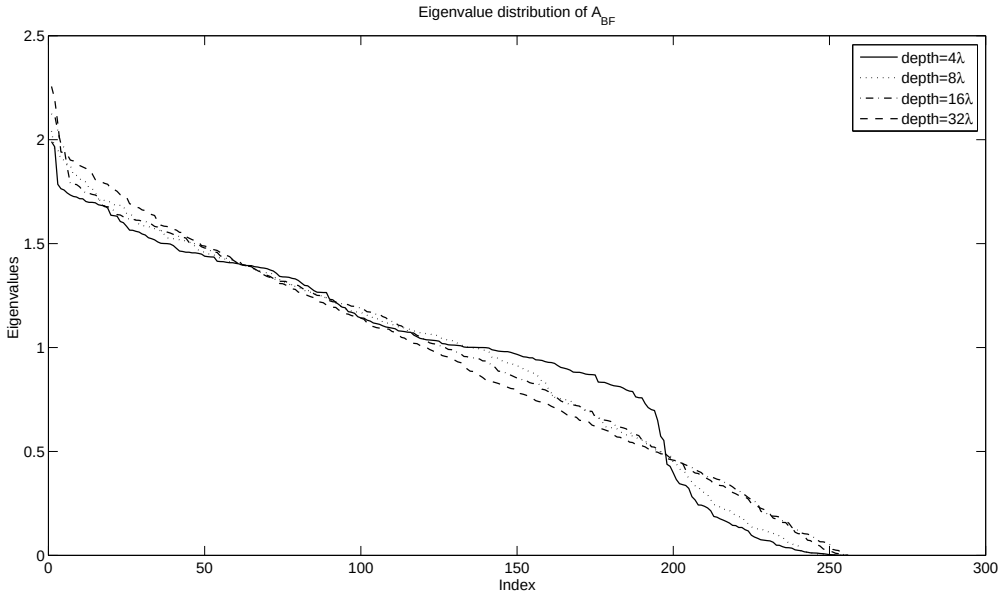

Figure 4.19: Eigenvalue distribution of the matrix $\mathbf{A}_{BF}$ under the scenarios illustrated in Figure 4.17.

In the second scenario, the given samples are taken within an isosceles shaped region. The number of given samples is again chosen as $s = 307$. In this scenario, the region is enlarged by changing the angle of the isosceles. The effect of changing the shape of the region is investigated. As it can be seen from the eigenvalue distribution of the $\mathbf{A}_{BF}$ matrix shown in Figure 4.23, perfect solution may not be possible when the angle of the isosceles is too small.

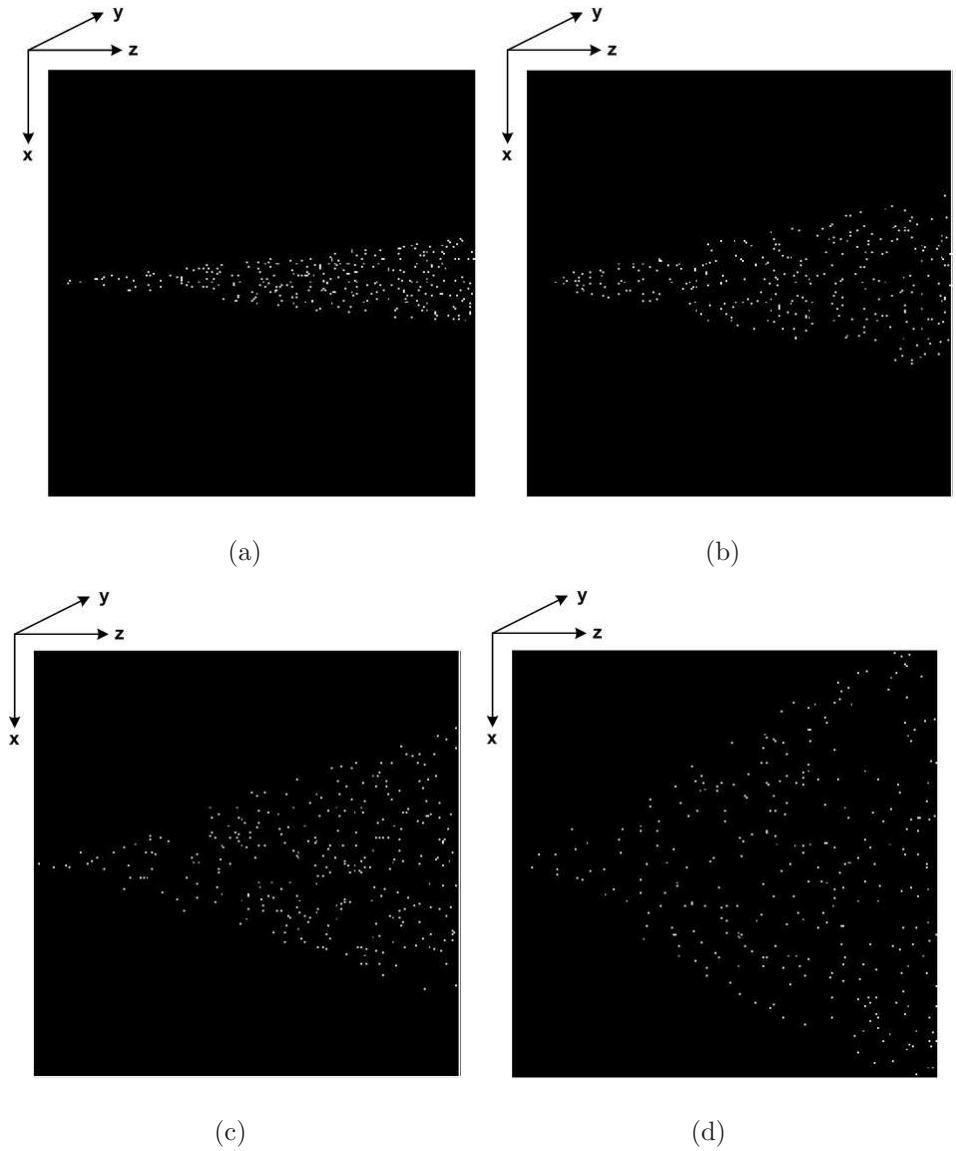

Figure 4.20: Locations of the given data points over the 2D space. The reference line is defined as $z = 0$. The angle of the isosceles is changed and the distance between the region in which the samples are given and the reference line is taken as 100λ. (a) angle $= \frac{2\pi}{30}$. (b) angle $= \frac{2\pi}{15}$. (c) angle $= \frac{2\pi}{10}$. (d) angle $= \frac{2\pi}{6}$.

The reconstructed patterns can be seen in Figure 4.22 when the samples are taken over the space as shown in Figure 4.20. Perfect reconstruction can not be achieved for the implemented scenarios illustrated in Figure 4.20(a), 4.20(b) and 4.20(c). There is an oscillating patterns on the reconstructed fields. Those oscillating patterns can be seen from Figure 4.21(a) and 4.21(b). The normalized errors for the reconstructed patterns in Figures 4.22(a) and 4.22(b) are 0.08331 and 0.07026, respectively.

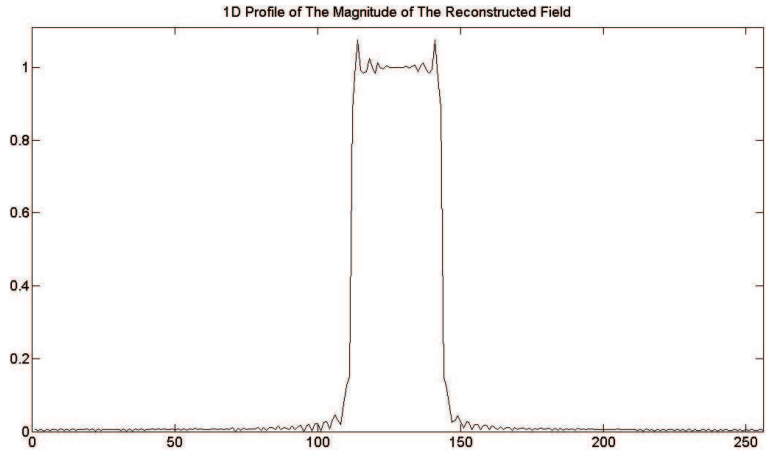

(a)

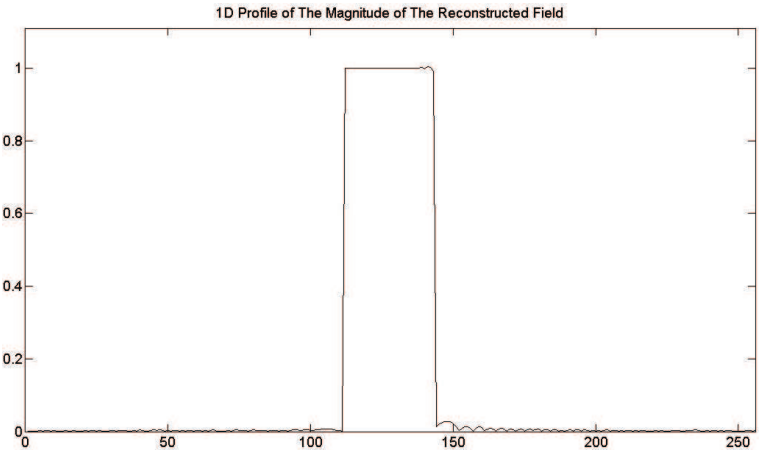

(b)

Figure 4.21: 1D cross-section of the magnitude of the reconstructed field on the reference line (a) 1D profile for the scenario shown in Figure 4.20(a). (b) for the scenario illustrated in the Figure 4.20(b).

Even the difference between the initial field and the reconstructed field can not be detected visually, there is a small amount of normalized error when the angle of the isosceles is chosen as $\frac{2\pi}{10} radians$. The computed normalized error for this scenario is 0.00137. Perfect reconstruction is obtained when the angle is $\frac{2\pi}{6} radians$. It is also seen from the Figure 4.23 which shows the eigenvalue distribution of the $\mathbf{A}_{BF}$ matrix, normalized error on the reconstructed fields decreases when the angle of isosceles is chosen larger.

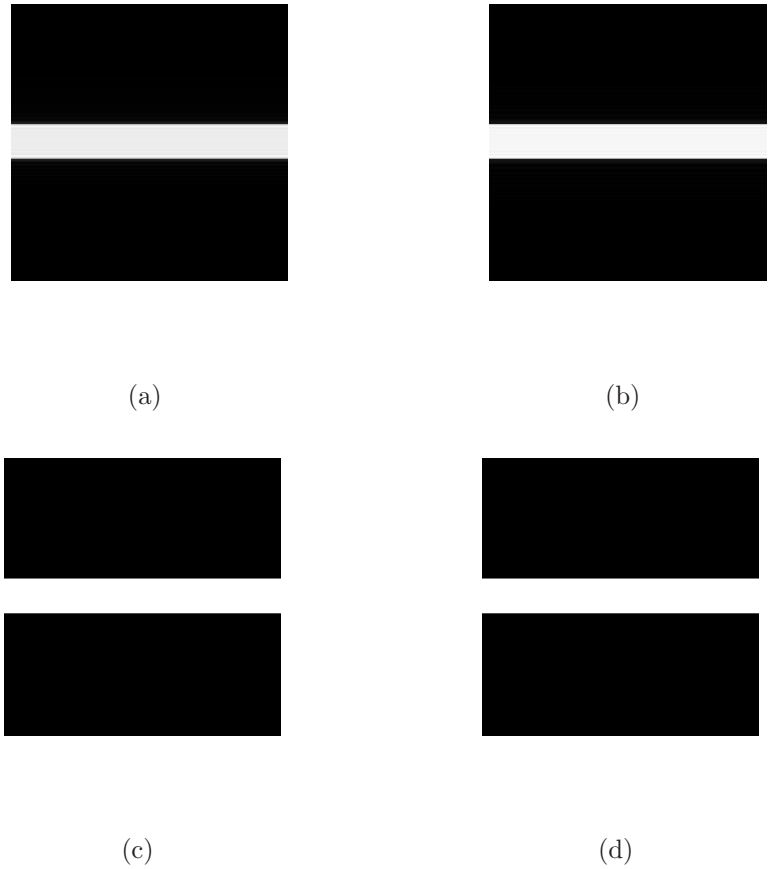

(a) (b)

(c) (d)

Figure 4.22: Reconstructed fields on the reference line under the scenarios illustrated in Figure 4.20. (a) Reconstructed field for the scenario shown in the Figure 4.20(a). (b) for the scenario illustrated in the Figure 4.20(b). (c) for the scenario illustrated in the Figure 4.20(c). (d) for the scenario illustrated in the Figure 4.20(d).

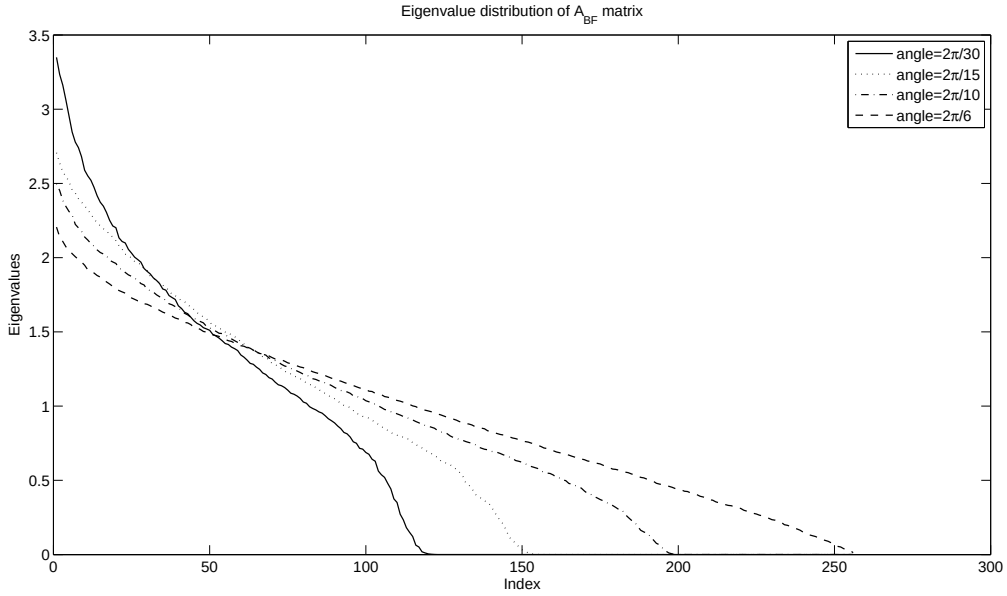

Figure 4.23: Eigenvalue distribution of the matrix $\mathbf{A}_{BF}$ under the scenarios illustrated in Figure 4.20.

In the third scenario, we investigate the behavior of the field model when the samples are taken over a smooth region which is chosen as a circle over the 2D space. Then, we change the radius of the circle to investigate the eigenvalue distribution and to find out whether the perfect reconstruction is possible under these type of sample distributions, or not. In this scenario, the number of given samples is more than the number of samples along the transversal line. Also, when we increase the radius of the circle, the number of given samples which are taken into consideration becomes multiple times than the number of plane waves forming the diffraction field over the entire space. A 3D illustration of the implemented scenario is given in Figure 4.24.

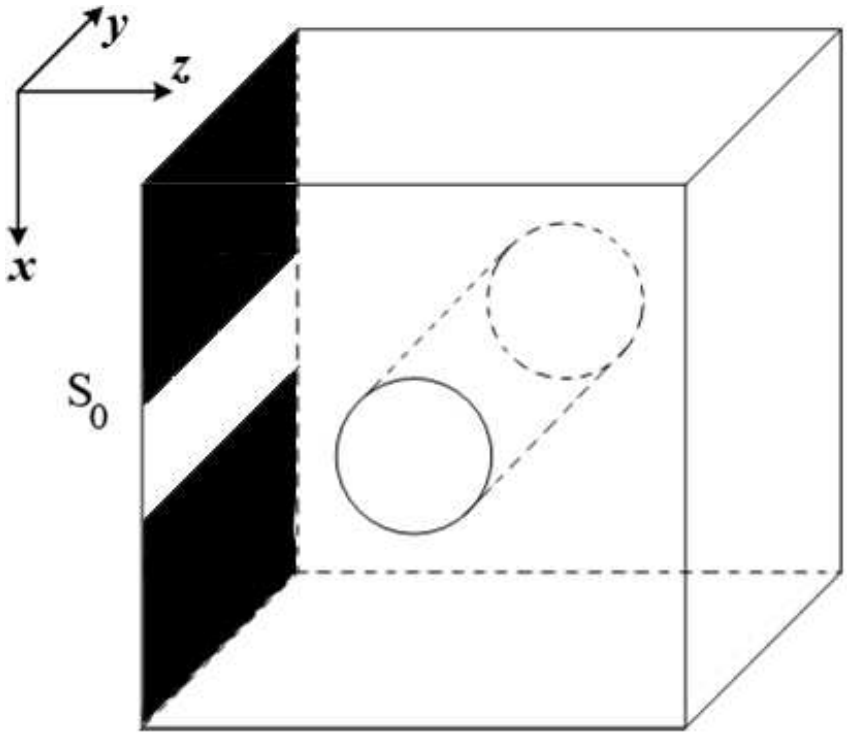

Figure 4.24: A 3D illustration of the implemented scenario.

For instance, the number of given samples for the implemented scenario shown in the Figure 4.25(a) is 317 and the calculated normalized error for the scenario is 0.36928. Normalized error is computed using Eq. 4.41. For the next scenario given in Figure 4.25(b), the number of given samples becomes 1257, but the normalized error in this scenario is considerably high: 0.15674. In the next scenario the radius of the circle is taken as 30λ, so the number of given samples is increased to 2821. Illustration of the implemented scenario is given in Figure 4.25(c). Even if the number of samples is more than 10 times of the degree of freedom of the problem, the normalized error is still significantly high. The error is computed as 0.10245. When the radius is taken as 40λ, then the number of samples becomes 5025. The locations of the samples can be seen from Figure 4.25(d). The reconstructed and the initial patterns looks like the same, but there is still considerable amount of normalized error on the reconstructed pattern. Normalized error is calculated as 0.07710. The illustrations of the implemented scenarios are given in Figure 4.25.

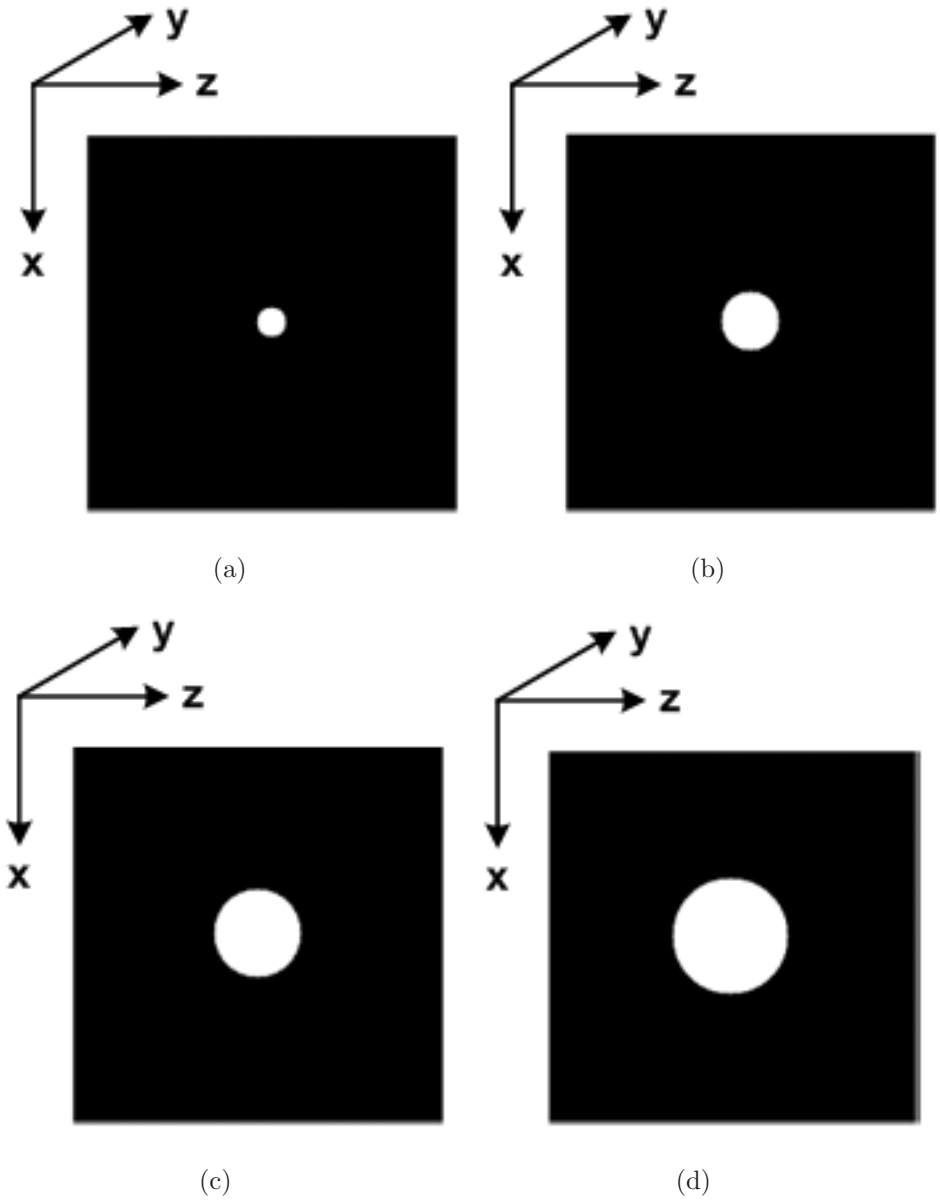

Figure 4.25: Locations of the given data points over the 2D space. Samples are taken from a circle shaped region. The radius of the circle is changed. The reference line is taken as $z = 0$. (a) radius = 10λ. (b) radius = 20λ. (c) radius = 30λ. (d) radius = 40λ.

The reconstructed patterns related to the scenarios shown in Figure 4.25 by the pseudo-inversion of the $\mathbf{A}_{BF}$ matrix can be seen in Figure 4.26. Perfect reconstruction can not be achieved for the implemented scenarios illustrated in Figure 4.25 even the number of given samples is larger than the number of plane

waves used in the implemented scenario. The difference between initial and the reconstructed patterns can also be detected visually. For the small radius scenarios, normalized error is significantly high and as expected normalized error decreases when the radius is increased. This result can also be interpreted from the eigenvalue distribution of the $\mathbf{A}_{BF}$ matrix shown in Figure 4.27 under the scenario given in Figure 4.25.

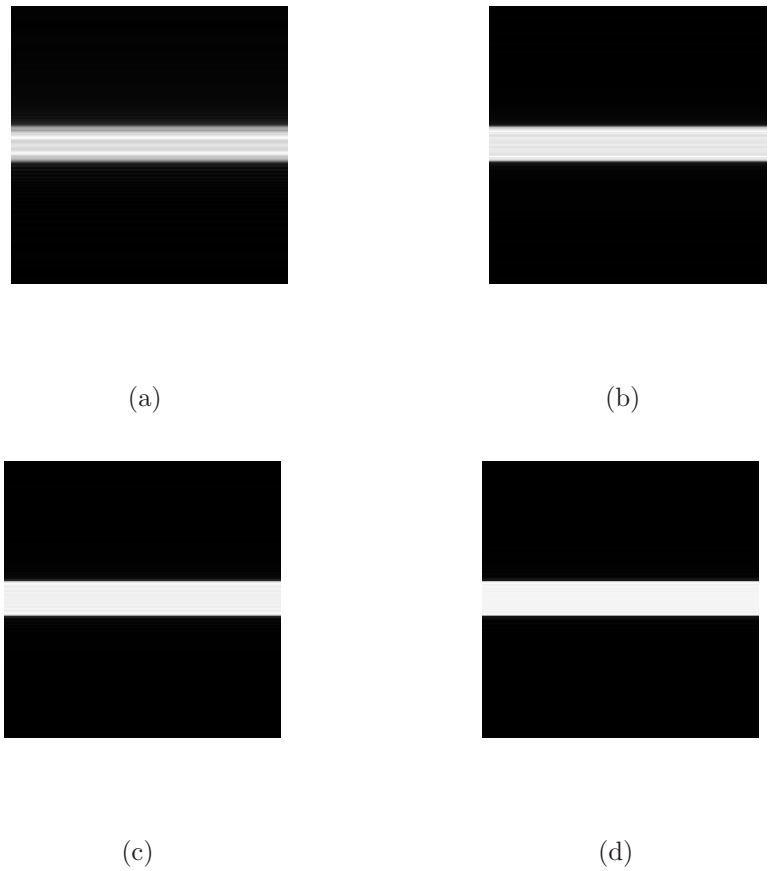

(a) (b)

(c) (d)

Figure 4.26: Reconstructed fields on the reference line under the scenarios illustrated in Figure 4.25. (a) Reconstructed field for the scenario shown in Figure 4.25(a). (b) for the scenario illustrated in Figure 4.25(b). (c) for the scenario illustrated in Figure 4.25(c). (d) for the scenario illustrated in Figure 4.25(d).

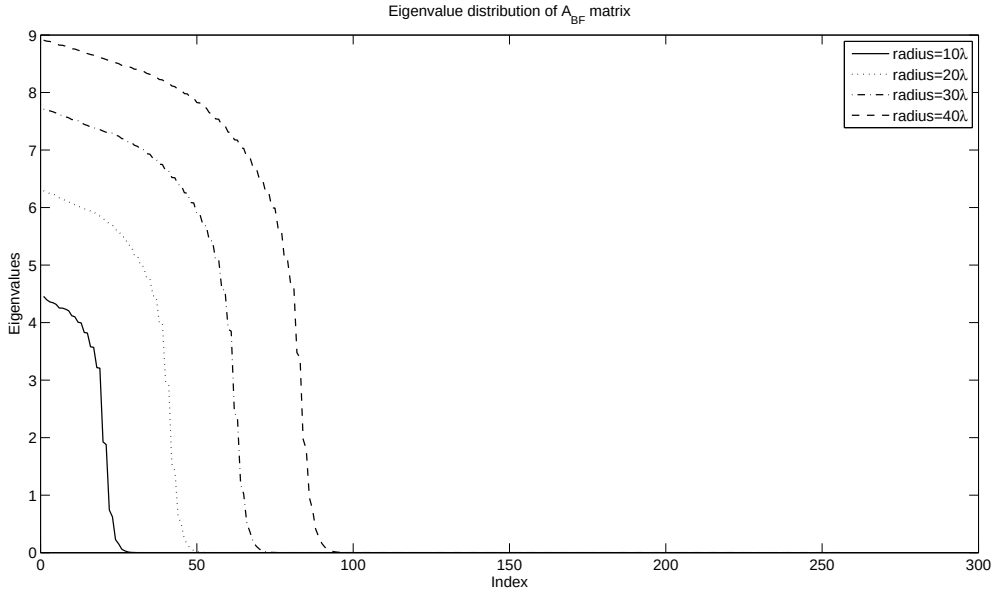

Figure 4.27: Eigenvalue distribution of the matrix $\mathbf{A}_{BF}$ under the scenarios illustrated in Figure 4.25.

The distribution the samples over the space affects the dependency of the diffraction field information gathered from the samples. Dependency of the samples determines the accuracy on the solution: When the dependency increases, the accuracy on the solution decreases; and then, we can not obtain perfect reconstruction of the initial field. Even if we have the same number of given samples, the accuracy on the solution depends on the locations of the given samples over the space. From the presented simulation results, it can be seen that the dependency decreases if the samples are taken uniformly random from the volume that is occupied by the object. When the samples are taken regularly, the dependency of the samples may increase; and the accuracy of the solution degrades. The dependency can also be decreased by taking the samples from a region which has full extent along the transversal axis.

In this chapter, in addition to the field model algorithm presented in Chapter 3, three more algorithms based on field model approach are presented. All

three of them use PWD in calculation of the diffraction field. Their performances are evaluated by their normalized errors and computational complexities related to the number of given samples. The algorithm based on pseudo inversion of the system matrix yields the minimum normalized error among all the algorithms proposed in this chapter even for the under-determined scenarios. Therefore, it is used in the performance evaluation related to the locations of the given samples. It can be seen from the simulation results that random selection of the positions of the samples usually provides independent samples and as a result perfect reconstruction can be achieved.

Chapter 5

Effect of distribution of samples on the source model performance

Exact diffraction field over the entire space can be computed by using the algorithms proposed in Chapters 3 and 4, but their associated computational complexities can be rather high. By computing an approximation of the diffraction field over the entire space instead of the exact one, computational complexity can be reduced significantly. One of the commonly used approach to reduce the computational complexity in the field computation is to superpose the diffraction fields that are assumed to be emanated from the samples of the object. Although, the field over the entire space may not be computed exactly by such models, the complexity in field computation can be significantly decreased to feasible levels. We call these kinds of diffraction field computation methods as the source model. In the literature, several elegant source model algorithms are proposed in [11,73,74,91]. Implementations of the source model based algorithms is rather straightforward because mutual couplings between the diffracted fields due to the elementary building blocks of the object are not taken into consideration. After computing the diffracted fields emitted by the elementary building blocks, it is assumed that a simple superposition over those diffraction fields will

give the diffracted field due to the object. In some scenarios, there will be a considerable amount of difference between the exact and such computed fields based on the source model. These deviations are highlighted by the presented scenarios in [2]. In this chapter, we will investigate the performance of the source model algorithms under several scenarios. Performance evaluation is determined by the visual evaluation on the reconstructed patterns. To illustrate the amount of deviation, some simulations which are based on various different distribution of the given samples over the space are presented. Even if the source model is tested under many conditions, only a few of them are presented this chapter. Moreover, in this work, we deal with the diffraction fields from 1D signals over 2D space, but it can be extended to diffraction from 2D signals over 3D space as in [67].

5.1 Numerical experiments of an algorithm based on the source model approach

Source model approach is based on the superposition of the diffraction fields that are assume to be emanating from the elementary building blocks of an object. The elementary building blocks are chosen as points whose values are obtained from the samples of the field over the surface of the object in the implemented algorithm in this chapter. The diffracted field due to the sample points are computed according to the Rayleigh-Sommerfeld (RS) diffraction integral kernel. To compute the field over the entire space, first, we compute the field on a hypothetical line (2D space) which is called as the reference line. Then, the field over the entire space can be computed rapidly using Eq. 4.10.

Depending on the distribution of the elementary building blocks over the space, the effect of mutual couplings between the emitted fields from those building blocks can be significant. A simple example can be helpful to clarify the

mutual coupling between the emitted fields from those building blocks. An illustration of the implemented scenario is given in Figure 5.1.

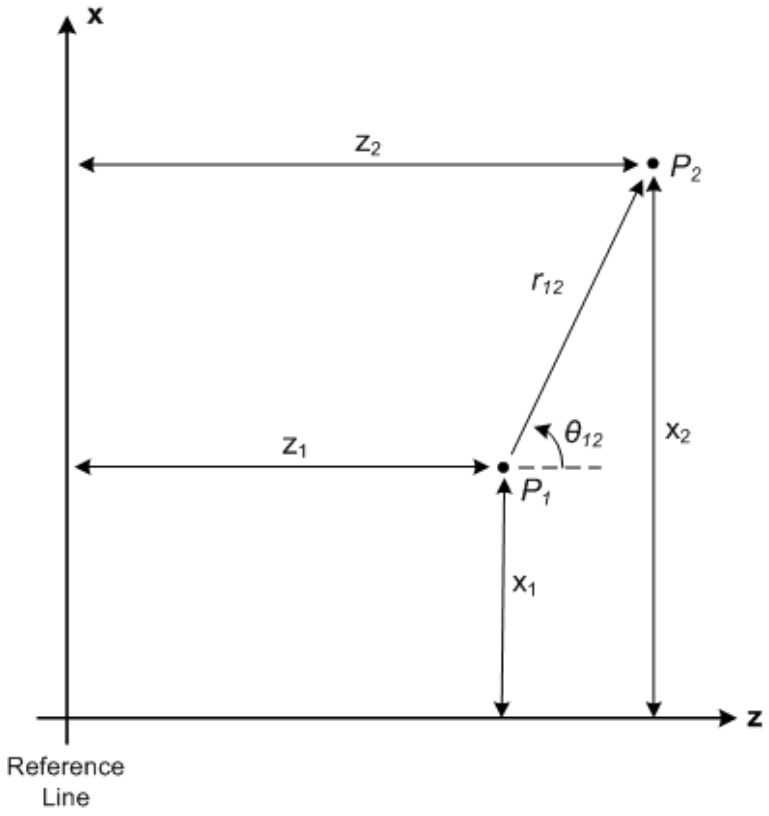

Figure 5.1: Illustration of a 2D space scenario that is used to show possible mutual coupling in the source model approach.

In the implemented scenario, there are two point light sources which are located at P_1 and P_2; and the field over the entire space is created by those point sources. According to the source model approach, the field over the reference line is computed by superposing the emitted fields by those point sources. RS diffraction integral kernel given in Eq. 2.12 is used to find the emitted fields due to those point sources. The effect of deviation can be seen when the field at one of the point source (i.e., P_1) is reconstructed by using the computed field over the reference line. The reconstructed field on P_1 is again calculated by using RS diffraction integral and the computed field on the reference line. However, the reconstructed field is different from the initial one. The deviation from the initial

field is found as

$$\begin{aligned}\Delta &= \psi(x_2, z_2)\frac{z_1 - z_2}{(x_1 - x_2)^2 + (z_1 - z_2)^2}\exp(j\frac{2\pi}{\lambda}\sqrt{(x_1 - x_2)^2 + (z_1 - z_2)^2}) \\ &= \psi(x_2, z_2)\frac{\cos\theta_{12}}{|\mathbf{r}_{12}|}\exp(j\frac{2\pi}{\lambda}|\mathbf{r}_{12}|) \qquad (5.1)\end{aligned}$$

where $\mathbf{r}_{12}$ is the vector between point sources P_1 and P_2, and θ_{12} denotes the angle between the vector $\mathbf{r}_{12}$ and z-axis. This is exactly the additional field imposed on P_1 by a source at P_2. Similarly, the reconstructed and the original values at P_2 would also deviate due to the effect of the source at P_1 to the point P_2. The deviation from the initial field depends on the initial field values at the other points sources and their mutual positions over the space. As a result of the mutual couplings between the fields emitted by the point sources, the source model approach may not provide the exact field over the entire space. Furthermore, when the positions of the point sources which represent the object are changed, the calculated field may also change.

The field on the reference line is obtained by the superposition of the fields which are emanated from the point light sources and each emanated field is expressed by a column vector, $\mathbf{r}^H(p_i, n_i)$ where ^{H} denotes the conjugate transposition. Conjugate transposition is needed for back-propagation from the sample point to the reference line. This column vector is obtained from the n_i^{th} row vector of $\mathbf{A}$ matrix as defined in Eq. 4.11, with $p = p_i$. Structure of the $\mathbf{A}$ matrix can be found in Chapter 4. The implemented source model can be summarized as

$$\mathbf{f} = \sum_{i=1}^{s} y_i \mathbf{r}^H(p_i, n_i). \qquad (5.2)$$

where s is the number of given samples over the space and y_i denotes the amplitude of i^{th} sample point which is taken as a point light source.

The performance of the model is determined according to the algorithmic complexity of the implemented method and the deviation of the reconstructed field from the initial one. In this chapter, the deviation is assessed by visual

evaluation. The algorithmic complexity is determined by the number of complex multiplications as in the previous chapters. To implement the source model in 2D space, we need $s(\frac{N}{2}\log_2 N + N)$ complex multiplications. The number of complex multiplications increases to $s(N^2 \log_2 N + N^2)$ in 3D space scenarios. The first term in the parenthesis is due to the inverse fast Fourier transform (FFT) to compute $\mathbf{r}(p_i, n_i)$ for each point source. The second term is needed for the scaling of each column vector by the source amplitude. The expression within parenthesis has to be performed s times to obtain the superposition over all given sample points. The similar approach, presented in [63], is used to compute the diffraction fields from 2D objects over 3D space. However, the implemented method in [63] utilizes Fresnel approximation to describe the diffraction field relationship due to a point light source.

For evaluation and illustration purposes, a simple synthetic signal over the reference line is defined. Then, the field over the entire space is computed from this synthetic signal. In the implemented scenarios, the defined synthetic signal is a discrete unit-amplitude square pulse of 32 samples located at the center of a reference line as in Chapter 4. Also, each transversal line in the space has $N = 256$ samples and there are $M = N$ transversal lines over the 2D space. Sampling periods in both x and z axes are the same, and taken as $X = \lambda$.

The presented simulations are only comprising 2D space scenarios, thus there is no variation along one of the transversal directions when 3D space scenarios are considered. But, to have better visual evaluation, we form 2D optical patterns by repeating the 1D field over the reference line. An example can be seen from Figure 5.2(a). The magnitude of the diffraction field over the entire space due to the synthetic signal defined on the reference line is shown in Figure 5.2(b).

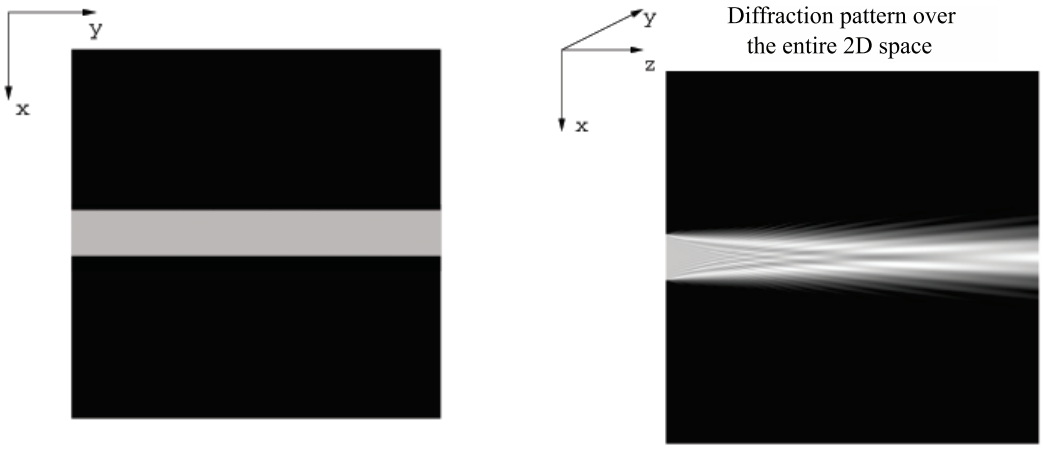

(a) (b)

Figure 5.2: (a) Magnitude of the synthetically generated diffraction field on the reference line. This is a 2D signal with 1D variation on it. For visualization purposes, the signal along the vertical direction is repeated N times horizontally to form N by N image (Images given in this paper has 256 grey levels)(b) Magnitude of the diffraction field over entire 2D space. (©2008 IEEE. Reprinted with permission. Published in [2])

In the first set of implemented scenarios, the effect of the thickness of the region along the longitudinal axis, z, is investigated as in Chapter 4. The degree of freedom of the problem is determined by the number of plane waves forming the diffraction field over the entire space. Perfect reconstruction can be achieved by the source model, which is summarized in Eq. 5.2, when all the samples are taken over a transversal plane. In that case, there is no coupling between the fields emitted by the sample points, because the kernel, $\mathbf{r}^H(p_i, n_i)$, given in Eq. 5.2 is in the sampled form of the RS diffraction kernel presented in Eq. 2.12. There will be no effect of the kernel along the direction which is perpendicular to the propagation direction because of the cosine factor on the kernel. If all the samples are given along the transversal direction then the perfect reconstruction is possible when the source model is employed. Since, the diffraction field over the entire space is formed by 256 propagating waves in the implemented scenarios,

we need at least 256 sample points in the space, for the inverse problem, not to deal with an under-determined problem. Therefore, the region in which the samples are given, is narrow along the longitudinal axis and has full extent along the transversal axis. We choose to take $1.2 \times 256 = 307$ samples to overcome a possible bottleneck that can arise due to insufficient amount of information as described in Chapter 4. The locations of the sample points are shown in Figure 4.17. Furthermore, to see the effect of the distance between the region in which the samples are taken and the reference line, an additional scenario, which can be seen in Figure 5.3(b), is implemented.

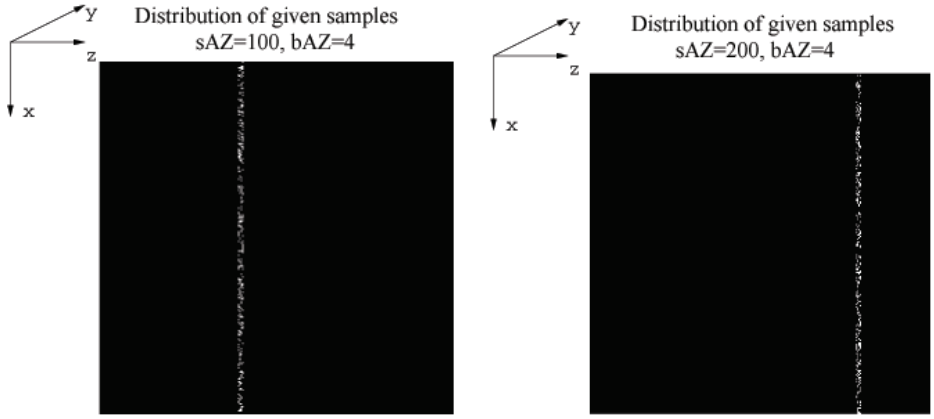

(a) (b)

Figure 5.3: Locations of the given data points. The number of given samples, s, is taken as 307. The thickness of the volume which contains all data points is 4λ as in Figure 4.17(a), but the distances between this volume and the reference line are changed. (a) the distance is taken as 100λ (b) the distance is taken as 200λ. (Published in [2])

The magnitudes of the reconstructed fields from the given samples using the source model are illustrated in Figure 5.4. To have better visual evaluation, N by N square images are formed by repeating N times the 1D reconstructed patterns over the reference line. Also, a 1D plot of the reconstructed pattern, a transversal slice of the Figure 5.4(a), is shown in Figure 5.4(b) to give an insight to the reader about the shape of the reconstructed signal on the reference line by

the source model. As it can be seen from Figure 5.4(a) and Figure 5.4(f), there is a strip at the middle of the frame. However, when the depth of the region is increased gradually, the quality of the strip degrades shown in Figures 5.4(c), 5.4(d) and 5.4(e).

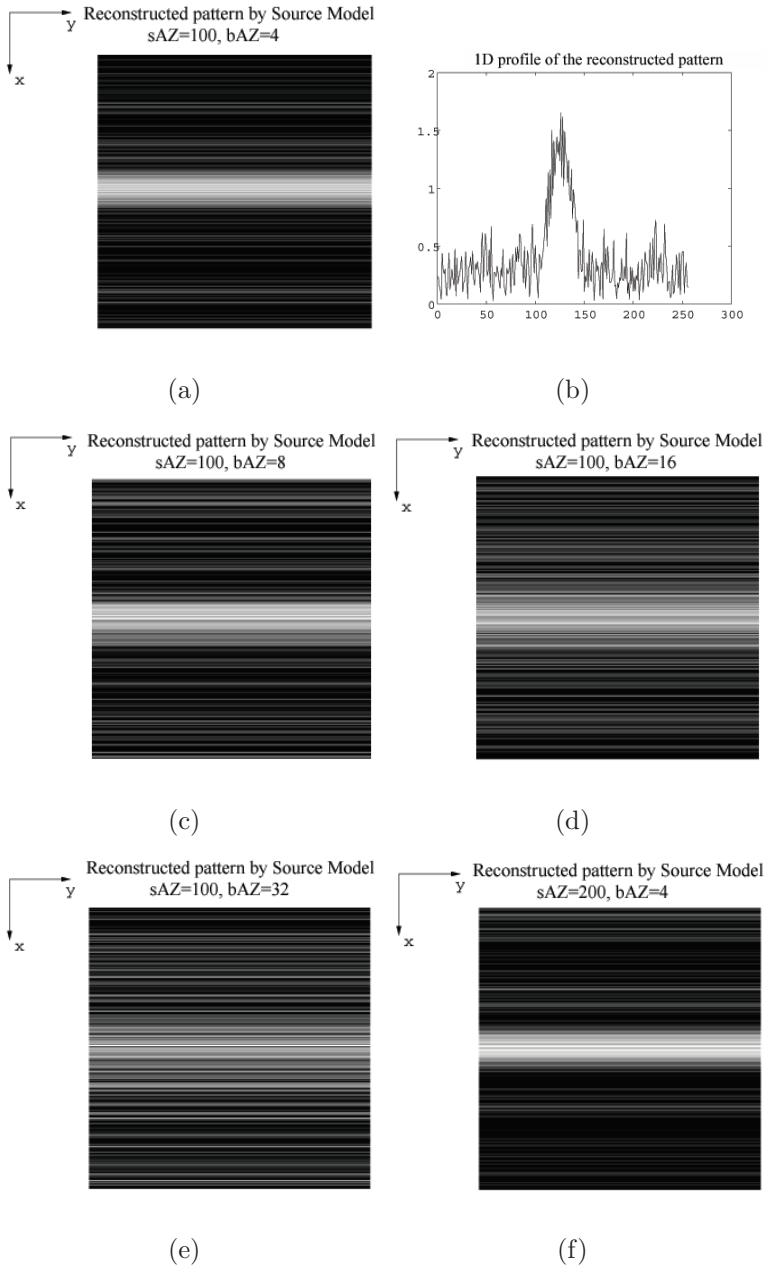

Figure 5.4: (a) Magnitude of the reconstructed diffraction field on the reference line by the source model when the given data points are distributed as in Figure 4.17(a). (b) 1D profile of the same pattern in Figure 5.4(a). (c) Magnitude of the reconstructed field by the same method under the conditions given in Figure 4.17(b). (d) Obtained result when the given sample points are distributed as in Figure 4.17(c). (e) Reconstructed pattern when the samples are distributed as in Figure 4.17(d). (f) Magnitude of the reconstructed field on the reference line when the given samples as in Figure 5.3(b).(©2008 IEEE. Reprinted with permission. Published in [2])

In the next scenario, samples are taken within a region whose shape is an isosceles triangle as in the simulations presented in Chapter 4. The number of samples is again taken as 307 which is larger than the degrees of freedom of the problem. Locations of the samples over the space for this set of scenarios are shown in Figure 4.20. The reconstructed patterns on the reference line are computed by using Eq. 5.2. Then, in order to conduct a visual evaluation, the reconstructed pattern is repeated N times along the y-axis to get a 2D image. As a result of this, the presented reconstruction problem is extended to diffraction field computation from a 2D object over 3D space where there is no variation along the y-axis.

The reconstructed patterns related to the implemented scenarios shown in Figure 4.20 are illustrated in Figure 5.5.

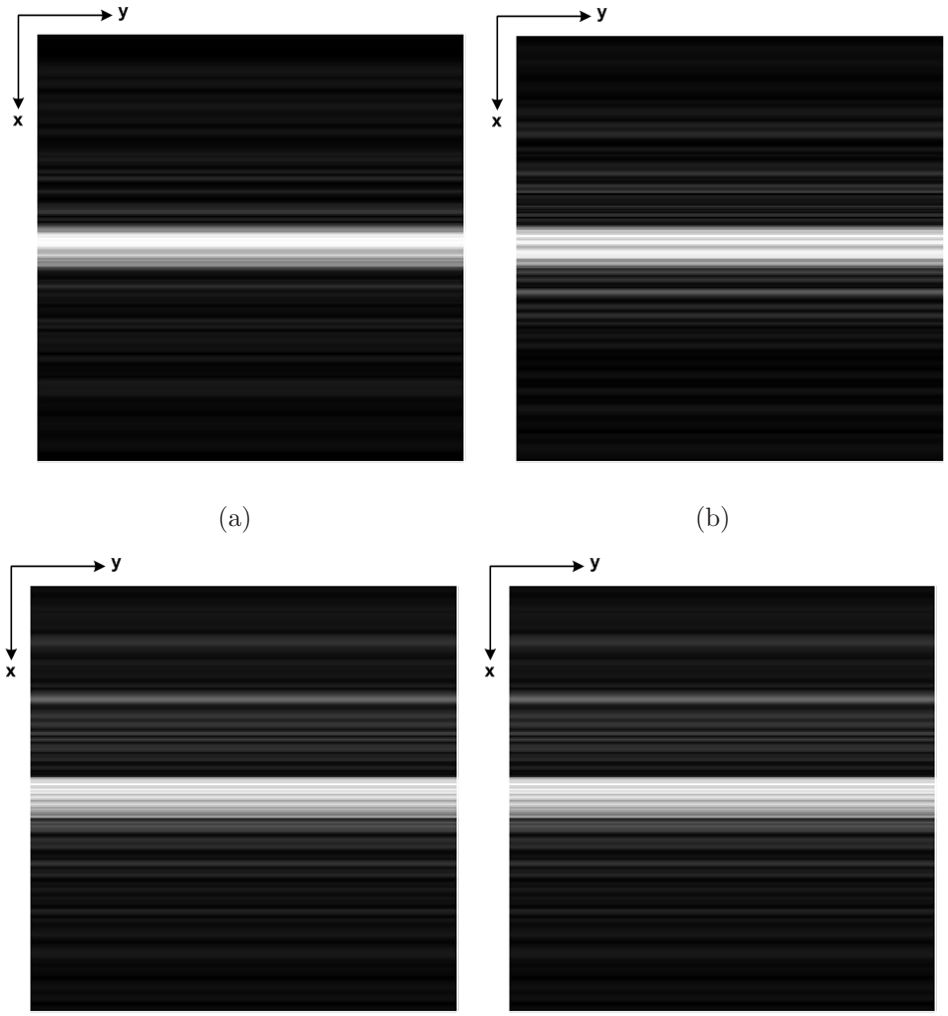

Figure 5.5: Reconstructed fields on the reference line under the scenarios illustrated in Figure 4.20. (a) Reconstructed field for the scenario shown in the Figure 4.20(a). (b) for the scenario illustrated in the Figure 4.20(b). (c) for the scenario illustrated in the Figure 4.20(c). (d) for the scenario illustrated in the Figure 4.20(d).

As it can be seen from the reconstructed patterns shown in Figure 5.5, the angle of the isosceles triangle has no significant effect on the quality of the reconstructed diffraction patterns; all reconstructions are unacceptably inferior.

In another scenario, the samples are taken along a diagonal line and the number of the given samples is decreased to 256. Illustration of the implemented

scenario is shown in Figure 5.6. The distance between the consecutive sample points is set to $\sqrt{2}\lambda$.

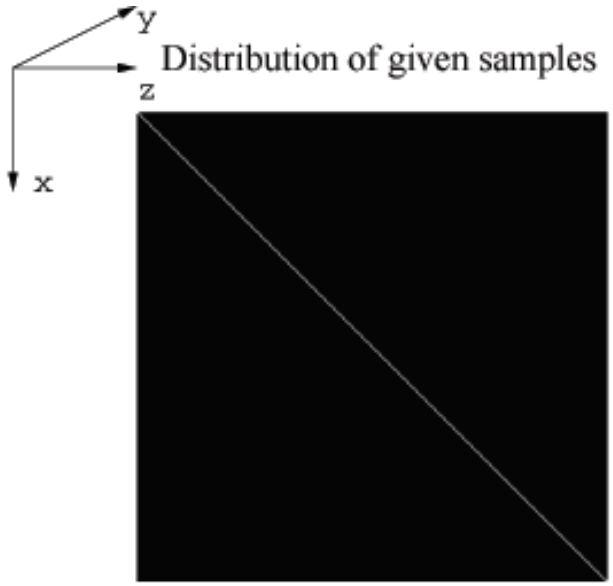

Figure 5.6: The samples of the diffraction field are taken along a diagonal line over the space. The reference line is chosen as $z = 0$. (©2008 IEEE. Reprinted with permission. Published in [2])

The strip at the middle can be easily recognized in Figure 5.7. There is only a small amplitude variation on it. The reconstructed pattern is much better than the previous ones even if the number of given samples is decreased to 256.

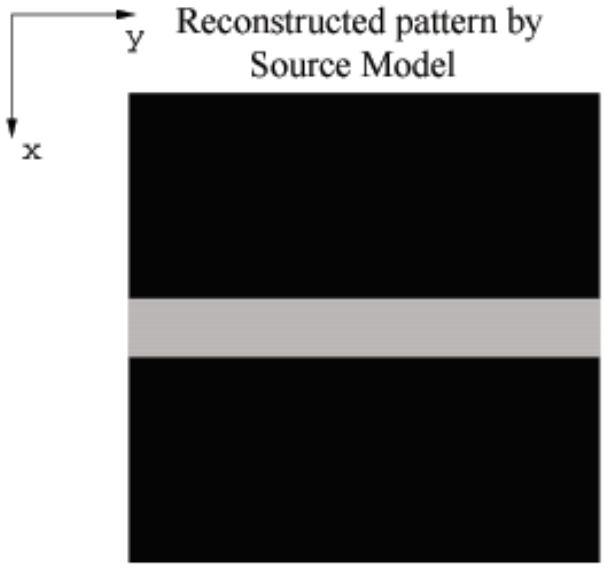

Figure 5.7: Magnitude of the reconstructed diffraction field on the reference line by the source model. The given data points are distributed as in Figure 5.6. The reconstructed field on the vertical reference line is repeated N times along horizontally to have conventional visual evaluation over N by N image.(©2008 IEEE. Reprinted with permission. Published in [2])

Fourth set of scenarios shows that we can obtain better results by the source model compared to the previous examples when the cumulative field, which is caused by the rest of the point sources, at a sample point tends to be independent of the location. The samples are taken within a smooth region whose shape is a circle. The radius of the circle is changed from 10λ to 40λ and the number of samples in these scenarios is also changed from 317 to 5025 as in the Chapter 4. The number of given samples is larger than the degree of freedom of the problem even for the first implemented scenario in the fourth set of scenarios. The distribution of the samples are shown in Figure 4.25. The source model works fine under these scenarios. Magnitude of the reconstructed fields can be seen in Figure 5.8.

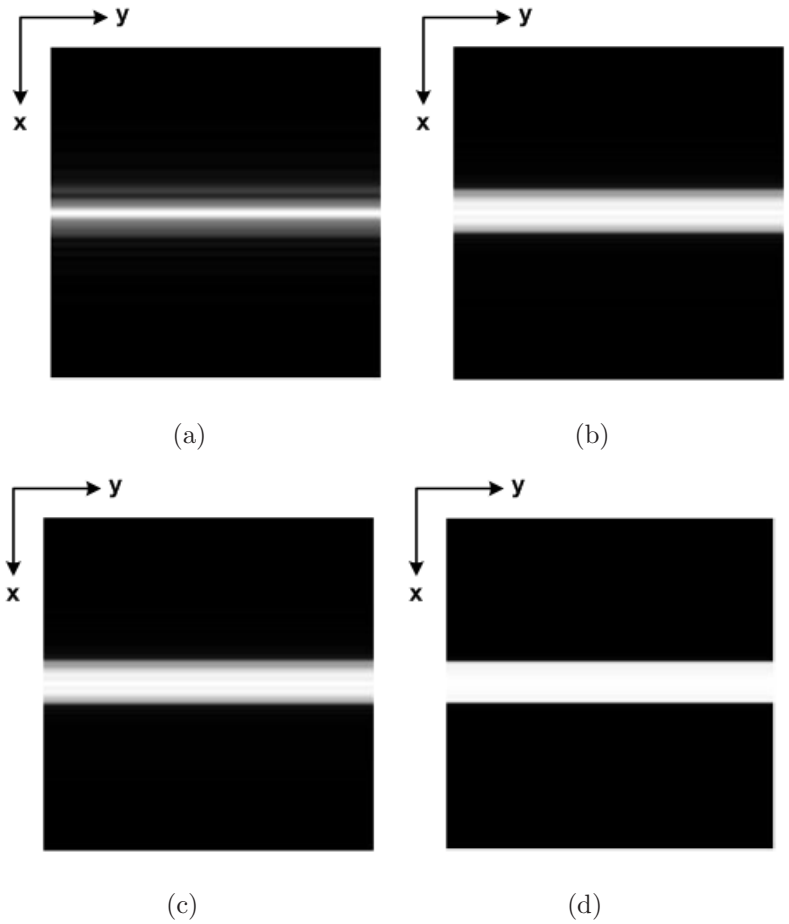

Figure 5.8: Magnitude of the reconstructed field when the samples are distributed over the space as in Figure 4.25. The reconstructed field on the vertical reference line is repeated N times along horizontally to have conventional visual evaluation over N by N image. (a) Reconstructed field for the scenario shown in the Figure 4.25(a). (b) for the scenario illustrated in the Figure 4.25(b). (c) for the scenario illustrated in the Figure 4.25(c). (d) for the scenario illustrated in the Figure 4.25(d).

In the last set of scenarios, we investigate performance of the source model from the visual evaluations of the reconstructed patterns even the number of given samples is less than the degree of freedom of the problem. The samples are again taken from a smooth surface over the space. We use a ring shaped region as an object which has a smooth surface. Then, we changed the radius of the ring. As a result of this, the number of given samples is changed, but still it is less

than the degree of freedom of the problem. When the radius is chosen as 10λ, the number of given samples is 65. Then, the radius is increased to 20λ, then we have 129 samples. In the next scenario, the radius is set to 30λ and we have 193 samples over the space. In the last scenario, the radius is taken as 40λ. Even for this scenario the number of given samples is 249. Implemented scenarios are illustrated in Figure 5.9. The reconstructed patterns for the scenarios shown in Figure 5.9 can be seen in Figure 5.10.

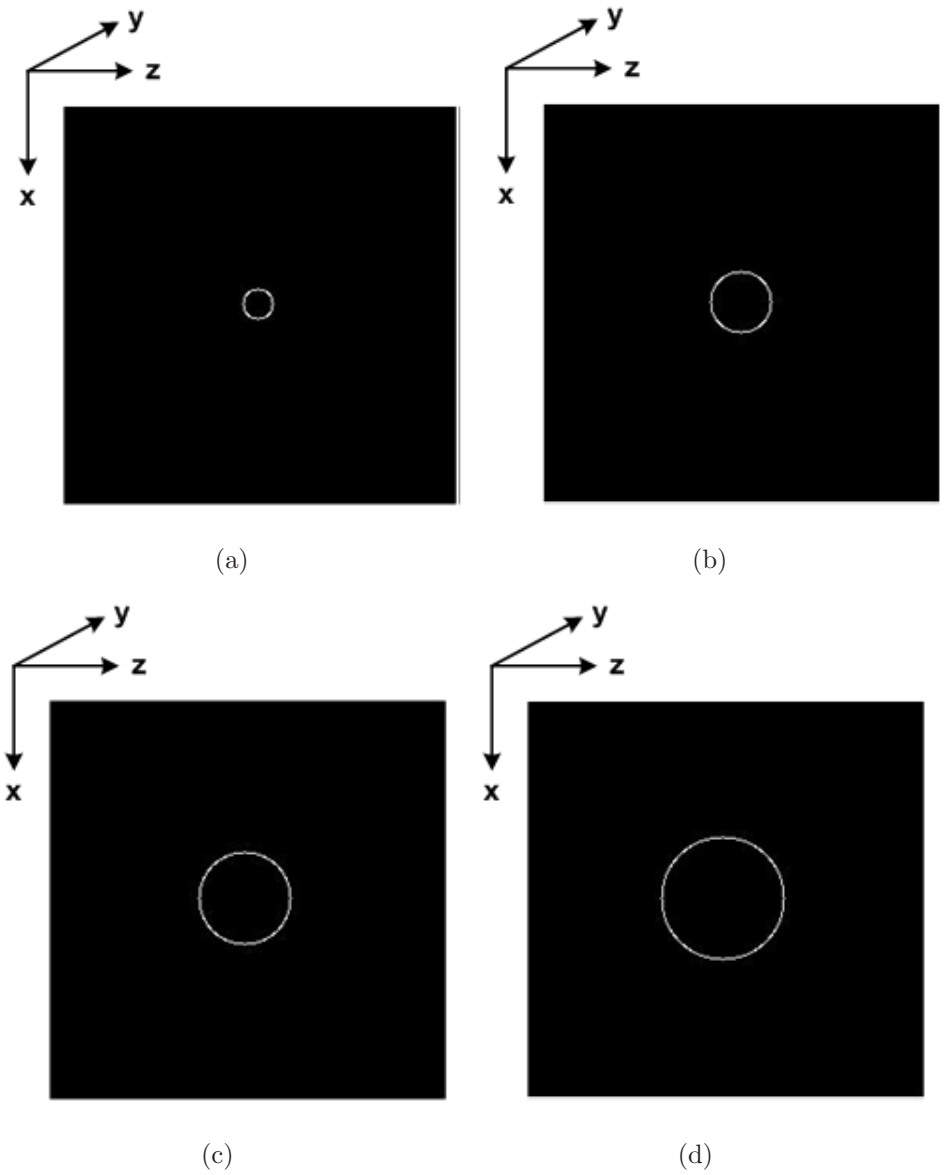

Figure 5.9: Locations of the given data points over the 2D space. $z = 0$ line is taken as the reference line. Samples are taken from a ring shaped region and the distance between the center of the ring and the reference line is 128λ. The radius of the ring is changed. (a) radius = 10λ. (b) radius = 20λ. (c) radius = 30λ. (d) radius = 40λ.

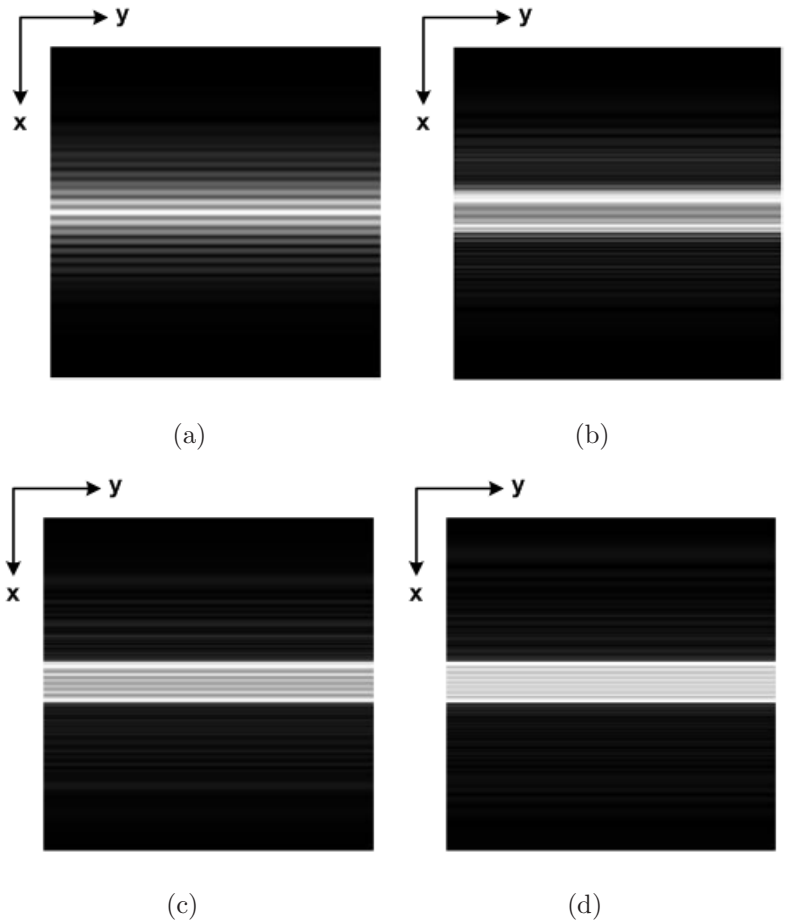

Figure 5.10: Magnitude of the reconstructed field when the samples are distributed over the space as in Figure 5.9. (a) Reconstructed field for the scenario shown in the Figure 5.9(a). (b) for the scenario illustrated in the Figure 5.9(b). (c) for the scenario illustrated in the Figure 5.9(c). (d) for the scenario illustrated in the Figure 5.9(d).

Quality of the reconstructed patterns increases when the number of samples is increased as expected, but it is seen from the fifth set of scenarios that reasonable quality reconstructions can also be obtained even when the number of given samples is less than the degree of freedom of the problem.

In this chapter, we investigated the performance of the source model algorithm based on visual evaluation of the reconstructed patterns from the given samples over the space. The implemented source model is based on superposition

of the diffraction fields emanated from the hypothetical light sources located at the given sample points. In the implemented scenarios, the distribution of the given sample points over the space and their total number are changed. As shown in the beginning of this chapter, the diffraction field, calculated by source model based algorithms, can be different from the exact field over the space. The difference between the calculated and the exact field is based on discarding the mutual coupling between the diffraction fields created by the elementary building blocks. The distribution of the samples over the entire space affects the deviation of the calculated field from the exact field. The deviation will be zero only when there will be no cumulative field on each sample due to the other samples. Also, the deviation can be kept low when cumulative field at the location of each point due to all other sources becomes negligible. Furthermore, there are some cases that the deviation can be low even if the cumulative field at the location of each point due to all other sources is not negligible. For instance, such a result is obtained when the cumulative field at each point source caused by the rest of the point sources tends to be independent of its location.

Chapter 6

Conclusions

In this dissertation, algorithms for computation of exact scalar optical diffraction field over the entire space due to the given diffraction field defined over an orientable manifold are presented. It is assumed that the diffraction field over the entire space is formed by a finite number of propagating plane waves. Therefore, by computing the complex amplitudes of the propagating plane waves, the continuous diffraction field over the entire space can be reconstructed as Fourier series expansion. In this dissertation, the proposed algorithms compute the complex amplitudes of the propagating plane waves due to the samples of the diffraction field which is defined over an orientable manifold. Performance evaluations of the proposed algorithms are obtained by the normalized errors and the computational complexities of the algorithms. Performances of the proposed algorithms are tested for several complex valued function and under various scenarios. The scalar optical diffraction field relationship, which is employed in the proposed algorithms, is based on the propagation of plane waves in space. We choose to discard the evanescent waves from the field calculation, because we are dealing only with propagating waves. This is the only approximation applied in the field calculations employed in the proposed algorithms.

In this work, two different computation approaches to the scalar optical diffraction field due to a given diffraction field are investigated:"field model" and "source model". First model takes the problem as a signal recovery issue from the given partial information of the diffraction field over the entire space. If the necessary amount of information is provided, field model based methods compute the diffraction field over the entire space perfectly. The amount of yielded information is determined by the number of given independent samples; it is also affected by the structure of the manifold on which the given samples are defined. In the second approach, the samples of the diffraction field, which are defined on the manifold, are considered as point light sources. Then, the diffraction field over the entire space is computed by the superposition of the diffraction fields emanated from the point samples. Therefore, it is assumed that each point sample emits light independent of other point samples. If the diffraction field over the entire space is calculated due to these point samples without taking into consideration of the mutual couplings between them, then the original field values at these point samples are changed. As a result of this, the calculated field can be different from the original field over the entire space.

In this work, four field model algorithms and their analyses under several scenarios are presented. The performances of the algorithms are evaluated by their normalized error and computational complexities according to the number of given samples. Furthermore, the performance of the algorithm, which is based on pseudo inversion of the system matrix, is investigated according to the locations of the given samples. Similar investigation is also performed for the source model algorithm.

In the presented field model algorithms, the given diffraction fields defined over the manifolds can be considered as a representation of an object or just as an intersection of the propagated fields by the manifold which represents the surface of the object. Then, the field over the manifold is sampled and from

these samples diffraction field over the entire space is simultaneously calculated. Therefore, we can compute the exact diffraction field (due to propagating waves) that takes care of the couplings between the given field samples, as well.

The first field model algorithm is based on the decomposition of the diffraction field defined over the manifold onto a function set which is derived from the intersections of the propagating planes waves by the manifold. One of the commonly used decomposition in diffraction field analysis is the plane wave decomposition. A diffraction field over a planar surface can be expressed by the superposition of these propagating plane waves. Furthermore, intersections of these plane waves by a planar surface are complex exponentials which form an orthogonal function set. Then, as in the Fourier series expansion, each plane wave has a complex amplitude and these complex amplitudes of the plane waves can be computed by performing a 2D forward Fourier transform of the diffraction field defined over the planar surface. Also, the frequencies of the complex exponentials over the planar surface are determined by the propagation direction of the plane wave and the surface normal. But, when the defined manifold is a curved surface then the intersections of the propagating plane waves by the manifold may not form an orthogonal function set as in planar surfaces. Furthermore, these function sets obtained from the intersection of the plane waves by the manifold may not be put into form of the complex exponentials as in the Fourier series expansion. Therefore, the complex amplitudes of the propagating plane waves may not be found by performing a 2D Fourier transform directly as in the scenarios in which planar surfaces are used. In this work, first, the intersections of the plane waves over the manifold are orthogonalized. Then, the complex coefficients of the plane waves are computed from the inner product of these orthogonalized functions by the diffraction field over the manifold. It is shown in Chapter 3 that by employing Gram-Schmidt orthogonalization over these functions which are the intersection of the plane waves by the manifold, we can compute complex amplitudes of the propagating plane waves. By using the

presented method in Chapter 3, continuous diffraction field over the entire space due to the propagating plane waves can be reconstructed perfectly from the given discrete field over the manifold. In the proposed algorithm, the diffraction field over the manifold and the intersections of the propagating plane waves by the manifold are stored as vectors in both 2D and 3D space scenarios. Therefore, the sizes of the vectors in 3D space scenarios can be larger than the sizes of the vectors defined in the 2D space scenarios. As a result of this, in 3D space scenarios, there can be a memory allocation problem.

The second field model algorithm is based on pseudo inversion of the system matrix. In determination of the computational complexity, we assume that the cost of complex multiplications dominate other operations. Therefore, the number of complex multiplications are taken as the measure of the computational complexity. To implement the pseudo inversion of the system matrix, we need $sN^2 - N^3/3$ complex multiplications in 2D scenarios where s denotes the number of given samples and N is the number of samples along the transversal axis; N is also the number of plane waves forming the diffraction field over the entire space. We observed that computational complexity of the algorithm is relatively high compared to the iterative methods when the number of given samples is larger than $1.4N$. The algorithm based on the pseudo inversion of the system matrix can be extended to compute diffraction field for the 3D space scenarios, but to store $\mathbf{A}_{BF}$ matrix, a large amount of memory is needed. In 3D space scenarios, to implement the pseudo inversion of the system matrix, we need $sN^4 - \frac{N^6}{3}$ complex multiplications. Therefore, it is not feasible to employ the pseudo inversion algorithm for the 3D cases.

The lowest normalized error among the algorithms, which are presented in Chapter 4, can be obtained by pseudo inversion method even for the scenarios in which the necessary amount of information is not given to get perfect reconstruction. Thus, the effect of the distribution of the given samples over the space is

only investigated for the algorithm based on pseudo inversion of the system matrix. The algorithm provides perfect reconstruction when the samples of the field distributed over the space uniformly random and when their number is equal to or larger than N. The yielded information can be affected by the distribution of the given samples over the space. In these scenarios, the information harvested from the given samples may not enough to achieve perfect reconstruction. Increasing the number of samples provides more information, but the number of samples and the amount of harvested information from the given samples are not related to each other linearly due to inter dependencies among the samples. To decrease the inter dependencies among the samples, the samples over the space can be taken randomly. If the given samples are located too close to each other, the diffraction fields at the given samples become relatively similar. Therefore, the necessary amount of information to reconstruct the field over the entire space may not be captured. To observe the effect of the inter-dependencies among the samples to the solution, we use the eigenvalue distribution of the system matrix, $\mathbf{A}_{BF}$. The eigenvalue distribution provides the condition number of the system matrix. It is observed that uniformly random selection of the samples or dealing with a large number of samples within a closed region helps to achieve lower normalized error on the computed diffraction field. However, when the field samples are located too close to each other, then most of the eigenvalues become practically zero. As a result, perfect reconstruction may not be achieved.

The third algorithm based on the field model utilizes an iterative method which employs projection onto convex sets. The algorithm also provides perfect reconstruction of the initial field when the number of given samples is larger than the degree of freedom of the problem. Due to its iterative structure, computational complexity of the presented algorithm is determined by the iteration number which is implicitly related to the number of given samples. The number of complex multiplications needed to implement the algorithm in 2D scenarios is

$n_{it}\big(MN\log_2 N + MN\big)$ where M is the number of lines used in 2D space. We observed that the algorithm provides advantages over the pseudo matrix inversion method associated to the computational complexity when the number of samples is larger than $1.4N$ in 2D scenarios where N is the number of plane waves used in the implemented scenario. POCS based algorithm is also extended to compute diffraction fields for 3D cases. Compared to other field model algorithms, POCS based algorithms can be implemented with a feasible amount of memory allocation even for larger 3D objects. The number of complex multiplications that are needed to implement 3D scenarios is found as $n_{it}(MN^2 \log_2 N + MN^2)$.

The last algorithm presented in the dissertation is again an iterative method. It uses conjugate gradient search algorithm to calculate the inverse of the system matrix. As the algorithms mentioned above, perfect reconstruction of the initial field can also be obtained from the CG based algorithm when the number of given samples are larger than the number of plane waves used in calculation of the diffraction field over the entire space. As in the POCS algorithm, the number of iterations is a parameter in the computational complexity of the CG based algorithm. In 2D scenarios, we need $2n_{it}N^2 + sN + M\frac{N}{2}\log_2 N$ complex multiplications to compute the diffraction field over the entire space. We observed that, CG based algorithm provides advantages over the POCS based algorithm in terms of the computational complexity when the number of given samples is between $0.5N$ and $1.2N$. The CG based algorithm is extended to 3D space by a similar procedure employed in the pseudo inversion based algorithm. Therefore, the need for large amount of memory allocation is also a problem for the CG based algorithm. Furthermore, the number of complex multiplications needed in implementation of the algorithm in 3D scenarios becomes $2n_{it}N^4 + sN^2 + MN^2 \log_2 N$. The computational complexity of the CG based algorithm is rather high compared to POCS based algorithm for the 3D scenarios.

The algorithms which are based on the source model approach are commonly used in the literature for diffraction field calculation. There are several reasons which make this choice appealing. One of the reason is the computational complexity, because computational complexity can be decreased significantly to feasible levels when the source model is used. For instance, there are some source model based algorithms that can be employed in real-time applications for small objects. Furthermore, source model based algorithms can be easily mapped to parallel computing and architectures, such as graphical processing units or other spacial hardwares. On the other hand, the source model based algorithms can not provide the exact diffraction field unless the samples are taken over a plane, because only in that scenario there is no mutual coupling between the sources. Even if the amount deviation can be changed by the locations of the point sources, the exact field over the space can not be calculated by the source model algorithms. Better visual evaluation and smaller deviation can be achieved when the cumulative field at a source point location due to all other source points becomes negligible. Also, there are some scenarios that there is a significant amount of the cumulative field at a source point due to all other sources, but the amount of cumulative field tends to be independent of the location of the source point. Although there are some ways to decrease the deviation, such as taking samples from smooth surfaces and having as much samples as possible, source model approach may not provide to calculate exact field over the space, except when all the sources points are taken over a transversal plane.

Appendix A

Nonorthogonality of Plane Waves on S_a

Nonorthogonality of the propagating plane waves on the manifold S_a is shown by a simple scenario. In Figure A.1, a simple setup is illustrated.

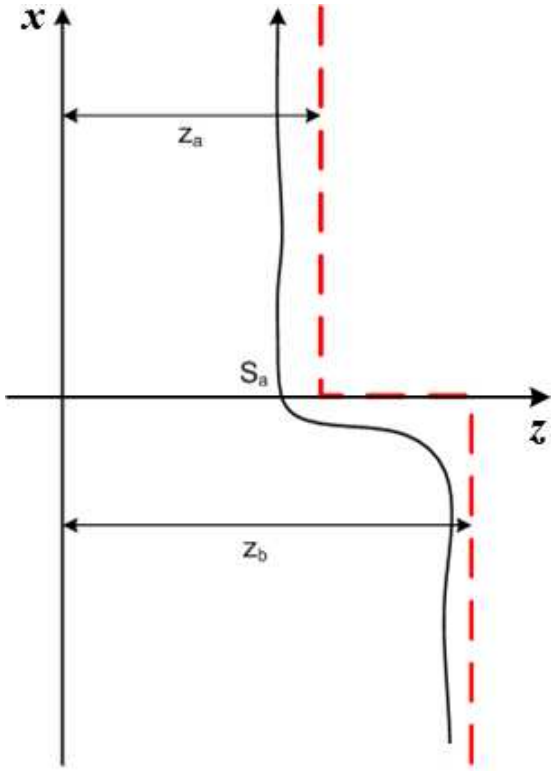

Figure A.1: 1D simple scenario to illustrate nonorthogonality of the plane waves on S_a.

The inner product of two different complex exponentials over S_a is shown as

$$\langle \exp(j{\mathbf{k}_1}^T\mathbf{x}), \exp(j{\mathbf{k}_2}^T\mathbf{x})\rangle\Big|_{S_a} = \int_{S_a} \exp\left[j(\mathbf{k}_1-\mathbf{k}_2)^T\mathbf{x}\right] dS \tag{A.1}$$

$$= \int_{S_a} \exp(j{\mathbf{k}_3}^T\mathbf{x}) dS \tag{A.2}$$

$$= \int_{-\infty}^{0} \exp(jk_{3,x}x)\exp(jk_{3,z}z_b)dx + \int_{z_b}^{z_a} \exp(jk_{3,z}z)dz + \int_{0}^{\infty} \exp(jk_{3,x}x)\exp(jk_{3,z}z_a)dx \tag{A.3}$$

$$= (-\frac{1}{jk_{3,x}} + \pi\delta(k_{3,x}))\exp(jk_{3,z}z_b) + \frac{\exp(jk_{3,z}z_a) - \exp(jk_{3,z}z_b)}{jk_{3,z}} + (\frac{1}{jk_{3,x}} + \pi\delta(k_{3,x}))\exp(jk_{3,z}z_a). \tag{A.4}$$

Since, the result of the integral given above is not equal to $C\delta(k_{3,x})$, the function set obtained from the intersection of the propagating plane waves by the manifold S_a is not orthogonal. The first and the third integrals in Eq. A.3 can be computed from the Fourier transform property of signum, $sgn(x)$, function. In [14], the Fourier transform of $sgn(x)$ is given as

$$\int_{-\infty}^{\infty} sgn(x) \exp(j2\pi f x) dx = \frac{1}{j\pi f} \tag{A.5}$$

The result obtained by Eq. A.4 shows that orthogonality can not be satisfied even for this simple scenario. To have orthogonal functions, an orthogonalization method can be used as shown in Chapter 3.

Appendix B

Proof of the properties of matrix A

Although the proof that the matrix $\mathbf{A}$ is unitary is first published in [1], because of the completeness of the dissertation, it is given as an appendix. If a matrix is unitary, it has to satisfy $\mathbf{A}^H\mathbf{A} = \mathbf{I}$ [75]. For the matrix $\mathbf{A}$, it shown as follows:

$$\begin{aligned}
\mathbf{A}^H\mathbf{A} &= \mathbf{A}\mathbf{A}^H = \mathbf{I} \\
&= (\mathbf{W}^{-1}\mathbf{H}_p\mathbf{W})(\mathbf{W}^{-1}\mathbf{H}_p\mathbf{W})^H \\
&= (\mathbf{W}^{-1}\mathbf{H}_p\mathbf{W})(\mathbf{W}^H\mathbf{H}_p^H\mathbf{W}^{-H}) \\
&= \mathbf{W}^{-1}\mathbf{H}_p N\mathbf{H}_p^H\mathbf{W}^{-H} \\
&= \mathbf{W}^{-1}N\mathbf{W}^{-H} \\
&= \mathbf{I}.
\end{aligned} \tag{B.1}$$

The matrix $\mathbf{A}$ has another property which is

$$\begin{aligned}
\mathbf{A}^l\mathbf{A}^j &= (\mathbf{W}^{-1}\mathbf{H}_{lp}\mathbf{W})(\mathbf{W}^{-1}\mathbf{H}_{jp}\mathbf{W}) \\
&= \mathbf{W}^{-1}\mathbf{H}_{lp}\mathbf{H}_{jp}\mathbf{W} \\
&= \mathbf{W}^{-1}\mathbf{H}_{(l+j)p}\mathbf{W}
\end{aligned} \tag{B.2}$$

where $\mathbf{H}_{(l+j)p}$ represents the kernel of the discrete system which is used to calculate the diffraction field at $p(l+j)$.

Appendix C

Proof of convergence by POCS

The proof of the problem, computation of diffraction field from the given samples over the space, can be set as projection onto convex sets is first published in [1].

The problem defined in this work can be approached as a signal recovery from partially given information. The diffraction field over the entire space is computed from the field defined over the reference line. Therefore, Eq. 4.8 has to be satisfied among all lines. The partial information related to the diffraction field over the reference line is given by the known sample points on consecutive lines over the space. As result of this, all the given samples are belong to the same diffraction field. Therefore, we can define a set, $\boldsymbol{C}_l$, for all possible diffraction fields having the given data points on a certain line $z = z_l$:

$$\boldsymbol{C}_l = \{\forall f(x,z) : f(x_{\mathbf{i}_l}, z_l) = \mathbf{v}_l;\ f(x,z_j) = \mathbf{A}^{j-l} f(x,z_l), \forall j, x\}, \tag{C.1}$$

where $l = 1, \ldots, M$ and M is the number of line over the space. The vector $\mathbf{v}_l$ denotes the known values on the line $z = z_l$ and $\mathbf{i}_l$ is the vector with the indices of their positions. The matrix $\mathbf{A}$, is given in Eq. 4.11, defines the diffraction field relation between two consecutive lines. The diffraction field relation between lines $z = z_l$ and $z = z - j$ is determined by the $(j-l)$th power of $\mathbf{A}$. The field

on the $z = z_j$ can be expressed with the help of an arbitrary function $q(x)$ as

$$f(x, z_j) = \mathbf{A}_{\mathbf{i}_l}^{j-l}\mathbf{v}_l + \mathbf{A}_{\bar{\mathbf{i}}_l}^{j-l}q(x_{\bar{\mathbf{i}}_l}), \tag{C.2}$$

where $\bar{\mathbf{i}}_l$ is the vector with the indices of the unknown values on the line $z = z_l$, and $\mathbf{A}_{\mathbf{i}_l}^{j-l}$ and $\mathbf{A}_{\bar{\mathbf{i}}_l}^{j-l}$ are submatrices of $\mathbf{A}^{j-l}$ obtained by taking columns with indices $\mathbf{i}_l$ and $\bar{\mathbf{i}}_l$.

To show that, the sets $\boldsymbol{C}_l$ defined by Eq. C.1 are convex, we take into consideration two functions, $f_1(x, z)$ and $f_2(x, z)$, belong to the set $\boldsymbol{C}_l$. Then, we define $F(x, z) = \alpha f_1(x, z) + (1-\alpha) f_2(x, z), 0 < \alpha < 1$ as their convex combination. For every line $z = z_j$, we have

$$\begin{aligned} F(x, z_j) &= \alpha\mathbf{A}_{\mathbf{i}_l}^{j-l}\mathbf{v}_l + \alpha\mathbf{A}_{\bar{\mathbf{i}}_l}^{j-l}q_1(x_{\bar{\mathbf{i}}_l}) + (1-\alpha)\mathbf{A}_{\mathbf{i}_l}^{j-l}\mathbf{v}_l + (1-\alpha)\mathbf{A}_{\bar{\mathbf{i}}_l}^{j-l}q_2(x_{\bar{\mathbf{i}}_l}) \\ &= \mathbf{A}_{\mathbf{i}_l}^{j-l}\mathbf{v}_l + \mathbf{A}_{\bar{\mathbf{i}}_l}^{j-l}Q(x_{\bar{\mathbf{i}}_l}), \end{aligned} \tag{C.3}$$

where $Q(x) = \alpha q_1(x) + (1-\alpha)q_2(x)$. Since $q(x)$ in Eq. C.2 can be an arbitrary function, the expression in Eq. C.3 becomes of the form of Eq. C.2. Therefore, $F(x, z)$ belongs to the set $\boldsymbol{C}_l$. As a result of this, it is shown that $\boldsymbol{C}_l$ is convex, because a convex combination of any two functions which belong to $\boldsymbol{C}_l$ also belongs to $\boldsymbol{C}_l$.

Iterative projections are performed from set to set by using Eq. 4.8. The known samples are kept as they are and the unknown samples are generated by diffracted field from the previous line. The projection from the set $\boldsymbol{C}_{l-1}$ to the set $\boldsymbol{C}_l$ can be shown as

$$\begin{aligned} f(x_{\bar{\mathbf{i}}_l}, z_l) &= g(x_{\bar{\mathbf{i}}_l}, z_l) \\ \text{and} \quad f(x_{\mathbf{i}_l}, z_l) &= \mathbf{v}_l \end{aligned} \tag{C.4}$$

where $g(x, z) \in \boldsymbol{C}_{l-1}$ and $f(x, z) \in \boldsymbol{C}_l$. The functions $f(x, z_l)$ and $g(x, z_l)$ have different values only at positions $x_{\mathbf{i}_l}$. Therefore the distance from $g(x, z_l)$ to $f(x, z_l)$ is minimized with respect to all functions in $\boldsymbol{C}_l$. Furthermore, the

distance along any other line $z = z_j$ is minimized because

$$\begin{aligned} d &= \|f(x, z_j) - g(x, z_j)\|^2 \\ &= \|\mathbf{A}^{j-l}(f(x, z_l) - g(x, z_l))\|^2 \\ &= \|f(x, z_l) - g(x, z_l)\|^2 \end{aligned} \tag{C.5}$$

and $\mathbf{A}^{j-l}$ is unitary for any j and l that is proved in Appendix A. As a result of this, the square of the distance between $g(x, z)$ and $f(x, z)$ is minimum for all the functions from the set $\boldsymbol{C}_l$ since

$$\|f(x, z) - g(x, z)\|^2 = \sum_j \|f(x, z_j) - g(x, z_j)\|^2.$$

Therefore, orthogonal projection of $g(x, z)$ onto the set $\boldsymbol{C}_l$ is obtained by choosing $f(x, z)$ as in Eq. C.4. Hence, the presented iterative method will converge [86].

Bibliography

[1] G.B. Esmer, V. Uzunov, L. Onural, H.M. Ozaktas, and A. Gotchev, "Diffraction field computation from arbitrarily distributed data points in space," *Signal Processing-Image Communication*, vol. 22, pp. 178–187, 2007.

[2] G.B. Esmer, L. Onural, H.M. Ozaktas, V. Uzunov, and A. Gotchev, "Performance assessment of a diffraction field computation method based on source model," in *3DTV-ConII 2008*, Istanbul, Turkey, 2008.

[3] R.J. Collier, C.B. Burckhardt, and L.H. Lin, *Optical Holography*, Academic Press, Inc., New York, 1971.

[4] T. Okoshi, *Three-Dimensional Imaging Techniques*, New York Academic Press, New York, US, 1976.

[5] Y.I. Ostrovsky, *Holography and Its applications*, Academic Press Inc., 1977.

[6] G. Saxsby, *Practical Holography*, Printice Hall, 1988.

[7] L. Yaroslavsky and M. Eden, *Fundamentals of Digital Optics*, Birkhauser, Boston, United States of America, 1996.

[8] M. Halle, "Autostereoscopic displays and computer graphics," *Computer Graphics, ACM SIGGRAPH*, vol. 31, no. 2, pp. 58–62, May 1997.

[9] I. Sexton and P. Surman, "Stereoscopic and autostereoscopic display systems: An in-depth review of past, present, and future technologies," *IEEE Signal Processing Magazine*, vol. 16, pp. 85–99, 1999.

[10] S.A. Benton and Jr. V.M. Bove, *Holographic Imaging*, John Wiley & Sons, Inc., New Jersey, United States of America, 2008.

[11] M. Lucente, *Diffraction-specific fringe computation for electro-holography*, Ph.D. thesis, Massachusetts Institute of Technology, Cambridge, MA USA, 1994.

[12] L. Yaroslavsky, *Digital Holography and Digital Image Processing: Principles, Methods, Algorithms*, Kluwer Academic Publishers, Massachusetts, USA, 2004.

[13] D. Gabor, "Holography, 1948-1971," *Proc. IEEE*, vol. 60, pp. 655–668, 1972.

[14] S. Haykin, *Communication systems*, John Wiley & Sons, Inc, 3rd edition, 1994.

[15] J.W. Goodman, *Introduction to Fourier Optics*, Mc-Graw-Hill, New York, 1996.

[16] M. Born and E. Wolf, *Principles of Optics: Electromagnetic theory of propagation, interference and diffraction of light*, Cambridge University Press, New York, 1980.

[17] H. Kang, T. Yamaguchi, H. Yoshikawa, S.-C. Kim, and E.-S. Kim, "Acceleration method of computing a compensated phase-added stereogram on a graphic processing unit," *Applied Optics*, vol. 47, no. 31, 2008.

[18] C. Petz and M. Magnor, "Fast hologram synthesis for 3d geometry models using graphics hardware," *Proc. SPIE, Practical Holography XVII and Holographic Materials IX*, vol. 5005, pp. 266–275, 2003.

[19] J.-C. Grossetie and P. Noirard, "Computer-assisted method and device for restoring three-dimensional images," U.S. Patent 6621605, 2003.

[20] Z. Liu, M. Centurion, G. Panotopoulos, J. Hong, and D. Psaltis, "Holographic recording of fast events on a ccd camera," *Optics Letters*, vol. 27, no. 1, pp. 22–24, 2002.

[21] M. Kovachev, R. Ilieva, P. Benzie, G.B. Esmer, L. Onural, J. Watson, and T. Reyhan, *Three-Dimensional Telvision: Capture, Transmission, Display*, chapter 15: Holographic 3DTV Displays Using Spatial Light Modulators, pp. 529–556, Springer-Verlag Berlin Heidelberg, 2008.

[22] V. Katkovnik, J. Astola, and K. Egiazarian, "Discrete diffraction transform for propagation, reconstruction, and design of wavefield distributions," *Applied Optics*, vol. 47, no. 19, pp. 3481–3493, 2008.

[23] R. Tudela, I Labastida, E. Martín-Badosa, S. Vallmitjana, I. Juvells, and A. Carnicer, "A simple method for displaying fresnel holograms on liquid crytal panels," *Optics Communications*, vol. 214, pp. 107–114, 2002.

[24] R. Tudela, E. Martín-Badosa, I Labastida, S. Vallmitjana, and A. Carnicer, "Full complex fresnel holograms displayed in liquid crystal devices," *Journal of Optics A: Pure and Applied Optics*, vol. 5, no. 5, 2003.

[25] T. Kreis, P. Aswendt, and R. Hofling, "Hologram reconstruction using a digital micromirror device," *Optical Engineering*, vol. 40, pp. 926–933, 2001.

[26] B.E.A. Saleh and M.C. Teich, *Fundamentals of Photonics*, John Wiley and Sons, Inc., 1991.

[27] D. Leseberg and C. Frére, "Computer generated holograms of 3D objects composed of tilted planar segments," *Appl. Opt.*, vol. 27, pp. 3020–3024, 1988.

[28] G.E. Moss, "Segmented 3-D hologram display," U.S. Patent, number 4795223, 1989.

[29] H.-S. Buchkremer and U. Rockenfeller, "Large display composite holograms and methods," U.S. Patent, number 5734485, 1998.

[30] R. Ziegler, P. Kaufmann, and M. Gross, "A framework for holographic scene representation and image synthesis," *IEEE Trans. on Visulization and Computer Graphics*, vol. 13, pp. 403–415, 2007.

[31] M. Janda, I. Hanák, and L. Onural, "Hologram synthesis for photorealistic reconstruction," *J. Opt. Soc. Am. A*, vol. 25, no. 12, pp. 3083–3096, 2008.

[32] S. Cunningham, *Computer Graphics: programming in OpenGL for Visual Communication*, Prentice Hall, 2006.

[33] K. Matsushima, H. Schimmel, and F. Wyrowski, "Fast calculation method for optical diffraction on tilted planes by use of the angular spectrum of plane waves," *J. Opt. Soc. A*, vol. 20, pp. 1755–1762, 2003.

[34] G.B. Esmer, "Computation of holographic patterns between tilted planes," M.S. thesis, Bilkent University, Dept. of Electrical and Electronics Engineering, Ankara, Turkey, 2004.

[35] G. Saxby, *Practical Holography*, The University Press, Cambridge, 1994.

[36] A. Asundi and V.R. Singh, "Sectioning of amplitude images in digital holography," *Meas. Sci. Technol.*, vol. 17, pp. 75–78, 2006.

[37] G. Groh, "Multiple imaging by means of point holograms," *Applied Optics*, vol. 7, no. 8, pp. 1643–1644, 1968.

[38] H. Dammann and K. Grtler, "High-efficiency in-line multiple imaging by means of multiple phase holograms," *Optics Communications*, vol. 3, no. 5, pp. 312–315, 1971.

[39] F. Chen, G.M. Brown, and M. Song, "Overview of three-dimensional shape measurement using optical methods," *Optical Engineering*, vol. 39, no. 1, pp. 10–22, 2000.

[40] B.R. Brown and A.W. Lohmann, "Computer-generated binary holograms," *IBM Journal of Research and Development: Optical Science and Technology*, vol. 13, no. 2, pp. 160–168, 1969.

[41] G. Tricoles, "Computer generated holograms: an historical reivew," *Applied Optics*, vol. 26, no. 20, pp. 4351–4360, 1987.

[42] M. Kitamura, "Computer-generated hologram," U.S. Patent, number 7068403 B2, 2006.

[43] K. Matsushima, "Computer generated holograms for three-dimensinal surface objects with shade and texture," *Applied Optics*, vol. 44, no. 22, pp. 4607–4614, 2005.

[44] G.W. Burr, J. Ashley, H. Coufal, R.K. Grygier, J.A. Hoffnagle, C.M. Jefferson, and B. Marcus, "Modulation coding for pixel-matched holographic storage," *Optics Letters*, vol. 22, no. 9, pp. 639–641, 1997.

[45] R.M. Shelby, J.A. Hoffnagle, G.W. Burr, C.M. Jefferson, M.-P. Bernal, H. Coufal, R.K. Grygier, H. Günther, R.M. Macfarlane, and G.T. Sincerbox, "Pixel-matched holographic data storage with megabit pages," *Optics Letters*, vol. 22, no. 19, pp. 1509–1511, 1997.

[46] D. Psaltis and G.W. Burr, "Holographic data storage," *Computer*, vol. 31, no. 2, pp. 52–60, 1998.

[47] D. Gabor, "Character recognition by holography," *Nature*, vol. 208, pp. 422–423, 1965.

[48] H.J. Caulfield and W.T. Maloney, "Improved discrimination in optical character recognition," *Applied Optics*, vol. 8, no. 11, pp. 2354–2356, 1969.

[49] L. Onural, A. Gotchev, H.M. Ozaktas, and E. Stoykova, "A survey of signal processing problems and tools in holographic three-dimensional television,"

IEEE Trans. on Circuits and Systems for Video Tech., vol. 17, no. 11, pp. 1631–1646, 2007.

[50] J.E. Kasper and S.A. Feller, *The Complete Book of Holograms*, John Wiley & Sons Inc., 1987.

[51] R.S. Pappu, "Minimum information holograms," M.S. thesis, Media Arts and Sciences School of Architecture and Planning MIT.

[52] G.C. Sherman, "Application of the convolution theorem to rayleigh's integral formulas," *J. Opt. Soc. Am.*, vol. 57, pp. 546–547, 1967.

[53] É. Lalor, "Conditions for the validity of the angular spectrum of plane waves," *J. Opt. Soc. Am.*, vol. 58, pp. 1235–1237, 1968.

[54] L. Mandel and E. Wolf, *Optical Coherence and Quantum Optics*, Cambridge University Press, 1995.

[55] G.B. Esmer and L. Onural, "Simulation of scalar optical diffraction between arbitrarily oriented planes," in *Proceedings of 2004 First International Symposium on Control, communications and signal Processing, ISCCSP 2004*, Hammamet, Tunisia, 21-24 March 2004.

[56] G.B. Esmer and L. Onural, "Computation of holographic patterns between tilted planes," in *Holography 2005*, Varna, Bulgaria, 21-25, May 2005, vol. Proc. SPIE 6252.

[57] H.J. Rabal, N. Bolognini, and E.E. Sicre, "Diffraction by a tilted aperture, coherent and partially coherent cases," *Opt. Acta*, vol. 27, pp. 1309–1311, 1985.

[58] C. Frére and D. Leseberg, "Large objects reconstructed from computer generated holograms," *Appl. Opt.*, vol. 28, pp. 2422–2425, 1989.

[59] T. Tommasi and B. Bianco, "Frequency analysis of light diffraction between rotated planes," *Opt. Lett.*, vol. 17, pp. 556–558, 1992.

[60] T. Tommasi and B. Bianco, "Computer-generated holograms of tilted planes by a spatial frequency approach," *J. Opt. Soc. Am. A*, vol. 10, pp. 299–305, 1993.

[61] B. Bianco and T. Tommasi, "Space-invariant interconnection through the use of computer-generated holograms," *Appl. Opt.*, vol. 34, pp. 7573–7580, 1995.

[62] N. Delen and B. Hooker, "Free-space beam propagation between arbitrarily oriented planes based on full diffraction theory: a fast fourier transform approach," *J. Opt. Soc. Am. A*, vol. 15, pp. 857–867, 1998.

[63] G.B. Esmer and L. Onural, "Hologram simülatörü," in *11. Sinyal Işleme ve Uygulamaları Kurultayı Kitapçğı*, Koç Universitesi, Istanbul, Türkiye, Haziran 2003, pp. 487–490, (In Turkish).

[64] V. Uzunov, A. Gotchev, G.B. Esmer, L. Onural, and H. Ozaktas, "Non-uniform sampling and reconstruction of diffraction field," in *TICSP Series 34*, Florence, Italy, 2006.

[65] G.B. Esmer, L. Onural, H. Ozaktas, and A. Gotchev, "An algorithm for calculation of scalar optical diffraction due to distributed data over 3d space," in *ICOB 2005, Workshop On Immersive Communication And Broadcast Systems*, Berlin, Germany, 2005.

[66] E. Ulusoy, G.B. Esmer, H.M. Ozaktas, L. Onural, A. Gotchev, and V. Uzunov, "Signal processing problems and algorithms in display side of 3dtv," in *ICIP 2006*, Atlanta, GA, USA, 2006.

[67] G.B. Esmer, L. Onural, V. Uzunov, A. Gotchev, and H.M. Ozaktas, "Reconstruction of scalar diffraction field from distributed data points over 3D space," in *3DTV-Con 2007*, Kos Island, Greece, 2007.

[68] V. Uzunov, G.B. Esmer, A. Gotchev, L. Onural, and H.M. Ozaktas, "Bessel functions - based reconstruction of non-uniformly sampled diffraction fields," in *3DTV-Con 2007*, Kos Island, Greece, 2007.

[69] M. Kovachev, R. Ilieva, L. Onural, G.B. Esmer, T. Reyhan, P. Benzie, J. Watson, and E. Mitev, "Reconstruction of computer generated holograms by spatial light modulators," in *LECTURE NOTES IN COMPUTER SCIENCE*, 2006, vol. 4105, pp. 706–713.

[70] M. Lucente, "Interactive computation of holograms using a look-up table," *Lurnal of Electronic Imaging*, vol. 2, no. 1, pp. 28–34, January 1993.

[71] M. Lucente, "Interactive three-dimensional holographic displays: seeing the future in depth," *ACM SIGGRAPH Computer Graphics*, vol. 31, no. 2, pp. 63–67, May 1997.

[72] J.L. Juárez, A. Olivares-Pérez, and L.R. Berriel-Valdos, "Nonredundant calculations for creating digital fresnel holograms," *Appl. Optics*, vol. 36, no. 29, pp. 7437–7443, 1997.

[73] A. Ritter, J. Böttger, O. Deussen, M. König, and T. Strothotte, "Hardward-based rending synthetic holograms," *Appl. Optics*, vol. 38, no. 8, pp. 1364–1369, 1999.

[74] M. Matsushima and M. Takai, "Recurrence formulas for the fast creation of synthetic three-dimensional holograms," *Appl. Optics*, vol. 39, no. 35, pp. 6587–6594, 2000.

[75] M.T. Heath, *Scientfic Computing: An Introductory Survey*, McGraw-Hill, 2nd edition, 2002.

[76] S.S. Chen, D.L. Donoho, and M.A. Saunders, "Atomic decomposition by basis pursuit," *SIAM Review*, vol. 43, no. 1, pp. 129–159, 2001.

[77] R.S. Nesbitt, S.L. Smith, R.A. Molnar, and S.A. Benton, "Holographic recording using a digital micromirror device," in *Conf on Practical Holography XIII, Proc SPIE*, S. A. Benton, Ed., 1999, vol. 3637, pp. 12–20.

[78] L. Onural and P. D. Scott, "Digital decoding of in-line holograms," *Optical Engineering*, vol. 26, pp. 1124–1132, 1987.

[79] D. Mas, J. Pérez, C. Hernández, C. Vázquez, J. J. Miret, and C. Illueca, "Fast numerical calculation of fresnel patterns in convergent systems," *Optics Communications*, vol. 227, pp. 245–258, 2003.

[80] J.A.C. Veerman, J.J. Rusch, and H.P. Urbach, "Calculation of the rayleigh-sommerfeld diffraction integral by exact integration of the fast oscillating factor," *J. Opt. Soc. Am. A*, vol. 22, pp. 636–646, 2005.

[81] T.K. Moon and W.C. Stirling, *Mathematical methods and algorithms for signal processing*, Prentice-Hall, Saddle River, New Jersey, 2000.

[82] R. Aharoni and Y. Censor, "Block iterative projection methods for parallel computation of solutions to convex feasibility problems," *Linear Algebra Applicat*, vol. 120, pp. 165–175, 1989.

[83] L.G. Gubin, B.T. Polyak, and E.V. Raik, "The method of projections for finding the common point of convex sets," *USSR Comput Math Math Phys*, vol. 7, pp. 1–24, 1967.

[84] R.G. Dorsch, A.W. Lohmann, and S. Sinzinger, "Fresnel ping-pong algorithm for two-plane computer-generated hologram display," *Applied Optics*, vol. 33, pp. 869–875, 1994.

[85] R.W. Gerchberg and W.O. Saxton, "A practical algorithm for the determination of phase from image and diffraction plane pictures," *Optik*, vol. 35, pp. 237–246, 1972.

[86] D.C. Youla and H. Webb, "Image restoration by the method of convex projections: Part I-theory," *IEEE Trans Med Imag*, vol. TMI-1, pp. 81–94, 1982.

[87] T. Kotzer, N. Cohen, and J. Shamir, "A projection-based algorithm for consistent and inconsistent constraints," *SIAM J. Optim.*, vol. 7, no. 2, pp. 527–546, 1997.

[88] A.E. Çetin, H. Özaktaş, and H.M. Ozaktas, "Resolution enchancement of low resolution wavefields with pocs algorithm," *Electronics Letters*, vol. 39, no. 25, December 2003.

[89] S.G. Nash and A. Sofer, *Linear and nonlinear programming*, McGraw-Hall, 1996.

[90] A. Björck, *Numerical Methods for Least Squares Problems*, SIAM, Amsterdam, Holland, 1990.

[91] J.L. Juárez-Pérez, A. Olivares-Pérez, and L.R. Berriel-Valdos, "Nonredundant calculations for creating digital fresnel holograms," *Appl. Optics*, vol. 36, no. 29, pp. 7437–7443, 1997.